# Magnesium isotope fractionation associated with biotic and abiotic weathering *-and-* Developing a scalable method for rare earth element extraction from non-traditional feedstocks using engineered *Escherichia coli*

Aaron W. Brewer

A dissertation

submitted in partial fulfillment of the

requirements for the degree of

Doctor of Philosophy

University of Washington

2019

Reading Committee:

Fang-Zhen Teng, Chair

Yongqin Jiao

Drew Gorman-Lewis

Program Authorized to Offer Degree:

Earth and Space Sciences

University of Washington

## ABSTRACT

# Magnesium isotope fractionation associated with biotic and abiotic weathering *-and-* Rare earth element extraction from non-traditional feedstocks using engineered *Escherichia coli*

Aaron W. Brewer

Chairman of the Supervisory Committee:
Fang-Zhen Teng, Ph.D.
Department of Earth and Space Sciences

This dissertation is divided into two sections, with the first discussing magnesium (Mg) isotope behavior during biotic and abiotic rock weathering, and the second describing the application of engineered microbes for the selective recovery of rare earth elements (REEs) from non-traditional feedstocks.

Magnesium isotopes exhibit observable mass dependent fractionation during a variety of rock weathering processes, permitting them to serve as a tracer of chemical and biological weathering. First, *Bacillus subtilis* endospore-mediated forsterite dissolution experiments demonstrating the effects of cell surface reactivity on Mg isotope fractionation are discussed. The endospore surfaces preferentially adsorbed $^{24}$Mg from the forsterite dissolution products, with calculated adsorbed Mg isotope compositions reaching $\delta^{26}$Mg = approx. -0.51‰ compared to the aqueous phase at approx. -0.37‰. These results demonstrate the effect of cell surface reactivity on Mg isotope fractionation in isolation, separate from other biological processes such as metabolism and organic acid production. Second, the Mg isotope compositions of granite and granodiorite

weathering profiles were examined to investigate Mg isotope behavior during the weathering of felsic rocks. Mg isotope fractionation in these profiles was primarily controlled by primary biotite weathering and secondary illite formation and weathering. Finally, North Cascade Volcanic Arc basalts and andesites were analyzed for Mg isotopes to assess the extent and mechanism of crustal contribution to this magmatic system. The $\delta^{26}$Mg of these samples vary from within the range of ocean island basalts (the lightest being -0.33 ± 0.07‰) to heavier compositions (as heavy as -0.15 ± 0.06‰). The heavy Mg isotope compositions are best explained by the addition of crustal materials during assimilation and fractional crystallization. The results show that Mg isotopes may be a valuable tracer of crustal input into a magma, supplementing more traditional methods.

Next, we investigate biosorption as a potential means of recovering REEs from non-traditional feedstocks. We examined how REE adsorption by engineered *E. coli* is controlled by various geochemical factors relevant to natural geofluids, including total dissolved solids (TDS), temperature, pH, and the presence of specific competing metals. REE biosorption is largely unaffected by high TDS concentrations, although high concentrations of some metals (e.g., U and Al) and decreasing pH below 5-6 were found to limit REE recovery. REE extraction efficiency and selectivity increase with temperature up to ~70°C, which is best explained by the thermodynamic properties of metal complexation on the bacterial surfaces. Together, these data demonstrate the potential utility of biosorption for selective REE recovery from geothermal fluids; however, the cells alone are generally not suitable for industrial-scale extraction operations. In the second portion of this section, we immobilize the engineered cells by encapsulating them in polyethylene glycol diacrylate (PEGDA) microparticles for use in fixed-bed columns. We demonstrate that optimal REE recovery (~2.6 mg Nd/g dry sorbent) occurs at an influent flow rate of ≤1 ml/min, pH of 6, and maximum REE concentration of ~21 mM. The microparticles exhibit minimal loss in performance

over >9 adsorption/desorption cycles. Furthermore, they have a strong preference for heavy REEs, particularly Eu, Sm, Yb, and Lu, which may permit the separation of individual rare earth metals. The results of this study represent a major step towards making biosorption a viable industrial scale REE extraction technology.

*To my parents, Laurie and Terry Brewer*
*and my sister, Katherine Brewer*

# ACKNOWLEDGEMENTS

This work is ultimately the result of the combined efforts of many people who provided their scientific expertise, personal and professional guidance, and “moral support.” I would first like to express my gratitude to my two primary supervisors, Dr. Fang-Zhen Teng and Dr. Yongqin Jiao. They are both leaders in their fields who contributed significantly to the conception and development of these projects throughout the duration of my Ph.D. Without them and their continued efforts, I would never have reached this point.

I would also like to thank my committee members Dr. Drew Gorman-Lewis and Dr. Bruce Nelson. Both have provided invaluable advice for my research efforts through the years. In particular, their feedback has greatly improved this dissertation. Dr. Dan Park, although not technically one of my supervisors, certainly deserves recognition for unofficially filling that role with such aplomb. I would also like to acknowledge Dr. Rory Barnes, my Graduate Student Representative, for being an excellent mentor and teacher and for his willingness to help. Undergraduate assistants often go without recognition proportional to their efforts, and I have truly been fortunate to have three undergraduates who went far above and beyond the expectations of their position. If their graduate student put out the call for some help in the lab, Khadijah Homolka, Jiarui Zhou, and Florence Yuen could always be counted on to be there, probably with a snack to share and a sarcastic comment about my failing work ethic.

Finally, some would see it as a sign of true megalomania to ignore the contributions of the people who raised him, so I feel obliged to acknowledge my parents, Laurie and Terry Brewer, and my sister, Katherine Brewer. Who can adequately describe the role of one’s family in the progression of their life, so I will leave it at that, and say a final thanks to everyone, named and unnamed, who has made this work possible.

# Table of Contents

## List of Figures

## List of Tables

# CHAPTER 1: INTRODUCTION

The research discussed here covers two distinct sections, which will be examined in sequence. The first section, using magnesium isotopes to trace weathered rock and elucidate biotic and abiotic weathering processes, is primarily the result of research performed at the University of Washington. The second section, applying microbes to selectively adsorb rare earth elements from various feedstock solutions, is the culmination of work conducted at Lawrence Livermore National Laboratory as part of the Livermore Graduate Scholar Program.

## *Part 1: Magnesium isotope fractionation associated with biotic and abiotic weathering and weathered materials*

Chemical weathering is a major determinant of the state of the atmosphere, hydrosphere, biosphere, and lithosphere. Silicate weathering, in combination with carbonate precipitation, removes carbon dioxide from the atmosphere, exerting a major influence on the atmospheric $CO_2$ budget (Urey, 1952). The chemical erosion and disintegration of igneous rocks provides the components for the formation of clays and other sedimentary rocks and affects river and seawater composition (Edmond et al., 1979). These aqueous weathering products are also essential for life, supplying many of the elements necessary for cell growth and metabolism. Finally, the subduction of weathered material can have an impact on the chemical composition of the middle and lower crust as well as upwelling magmas (Hofmann, 2003; Planck, 2014). Chemical weathering is therefore involved, directly or indirectly, in a wide range of geological processes.

Magnesium (Mg) is a major element that is abundant in the hydrosphere, biosphere, and lithosphere. Magnesium has three stable isotopes ($^{24}$Mg, $^{25}$Mg, and $^{26}$Mg), and many geochemical processes cause measurable mass dependent Mg isotope fractionation due to the 8% mass difference between $^{24}$Mg and $^{26}$Mg (Teng, 2017 and references therein). Although Mg isotope analyses have now been applied to the study of many of these processes, providing progress towards a systematic knowledge of Mg isotope behavior, some gaps remain in our understanding of this valuable geochemical tracer. Minimal Mg isotope fractionation is observed at high temperatures, so the compositions of uncontaminated mid-ocean ridge basalts and of the mantle are essentially homogeneous ($\delta^{26}$Mg = -0.25 ± 0.07‰ and -0.25 ± 0.04‰, respectively; Teng et al., 2010a). Magnesium leaching from igneous rocks into the hydrosphere during chemical weathering produces isotopically heavy residual rock, as high as +1.81 ‰, and a correspondingly light fluid phase (Tipper et al., 2008, 2010; Li et al., 2010; Teng et al., 2010b; Liu et al., 2014; Wimpenny et al., 2014). Although this preferential leaching of $^{24}$Mg may be generally representative of most chemical weathering systems, there are many additional processes that play variable roles in determining Mg isotope behavior in natural weathering environments.

A natural weathering system will involve primary mineral dissolution and alteration, secondary mineral formation, surface adsorption/desorption, biological processes, and potentially horizontal deposition of additional material. The final Mg isotope composition of a weathered sample will be the result of some combination of these processes, and may be informative about the weathering history of the sample. For example, Mg isotopes have been used to identify loess deposition in a weathering profile (Teng et al., 2010b) and can distinguish between adsorbed and structural Mg in secondary clay minerals (Wimpenny et al., 2014). Mg isotopes may similarly be used as a biosignature in the future, once the fractionation effects of various biological processes have been more systematically examined. The utility of Mg isotopes as an indicator of weathering will be more fully realized by assessing the distinct effects of individual weathering processes, the cumulative results of those processes in natural weathering systems, and the fate of weathered material in the environment.

Magnesium isotope behavior associated with biological processes has largely remained unexplored. Several studies have investigated Mg isotope behavior in plants (Black et al., 2006, 2008; Bolou-Bi et al., 2010, 2012; Uhlig et al., 2017), fungi (Fahad et al., 2016), and in biogenic carbonates (Higgins and Schrag, 2010; Immenhauser et al., 2010; Pokrovsky et al., 2011). Pokharel et al. (2017) assessed Mg isotope fractionation during uptake into microbes, but otherwise Mg interactions with microbial life have not been tested. The biosphere may play a particularly large and complex role in Mg isotope fractionation during chemical weathering. Microbes may influence Mg isotope behavior by increasing the rates of mineral dissolution and Mg release into the hydrosphere through direct surface adhesion, organic acid production, and/or the removal of aqueous dissolution products via uptake and adsorption (Lee and Fein, 2000; Wightman and Fein, 2004; Song et al., 2006). Uptake and adsorption may also affect the Mg isotope composition of the fluid phase, in addition to affecting weathering rates. These effects may be compared to Mg isotope behavior during purely chemical dissolution of specific minerals, which has been investigated for brucite (Li et al., 2014) and forsterite (Wimpenny et al., 2010).

Chapter 2 assesses the effects of cell surface reactivity on Mg isotope fractionation by studying forsterite dissolution in the presence of *Bacillus subtilis* endospores at various experimental conditions. Because endospores are metabolically dormant and do not produce significant organic acids, they affect the dissolution process only through cell surface reactivity (Olsen and Rimstidt, 2008; Song et al., 2006; Lee and Fein, 2000; Vandiviere et al., 1994; Harrold, 2014). Their sorption behavior is also generally representative of vegetative cell surfaces (Fein et al., 2005; Gorman-Lewis et al., 2006; Harrold and Gorman-Lewis, 2013), and they are therefore ideal for isolating the Mg isotope fractionation associated with cell surface reactivity in weathering systems. The endospore surfaces may affect Mg isotopes by attaching to the mineral surfaces to increase dissolution rate, and/or by interacting with the aqueous dissolution products. Dissolution assays with and without dialysis tubing preventing direct interaction between the mineral powder and the endospores permit those processes to be differentiated. In combination, the two assays show that the endospores do not appear to have an effect on Mg isotopes during Mg leaching from the forsterite over the analyzed time period (10-43 days). The compositions of the total dissolution products for the biotic and abiotic control assays are indistinguishable if all other processes are excluded. However, the endospores do cause an increase in the Mg isotope composition of the aqueous phase by preferentially adsorbing dissolved $^{24}$Mg. The original forsterite dissolution assays were performed by Zoe Harrold working under the supervision of Drew Gorman-Lewis at the University of Washington. Fang-Zhen Teng contributed to the conception of the Mg isotope component of this work. The results of this study are in the final stages of preparation to be submitted to *Geobiology*.

The laboratory dissolution experiments are informative because they permit an individual chemical process to be studied in isolation; however, natural weathering systems are the combined result of many distinct processes. For example, soil formation (Immenhauser et al., 2011; Ma et al., 2015) and clay mineral precipitation and surface chemistry (Huang et al., 2012; Ma et al., 2015; Opfergelt et al., 2014; Tipper et al., 2012; Wimpenny et al., 2014) may have a significant impact on the final composition of a weathering system in addition to mineral leaching and dissolution. The Mg isotope composition of several natural weathering profiles have been assessed to date, focusing mainly on mafic lithologies, such as basalt (Huang et al., 2012; Liu et al., 2014; Pogge von Strandmann et al., 2012) and diabase (Teng et al., 2010b), although one shale profile has also been analyzed (Ma et al., 2015). However, the Mg isotope composition of granite and granodiorite weathering profiles has not previously been the subject of systematic study. This gap in our understanding is significant because granites are the most abundant rock-type in the upper crust, while granodiorite is taken as representative of the bulk chemical composition of the upper crust (Rudnick and Gao, 2003; Wedepohl, 1995). Magnesium isotope analyses of granite and granodiorite weathering profiles may provide important insights into weathering on the continents and into the Mg cycle in these environments.

Chapter 3 investigates Mg isotope fractionation during granite and granodiorite weathering, specifically with regard to the dissolution and alteration of primary Mg-bearing minerals and the formation and behavior of secondary clay minerals. Mg isotope composition in these profiles was primarily the result of primary biotite weathering and the formation and weathering of secondary clay minerals, particularly illite. As biotite weathers, some $^{24}$Mg is preferentially lost to the hydrosphere, producing increased Mg isotope compositions from the bedrock until the upper ~2 m of the profiles. However, significant Mg is preserved in the rock through incorporation into secondary illite, minimizing the fractionation effect. At depths <2 m, illite begins to weather, causing a decrease in Mg isotope composition as the Mg content shifts from being primarily incorporated into structural sites in the illite to being primarily adsorbed onto the exchangeable sites of clays such as kaolinite. One hydrothermal profile does not follow this trend, exhibiting radically increased Mg isotope composition in the near-surface samples.

The study represents a significant step towards a thorough understanding of Mg isotope systematics in felsic, continental weathering environments. The samples were collected and assessed for chemical and mineralogical composition by David Dethier currently at Williams College. Fang-Zhen Teng procured the samples and provided his insight into the observed Mg isotope behavior. A manuscript detailing these results was published in *Chemical Geology* in October 2018.

Because weathering processes typically result in the preferential release of $^{24}$Mg into the hydrosphere, weathered silicate materials may have significantly elevated Mg isotope compositions (Tipper et al., 2008, 2010; Li et al., 2010; Teng et al., 2010b; Liu et al., 2014). This upper crustal Mg isotope signature can be preserved during subduction and assimilation into rising magmas to produce volcanic arc rocks with Mg isotope compositions that deviate from the canonical basalt value ($\delta^{26}$Mg = -0.25 ± 0.07‰; Teng et al., 2010a). The subduction of carbonates, for example, has been found to produce arc magmas with unusually light Mg isotope compositions (Yang et al., 2012; Huang et al., 2015). The preservation of the Mg isotope signature is possible because metamorphism has little effect on Mg isotopes, particularly at the conditions relevant to volcanic arcs (Geske et al., 2012; Li et al., 2011; Wang et al., 2015). Unlike carbonates, the incorporation of weathered silicate materials into a magma may result in an increased Mg isotope composition, which has been observed in some granites (Shen et al., 2009; Liu et al., 2010), but not previously at volcanic arcs.

The Northern Cascade Volcanic Arc represents an excellent location to assess the impacts of upper crustal material additions on the Mg isotope composition of arc magmas because it has produced samples with a known range of upper crustal contributions, including samples with no measurable crustal component (Mullen and Weis, 2013, 2015; Mullen and McCallum, 2014;

Mullen et al., 2017). Furthermore, the specific mechanism of crustal material addition (e.g., bulk mixing during subduction or assimilation and fractional crystallization) is also known to vary across the arc (Mullen and Weis, 2013, 2015; Mullen and McCallum, 2014; Mullen et al., 2017). By combining traditional geochemical tracers with Mg isotope systematics, Chapter 4 demonstrates that the addition of isotopically heavy upper crustal materials to primary magmas during assimilation and fractional crystallization may produce a small but measurable increase in Mg isotope composition. The addition of subducted materials appeared to have minimal effect on Mg isotopes in these samples. With further study and improvements in instrumental precision, Mg isotopes may prove to be a valuable tracer of upper crustal material in igneous rocks. Emily Mullen, then at the University of Washington, gathered and published much geochemical data for these samples, while Fang-Zhen Teng made significant contributions to the development of the project idea and interpretation of the results. This work was published in *Frontiers in Earth Sciences* in March 2018.

### *Part 2: Rare earth element extraction from non-traditional feedstocks using engineered* Escherichia coli

Rare earth elements (REEs), which consist of the lanthanide series metals, as well as scandium and yttrium, are becoming increasingly important to the international economy with the development and spread of new technologies, especially in the area of clean energy. The most common uses for REEs include automotive and industrial catalysts, metallurgical additives, and permanent magnets in wind turbines, electric motors, and electronic devices (DOE, 2011). However, the supply of these metals is potentially at risk globally because more than 85% of the world's REE production comes from China (Zhou et al., 2017), even though there are significant reserves elsewhere, including in the United States. REEs have been identified as critical materials by the European Union and the United States Department of Energy based on both their supply risk and their importance to the modern economy. Five REEs in particular (Tb, Dy, Eu, Nd, and Y) have been identified as especially critical (DOE, 2011). Given the limited sources of REE production and the increasing global demand for these metals, it is essential to investigate new REE feedstocks and to develop new and improved techniques for REE recovery and purification.

Rare earth elements are relatively abundant in the Earth's crust, despite their name, but they are not typically concentrated in easily exploitable ore deposits. Most REEs are currently mined from monazite, bastnasite, and ion adsorption clay minerals that require significant processing for REE recovery, often causing serious environmental problems, particularly in China where there is minimal regulation (Hennebel et al., 2015). There are, however, many promising non-traditional REE resources, such as coal byproducts and electronic waste, which are abundant and may provide a means of diversifying the world's REE supply. However, due to the low REE concentrations and/or adverse chemical characteristics of these potential resources, conventional REE-extraction approaches have not yet been applied at an industrial scale, and the resources remain unexploited. Therefore, the development of novel REE recovery methods designed specifically for use with non-traditional feedstocks is the focus of significant ongoing research efforts.

Solid-phase extraction (SPE) is one category of novel REE recovery technologies, which involves the application of a solid material to selectively adsorb REEs from an aqueous feedstock, such as a leachate or a naturally occurring geofluid. The extractant will have a high binding affinity for REEs compared to other, non-REE metals and will therefore concentrate and purify REEs in the solid phase. A targeted desorption scheme can then further purify the REEs from any co-adsorbed non-REEs and may also make possible the separation of individual REEs. Many SPE adsorbents have been tested, including organic wastes such as seafood (Takahashi et al., 2014) and vegetable byproducts (Varshini et al., 2014), various hydrogels (Bertagnolli et al., 2016), zero-valent iron particles (Crane and Sapsford, 2018), and mineral powders (Gok et al., 2014). Each of these materials has clear advantages and disadvantages for REE separation and purification purposes. For example, organic wastes are inexpensive, abundant, and environmentally-friendly; however, they may not have the high selectivity for REE adsorption that an engineered hydrogel will exhibit (Anastopolous et al., 2016). An ideal adsorbent would have both a high capacity and a high selectivity for REEs and would be cheap, readily available, mechanically and chemically stable, and environmentally friendly.

Microbes are a particularly promising REE-specific adsorbent given those criteria. Biosorption does not contribute to the hazardous chemical footprint of the REE extraction process, and microbes are relatively inexpensive and simple to produce even at a large scale (Jiang et al., 2012; Moriwacki and Yamamoto, 2013; Ozaki et al., 2004; Texier et al., 1999; Tsuruta, 2007). Furthermore, microbes can sustain multiple REE recovery cycles since the cells do not need to be viable to retain the desired cell surface reactivity (Park et al., 2016, 2017). Finally, native microbial cell surfaces typically exhibit a high selectivity for REEs and a high REE adsorption capacity for a given sorbent weight (Dodson et al., 2015; Jacinto et al., 2018; Lo et al., 2014). The inherent adsorptive properties of microbes have been enhanced by engineering the cells to express a lanthanide binding tag (LBT) on the cell surface (Park et al., 2016, 2017). In *E. coli* cells specifically, LBT expression increased REE adsorption capacity by ~2-fold and increased REE adsorption selectivity over every tested non-REE metal except copper (Park et al., 2017). With a comprehensive understanding of the adsorption characteristics of these LBT-displayed *E. coli* cells and the proper extraction system design, these microbes may permit the recovery of REEs from a variety of traditional and non-traditional feedstocks.

Geofluids are one promising REE feedstock given their abundance and the lack of pre-processing (e.g., crushing, beneficiation, and leaching) required before biosorption compared to solid REE feedstocks. Geofluids, including geothermal fluids, have a range of geochemical characteristics that make them unique compared to many other non-traditional feedstocks and which present unusual difficulties for REE extraction. Even the highest grade geofluids have total REE concentrations only up to low ppm levels, which is much lower than other non-traditional feedstocks, such as recycled electronic waste leachates which may reach REE concentrations in the thousands of ppm (Lixandru et al., 2017). Most geofluids do not even reach the low ppm threshold, and a typical fluid for REE recovery is often in the hundreds of ppb range (Wood et al., 2001). The high-REE geofluids typically have pH <3.5, which further complicates biosorption because the cell surfaces exhibit optimal REE recovery at pH 5-6, with decreasing recovery efficiency with decreasing pH (Wood et al., 2001; Park et al., 2016). Geofluids may also have extremely high ionic strength, high concentrations of specific, competitive non-REE metals, and high temperatures, all of which may have an impact on REE extraction.

Chapter 5 investigates the effects of pH, ionic strength, competing metal concentrations, and temperature on REE adsorption by the LBT-displayed *E. coli* cells. Ionic strength did not have a resolvable effect on REE recovery at the range of concentrations relevant to geofluids. Individual competing metals were capable of displacing REEs from the cell surface once their concentration reached a certain threshold, typically >10x higher than the REE concentrations. Decreasing pH blow pH 6 progressively reduced REE adsorption; however, increasing temperature up to 70°C improved REE adsorption. These results inform the use of biosorption techniques for REE recovery from natural geofluids. This chapter was submitted to *Environmental Science & Technology* and is currently in revision. Yongqin Jiao and Dan Park at Lawrence Livermore National Laboratory (LLNL), along with collaborators Laura Lammers and Elliot Chang at UC Berkeley and Yat Li and Tianyi Kou at UC Santa Cruz, made significant contributions to this study.

Although the LBT-displayed *E. coli* cells, and microbes in general, have many promising attributes for REE extraction purposes, particularly their advantageous surface chemistry, their physical characteristics make them difficult to apply at an industrial scale. Perhaps most critically, large-scale REE solid-phase extraction operations would benefit from a continuous flow design that maximizes feedstock exposure to the adsorbent. However, high densities of cells tend to obstruct flow, causing head loss and even clogging. To address this issue, the cells may be immobilized, often by imbedding them in a permeable material, such as a polymer. Ideally, this immobilization technique will produce an adsorbent with the advantageous chemical characteristics of the cells and the advantageous physical characteristics of the polymer. The selected polymers must be biocompatible, highly permeable, easy to synthesize, chemically and mechanically stable, and minimally adsorptive. While many polymers, such as alginate, have previously been used for cell immobilization because they meet the first four criteria, these materials commonly adsorb significant amounts of non-REE metals, and are therefore not suitable for REE recovery applications.

Chapter 6 describes the development of a method to produce polyethylene glycol diacrylate (PEGDA) microparticles, or matrix-style capsules, with a high concentration of LBT-displayed *E. coli* cells, and then demonstrates the function of these microparticles in continuous flow REE extraction columns at conditions relevant to REE feedstocks. In a breakthrough column system, increasing flow rate, decreasing pH, and decreasing REE concentration in the feedstock all decreased the REE adsorption of the microparticle sorbent from a baseline of ~3 mg REEs for each g of dry sorbent. Columns largely retained function through the course of 9 adsorption/desorption cycles, suggesting excellent reusability. The chapter concludes with the successful recovery of REEs from real-world leachates of electronic waste and lignite coal, showing that the cell/PEGDA microparticles are a practical, scalable adsorbent for REE recovery from non-traditional feedstocks. Yongqin Jiao, Dan Park, and Congwang Ye at LLNL were instrumental in the completion of this work, with support from Laura Lammers and Elliot Chang at UC Berkeley, Yat Li and Shanwen Wang at UC Santa Cruz, and Heileen Hsu-Kim and Ryan Smith at Duke University. The manuscript detailing the results of this study is in preparation to be submitted to *ACS Applied Materials & Interfaces*.

## References

Anastopoulos, I.; Bhatnagar, A.; Lima, E.C. (2016) Adsorption of rare earth metals: A review of recent literature. Journal of Molecular Liquids, 221, 954-962.

Bertagnolli, C.; Grishin, A.; Vincent, T.; Guibal, E. (2016) Recovering Heavy Metal Ions from Complex Solutions Using Polyethylenimine Derivatives Encapsulated in Alginate Matrix. Industrial & Engineering Chemistry Research, 55, (8), 2461-2470.

Black, J.R., Yin, Q.-Z., Casey, W.H. (2006) An experimental study of magnesium-isotope fractionation in chlorophyll-a photosynthesis. Geochimica et Cosmochimica Acta 70, 4072-4079.

Black, J.R., Epstein, E., Rains, W.D., Yin, Q.-Z., Casey, W.H. (2008) Magnesium-isotope fractionation during plant growth. Environmental Science & Technology 42, 7831-7836.

Bolou-Bi, E.B., Poszwa, A., Leyval, C., Vigier, N. (2010) Experimental determination of magnesium isotope fractionation during higher plant growth. Geochimica et Cosmochimica Acta 74, 2523-2537.

Bolou-Bi, E.B., Vigier, N., Poszwa, A., Boudot, J.-P., Dambrine, E. (2012) Effects of biogeochemical processes on magnesium isotope variations in a forested catchment in the Visges Mountains (France). Geochimica et Cosmochimica Acta 87, 341-355.

Crane, R.A.; Sapsford, D.J. (2018) Sorption and fractionation of rare earth element ions onto nanoscale zerovalent iron particles. Chemical Engineereing Journal, 345, 126-137.

Dodson, J. R.; Parker, H. L.; Garcia, A. M.; Hicken, A.; Asemave, K.; Farmer, T. J.; He, H.; Clark, J. H.; Hunt, A. J. (2015) Bio-derived materials as a green route for precious & critical metal recovery and re-use. Green Chemistry, 17, (4), 1951-1965.

DOE, Critical Materials Strategy Report. In 2011.

Edmond, J.M., Measures, C., McDuff, R.E., Chan, L.H., Collier, R., Grant, B., Gordon, L.I., Corliss, J.B. (1979) Ridge crest hydrothermal activity and the balances of the major and minor elements in the ocean: The Galapagos data. Earth and Planetary Science Letters 46, 1-18.

Fahad, Z.A., Bolou-Bi, E.B., Kohler, S.J., Finlay, R.D., Mahmood, S. (2016) Fractionation and assimilation of Mg isotopes by fungi is species dependent. Environmental Microbiology Reports, 8, 956-965.

Fein, J.B., Boily, J.-F., Yee, N., Gorman-Lewis, D., Turner, B.F. (2005) Potentiometric titrations of *Bacillus subtilis* cells to low pH and a comparison of modeling approaches. Geochimica et Cosmochimica Acta 69, 1123-1132.

Geske, A., Zorlu, J., Richter, D.K., Buhl, D., Niedermayr, A., Immenhauser, A. (2012) Impact of diagenesis and low grade metamorphosis on isotope ($\delta^{26}$Mg, $\delta^{13}$C, $\delta^{18}$O and $^{87}$Sr/$^{88}$Sr) and elemental (Ca, Mg, Mn, Fe and Sr) signatures of Triassic sabkha dolomites. Chemical Geology 332-333, 45-64.

Gok, C. (2014) Neodymium and samarium recovery by magnetic nano-hydroxyapatite. Journal of Radioanalytical and Nuclear Chemistry, 301, (3), 641-651.

Gorman-Lewis, D., Fein, J.B., Jensen, M.P. (2006) Enthalpies and entropies of proton and cadmium adsorption onto Bacillus subtilis bacterial cells from calorimetric measurements. Geochimica et Cosmochimica Acta 70, 4862-4873.

Harrold, Z.R., (2014) Investigating the effects of Bacillus subtilis endospore surface reactivity on low-temperature aqueous geochemical systems. Doctoral dissertation. University of Washington, Seattle, WA, USA.

Harrold, Z.R., Gorman-Lewis, D. (2013) Thermodynamic analysis of Bacillus subtilis endospore protonation using isothermal titration calorimetry. Geochimica et Cosmochimica Acta,109, 296-305.

Higgins, J.A., Schrag, D.P. (2010) Constraining magnesium cycling in marine sediments using magnesium isotopes. Geochimica et Cosmochimica Acta 74, 5039-5053.

Hennebel, T.; Boon, N.; Maes, S.; Lenz, M. (2015) Biotechnologies for critical raw material recovery from primary and secondary sources: R&D priorities and future perspectives. New Biotechnology, 32, (1), 121-127.

Hofmann, A.W. (2003) Sampling mantle heterogeneity through oceanic basalts: Isotopes and trace elements, in: Carlson, R.W., (Ed.), The Mantle and Core. Treatise on Geochemistry. Elsevier-Pergamon, Oxford, pp. 61-101.

Huang, K.-J., Teng, F.-Z., Wei, G.-J., Ma, J-.L., Bao, Z.-Y. (2012) Adsorption- and desorption-controlled magnesium isotope fractionation during extreme weathering of basalt in Hainan Island, China. Earth and Planetary Science Letters 359-360, 73-83.

Immenhauser, A., Buhl, D., Richter, D., Niedermayer, A., Reichelmann, D., Dietzel, M., Schulte, U. (2010) Magnesium-isotope fractionation during low-Mg calcite precipitation in a limestone cave – Field study and experiments. Geochimica et Cosmochimica Acta, 74, 4346-4364.

Jacinto, J.; Henriques, B.; Duarte, A. C.; Vale, C.; Pereira, E. (2018) Removal and recovery of Critical Rare Elements from contaminated waters by living *Gracilaria gracilis*. Journal of Hazardous Materials, 344, 531-538.

Jiang, M. Y.; Ohnuki, T.; Tanaka, K.; Kozai, N.; Kamiishi, E.; Utsunomiya, S. (2012) Post-adsorption process of Yb phosphate nano-particle formation by *Saccharomyces cerevisiae*. Geochimica et Cosmochimica Acta, 93, 30-46.

Lee, J.-U. and Fein, J.B. (2000) Experimental study of the effects of *Bacillus subtilis* on gibbsite dissolution rates under near-neutral pH and nutrient-poor conditions. Chemical Geology, 166, 193-202.

Li, W., Beard, B.L., Li, C., Johnson, C.M. (2014) Magnesium isotope fractionation between brucite [$Mg(OH)_2$] and Mg aqueous species: Implications for silicate weathering and biogeochemical processes. Earth and Planetary Science Letters 394, 82-93.

Li, W.-Y., Teng, F.-Z., Ke, S., Rudnick, R. L., Gao, S., Wu, F.-Y., Chappell, B. W. (2010) Heterogeneous magnesium isotopic composition of the upper continental crust. Geochimica et Cosmochimica Acta 74, 6867–6884.

Li, W.-Y., Teng, F.-Z., Xiao, Y., Huang, J. (2011) High-temperature inter-mineral magnesium isotope fractionation in eclogite from the Dabie orogeny, China. Earth and Planetary Science Letters 224-230.

Liu, S.A., Teng, F.-Z., He, Y., Ke, S., Li, S. (2010) Investigation of magnesium isotope fractionation during granite differentiation: Implication for Mg isotopic composition of the continental crust. Earth and Planetary Science Letters 297, 646-654.

Liu, X.-M., Teng, F.-Z., Rudnick, R.R., McDonough, W.F., Cummings, M.L. (2014) Massive magnesium depletion and isotope fractionation in weathered basalts. Geochimica et Cosmochimica Acta, 135, 336–349.

Lixandru A, Venkatesan P, Jönsson C, Poenaru I, Hall B, Yang Y, Walton, A., Guth, K., Gaus, R., Gutfleisch, O. (2017) Identification and recovery of rare-earth permanent magnets from waste electrical and electronic equipment. Waste Management, 68:482-9.

Lo, Y. C.; Cheng, C. L.; Han, Y. L.; Chen, B. Y.; Chang, J. S. (2014) Recovery of high-value metals from geothermal sites by biosorption and bioaccumulation. Bioresource Technology, 160, 182-190.

Ma, L., Teng, F.-Z., Jin, L., Ke, S., Yang, W., Gu, H.-O., Brantley, S.L. (2015) Magnesium isotope fractionation during shale weathering in the Shale Hills Critical Zone Observatory: Accumulation of light Mg isotopes in soils by clay mineral transformation. Chemical Geology, 397, 37-50.

Moriwaki, H.; Yamamoto, H. (2013) Interactions of microorganisms with rare earth ions and their utilization for separation and environmental technology. Applied Microbiology and Biotechnology, 97, (1), 1-8.

Mullen, E.K., McCallum, I.S. (2014). Origin of Basalts in a Hot Subduction Setting: Petrological and Geochemical Insights from Mt. Baker, Northern Cascade Arc. Journal of Petrology 55(2):241-281.

Mullen, E.K., Weis, D. (2013) Sr-Nd-Nf-Pb isotope and trace element evidence for the origin of alkali basalts in the Garabaldi Belt, northern Cascade arc. Geochemistry, Geophysics, and Geosystems, 14:3126-3155.

Mullen, E.K., Weis, D. (2015). Evidence for trench-parallel mantle flow in the northern Cascade Arc from basalt geochemistry Earth and Planetary Science Letters 414:100-107.

Mullen, E.K., Weis, D., Marsh, N.B., Martindale, M. (2017). Primitive arc magma diversity: New geochemical insights in the Cascade Arc. Chemical Geology, 448:43-70.

Olsen, A.A., Rimstidt, J.D. (2008) Oxalate-promoted forsterite dissolution at low pH. Geochimica et Cosmochimica Acta, 72, 1758–1766.

Opfergelt, S., Burton, K.W., Georg, R.B., West, A.J., Guicharnaud, R.A. Sigfusson, B., Siebert, C., Gislason, S.R., Halliday, A.N. (2014) Magnesium retention on the soil exchange complex controlling Mg isotope variations in soils, soil solutions and vegetation in volcanic soils, Iceland. Geochimica et Cosmochimica Acta, 125, 110-130.

Ozaki, T.; Gillow, J. B.; Kimura, T.; Ohnuki, T.; Yoshida, Z.; Francis, A. J. (2004) Sorption behavior of europium(III) and curium(III) on the cell surfaces of microorganisms. Radiochimica Acta, 92, (9-11), 741-748.

Park, D. M.; Reed, D. W.; Yung, M. C.; Eslamimanesh, A.; Lencka, M. M.; Anderko, A.; Fujita, Y.; Riman, R. E.; Navrotsky, A.; Jiao, Y. Q. (2016) Bioadsorption of Rare Earth Elements through Cell Surface Display of Lanthanide Binding Tags. Environmental Science & Technology, 50, (5), 2735-2742.

Park, D. M.; Brewer, A.; Reed, D. W.; Lammers, L. N.; Jiao, Y. (2017) Recovery of Rare Earth Elements from Low-Grade Feedstock Leachates Using Engineered Bacteria. Environmental Science & Technology, 51, (22), 13471-13480.

Plank, T. (2014) The chemical composition of subducting sediments, in: Rudnick, R.L., (Ed.) The Crust. Treatise on Geochemistry. Elsevier, Oxford, pp. 607-629.

Pokharel, R., Gerrits, R., Schuessler, J.A., Floor, G.H., Gorbushina, A.A., von Blanckenburg, F. (2017) Mg isotope fractionation during uptake by a rock-inhabiting, model microcolonial fungus *Knufia petricola* at acidic and neutral pH. Environmental Science & Technology, 51, 9691-9699.

Pokrovsky, B.G., Mavromatis, V., Pokrovsky, O.S. (2011) Co-variation of Mg and C isotopes in late Precambrian carbonates of the Siberian Platform: A new tool for tracing the change in weathering regime? Chemical Geology, 290, 67-74.

Rudnick, R.L., Gao, S. (2003) Composition of the Continental Crust, in: Carlson, R.W., (Ed.), The Crust. Treatise on Geochemistry. Elsevier-Pergamon, Oxford, pp. 1-64.

Shen, B., Jacobsen, B., Lee, C.-T.A., Yin, Q.-Z., Morton, D.M. (2009) The Mg isotopic systematics of granitoids in continental arcs and implications for the role of chemical weathering in crust formation. Proceedings of the National Academy of Sciences, 106, 20652-20657.

Song, W., Ogawa, N., Oguchi, C.T., Hatta, T., Matsukua, Y. (2006) Effect of Bacillus subtilis on granite weathering: A laboratory experiment. Catena 70, 275-281.

Takahashi, Y.; Kondo, K.; Miyaji, A.; Watanabe, Y.; Fan, Q.; Honma, T.; Tanaka, K. (2014) Recovery and Separation of Rare Earth Elements Using Salmon Milt. PLOS ONE, 9, (12), e114858.

Teng, F.-Z., Li, W.-Y., Ke, S., Marty, B., Dauphas, N., Huang, S., Wu F. Y., Pourmand, A. (2010a) Magnesium isotopic composition of the Earth and chondrites. Geochimica et Cosmochimica Acta 74, 4150–4166.

Teng, F.-Z., Li, W.-Y., Rudnick, R.L., Gardner, L.R. (2010b) Contrasting lithium and magnesium isotope fractionation during continental weathering. Earth and Planetary Science Letters 300, 63-71.

Teng, F.-Z. (2017) Magnesium Isotope Geochemistry. Reviews in Mineralogy and Geochemistry vol. 82, 219-287.

Texier, A. C.; Andres, Y.; Le Cloirec, P. (1999) Selective biosorption of lanthanide (La, Eu, Yb) ions by Pseudomonas aeruginosa. Environmental Science & Technology, 33, (3), 489-495.

Tipper, E.T., Gaillardet, J., Louvat, P., Capmas, F., White, F. (2010) Mg isotope constraints on soil pore-fluid chemistry: Evidence from Santa Cruz, California. Geochimica et Cosmochimica Acta 74, 3883-3896.

Tipper, E.T., Galy, A., Bickle, M.J. (2008) Calcium and magnesium isotope systematics in rivers draining the Himalaya-Tibetan-Plateau region: Lithological or fractionation control? Geochimica et Cosmochimica Acta 72, 1057-1075.

Tipper, E.T., Calmels, D., Gaillardet, J., Louvat, P., Capmas, F., Dubacq, B. (2012) Positive correlation between Li and Mg isotope ratios in the river waters of the Mackenzie Basin challenges the interpretation of apparent isotopic fractionation during weathering. Earth and Planetary Science Letters 333-334, 35-45.

Tsuruta, T. (2007) Accumulation of rare earth elements in various microorganisms. Journal of Rare Earths 25, (5), 526-532.

Uhlig, D., Schuessler, J.A., Bouchez, J., Dixon, J.L., von Blanckenburg, F. (2017) Quantifying nutrient uptake as a driven of rock weathering in forest ecosystems by magnesium stable isotopes. Biogeosciences 14, 3111-3128.

Urey, H.C., 1952. The Planets: Their Origin and Development. Yale University Press, New Haven, CT. 245 pp.

Vandevivere, P., Welch, S.A., Ullman, W.J., Kirchman, D.L. (1994) Enhanced Dissolution of Silicate Minerals by Bacteria at Near-Neutral pH. Microbial Ecology 27, 241-251.

Varshini, J. S. C., Nilanjana, D. (2014) Screening of biowaste materials for the sorption of cerium (III) from aqueous environment. Research Journal of Pharmaceutical, Biological and Chemical Sciences 5, 402-408.

Wang, S.-J., Teng, F.-Z., Li, S.-G., Hong, J.-A. (2015) Magnesium isotopic systematics of mafic rocks during continental subduction. Geochimica et Cosmochimica Acta 143, 34-48.

Wedepohl, K.H. (1995) The composition of the continental crust. Geochimica et Cosmochimica Acta 59, 1217-1232.

Wightman, P.G., Fein, J.B. (2004) The effect of bacterial cell wall adsorption on mineral solubilities. Chemical Geology 212, 247-254.

Wimpenny, J., Gislason, S.R., James, R.H., Gannoun, A., Pogge von Strandmann, P.A.E., Burton, K.W. (2010) The behavior of Li and Mg isotopes during primary phase dissolution and secondary mineral formation in basalt. Geochimica et Cosmochimica Acta 74, 5259-5279.

Wimpenny, J., Colla, C.A., Yin, Q.-Z., Rustad, J.R., Casey, W.H. (2014) Investigating the behavior of Mg isotopes during the formation of clay minerals. Geochimica et Cosmochimica Acta 128, 178-194.

Wood, S. A. (2001) Behavior of rare earth elements in geothermal systems: A new exploration/exploitation tool? In DOE, Ed. Geothermal Reservoir Technology Research.

Yang, W., Teng, F.-Z., Zhang, H.-F., Li S.-G. (2012) Magnesium isotopic systematics of continental basalts from the North China craton: Implications for tracing subducted carbonate in the mantle. Chemical Geology 328, 185-194.

Zhou, B. Li, Z.;Chen, C. (2017) Global potential of rare earth resources and rare earth demand from clean technologies. Minerals 7, 1-14.

# CHAPTER 2: Magnesium isotope fractionation during microbially enhanced forsterite dissolution

This chapter is in preparation for publication as:

*Brewer, A.B., Harrold, Z., Chang, E., Gorman-Lewis, D., Teng, F.-Z., (2018) Magnesium isotope fractionation during microbially enhanced forsterite dissolution. Geobiology.*

## Abstract

A series of *Bacillus subtilis* endospore-mediated forsterite dissolution experiments were performed to assess the effects of cell surface reactivity on Mg isotope fractionation during chemical weathering. During abiotic control assays, $^{24}$Mg was preferentially released into solution during dissolution, producing an isotopically light liquid ($\delta^{26}$Mg = -0.39 ± 0.06 to -0.26 ± 0.09 ‰) relative to the initial mineral composition ($\delta^{26}$Mg = -0.24 ± 0.03 ‰). The presence of endospores did not have an apparent effect on Mg isotope fractionation associated with dissolution; rather, the endospore surfaces preferentially adsorbed $^{24}$Mg from solution, which resulted in heavy aqueous Mg isotope compositions (up to $\delta^{26}$Mg = -0.08 ± 0.07 ‰). Aqueous Mg isotope composition increased proportional to the fraction of dissolved Mg that was adsorbed by the endospores, with the highest measured $\delta^{26}$Mg occurring at the highest degree of adsorption (~76%). Secondary mineral precipitation and Mg adsorption onto secondary minerals had a minimal effect on Mg isotopes. These results demonstrate the isolated effect of cell surface reactivity on Mg isotope fractionation, separate from other common biological processes, such as metabolism and organic acid production. With further study, Mg isotopes could be used to elucidate the role of the biosphere on Mg cycling in the environment.

# 1. Introduction

Silicate weathering exerts a major geochemical influence on the state of the atmosphere, hydrosphere, biosphere, and lithosphere. For example, chemical weathering of silicates releases ions, such as calcium and magnesium, that promote carbonate precipitation, sequestering atmospheric carbon dioxide in carbonate rock and affecting the long-term atmospheric $CO_2$ budget (Urey, 1952). The products of chemical weathering supply the building blocks for clays and other secondary minerals and are a major determinant of river and ultimately ocean water composition. These silicate weathering products, such as magnesium, are also integral to life, providing the components necessary for cell growth and metabolism.

Magnesium (Mg) isotope behavior is sensitive to the various processes involved in chemical weathering, and may therefore be a valuable tracer of these processes. Magnesium, a major element found in significant concentrations in the hydrosphere, biosphere, and lithosphere, has three stable isotopes ($^{24}$Mg, $^{25}$Mg, and $^{26}$Mg). The 8% mass difference between $^{24}$Mg and $^{26}$Mg results in observable mass dependent isotope fractionation, particularly during low-temperature, near-surface processes (Teng, 2017 and references therein). In the context of weathering-related processes, Mg isotopes are fractionated during, for example, primary mineral dissolution, secondary mineral formation, and surface adsorption. The leaching of Mg from igneous rocks into the hydrosphere during weathering has been shown to produce isotopically heavy residual rock, as heavy as +1.81 ‰ (Li et al., 2010; Liu et al., 2014; Teng et al., 2010b; Tipper et al., 2008, 2010; Wimpenny et al., 2014). The aqueous phase tends to be correspondingly isotopically light depending upon the degree of weathering and additional factors (Huang et al., 2012; Liu et al., 2014; Pogge von Strandmann et al., 2012; Teng et al., 2010b; Wimpenny et al., 2010, 2014). The formation of secondary minerals can have a variable effect on Mg isotopes, with carbonate precipitates typically exhibiting a light Mg isotope composition (as light as -5.6 ‰; Wombacher et al., 2011), while clay minerals preferentially incorporate $^{26}$Mg into their structural sites and are generally isotopically heavy (Huang et al., 2012; Li et al., 2010; Ma et al., 2015; Opfergelt et al., 2014; Tipper et al., 2012; Wimpenny et al., 2014). Magnesium adsorbed onto mineral surfaces has been found to be variably heavy (Huang et al., 2012; Liu et al., 2014b; Pogge von Strandmann et al., 2012) or light (Brewer et al., 2018; Ma et al., 2015; Opfergelt et al., 2012, 2014; Wimpenny et al., 2014), and the mechanisms responsible for these differences are not well understood. Magnesium isotope fractionation during adsorption and desorption are therefore active areas of investigation. Despite the progress that has been made in assessing Mg isotope behavior during chemical weathering, the role of biological processes in weathering systems has not been the focus of much study. Magnesium isotope fractionation in plants has been investigated (Black et al., 2006, 2008; Bolou-Bi et al., 2010, 2012; Uhlig et al., 2017), as has the increased Mg isotope composition associated with uptake into microbial cells (Pokharel et al., 2017) and fungi (Fahad et al., 2016). However, Mg isotopes have not previously been applied to specifically elucidate the effects of biological surface chemistry on chemical weathering.

Microbes are ubiquitous in weathering environments and are known to increase rates of mineral dissolution (Lee and Fein, 2000; Song et al., 2007; Vandevivere et al., 1994), potentially exerting a major control on the flux of dissolution products into the hydrosphere. It can be difficult to distinguish the effects of biotic weathering from purely chemical weathering, particularly given the range of conditions and processes relevant to each. Both biotic and abiotic weathering can vary with temperature, pressure, pH, and surface area, among other factors (Bennett et al., 2001; Oelkers et al., 2001; Olsen and Rimstidt, 2008; Rogers and Bennett, 2004;

Vandeviere et al., 1994). Biotic weathering, however, is also dependent on cell wall reactivity and the metabolism of the microorganisms present, as well as any organic acids that they produce (Lee and Fein, 2000; Song et al., 2006; Wightman and Fein, 2004). Each of these biological factors may influence a natural weathering system in a variety of ways, and Mg isotopes may help to assess the contributions of these variables.

Bacterial cell wall reactivity can have significant direct and indirect effects on mineral dissolution in a weathering system (Friis et al., 2003; Oelkers et al., 2015; Wightman and Fein, 2004). The reactive sites on the cell wall can interact directly with a mineral surface, making dissolution more thermodynamically favorable; however, they can also adsorb the aqueous dissolution products, changing the saturation state of the solution and preventing the system from approaching equilibrium, which indirectly maintains a more rapid dissolution rate (Friis et al., 2003; Oelkers et al., 2015; Wightman and Fein, 2004). Their high surface reactivity is due to the high concentration of ion adsorption sites, such as carboxyl and phosphate ligands, on cell surfaces (Borrok et al., 2004; Gorman-Lewis et al., 2006; Harrold and Gorman-Lewis, 2013; Kelly et al., 2001, 2002). In environments where cell metabolism is slow and/or the microbial surface area is large, the two-fold effects of cell surface reactivity on chemical weathering may potentially be more significant than those of active metabolism or organic acid production.

Bacterial endospores present a unique opportunity to isolate the effects of microbial surface reactivity on Mg isotope fractionation. Endospores are a metabolically dormant cell type that can be produced by certain bacterial genera (e.g. *Bacillus* and *Clostridium*) under conditions not conducive to life. These endospores can survive high levels of radiation, toxic chemical exposure, and the absence of nutrients, among other harsh conditions, and can persist for many years (Siala et al., 1974; Whitman et al., 1998). Endospores are therefore common constituents of the bacterial biomass in many environments (Siala et al., 1974; Whitman et al., 1998). While mineral dissolution in the presence of vegetative microbial cells is complicated by metabolism and the production of organic acids, endospores only affect dissolution through cell wall reactivity (Daughney et al., 2001, 2002; Harrold, 2014; Lee and Fein, 2000; Olsen and Rimstidt, 2008; Song et al., 2006; Vandiviere et al., 1994). The cell wall reactivity of endospores is taken as generally representative of vegetative bacterial cell wall reactivity for the purposes of this study (Fein et al., 2005; Gorman-Lewis et al., 2006; Harrold and Gorman-Lewis, 2013). The application of endospores in controlled forsterite dissolution experiments permits the effects of cell wall reactivity on the fractionation of Mg isotopes during weathering to be assessed.

## 2. Materials and Methods

### *2.1. Endospore Preparation*

A detailed discussion of endospore growth and separation can be found in Harrold et al., (2011). Briefly, *B. subtilis* was aseptically inoculated into 3.5 ml 3% typticase soy broth (TSB) and 0.5% yeast extract for 24 hours. The broth cultures were then transferred to 1 L of 0.3% TSB for a further incubation of 6 days at 32°C. The biomass was harvested via centrifugation and washed three times by suspension in 0.1 M NaCl. The suspension was pelleted via centrifugation and the supernatant was discarded each time. The biomass was suspended in MQ water and added to a 2-phase extraction system comprised of 11.18% w/v PEG 4000, 34% v/v potassium phosphate buffer, and 50% v/v MQ water. This mixture was centrifuged, resulting in phase separation, and the top phase containing the endospores was collected, leaving the vegetative cells behind within the lower phase. The endospores were pelleted via centrifugation and washed five times by suspension in $NaClO_4$. The final endospore yield was weighed, and a 50 µl cut taken to quantify vegetative cell contamination. The average purity for this endospore harvesting method was 88 ± 11 % (1σ).

### *2.2. Forsterite Preparation*

All forsterite dissolution assays used powdered, naturally occurring San Carlos forsterite ($Mg_{1.8}Fe_{0.2}(Ni,Mn,Ca,Cr)_{0.01}SiO_4$, $Fo_{90}$; Harrold, 2014) at a concentration of 1.25 g $L^{-1}$. The $Fo_{90}$ had minimal contamination from other mafic minerals or secondary precipitates. The particle size ranged from 50 to 125 μm and exhibited variable surface area, from 0.6 to 4 $m^2$ $g^{-1}$ at an average of 2.5 ± 1.7 (1σ, n = 8), likely due to the large range in grain size (Harrold, 2014).

### *2.3. Direct and indirect dissolution experiments*

All dissolution experiments were conducted previously for Harrold (2014). All dissolution assays were conducted over an incubation period of 43 days. The bulk solution used was 25 mM $NaClO_4$ made with 18 MΩ $cm^{-1}$ $H_2O$, and the biotic assay endospore concentration was 0.65 g $L^{-1}$. Abiotic control assays were conducted under the same conditions as the biotic assays, but without endospores. Solution pH and temperature were maintained at 7.5 ± 0.3 and 23 ± 0.3°C, respectively, for the duration of the experiments. All assays were run in duplicate. For the purpose of Mg isotope analyses, the data from the duplicates were combined into a single time series.

Two different biotic dissolution assays were conducted in order to elucidate indirect versus direct impacts of endospore surfaces on forsterite dissolution. Indirect endospore-mineral interactions were assessed by isolating forsterite powder in 1 mL dialysis capsules (Spectra/Por Float-a-lyzer G2) with a molecular weight cut off (MWCO) of 1000 kD (~0.1 μm) to prevent direct contact between the endospores and the mineral surfaces. Only dissolution products with a

MW less than 1000 kD could pass through the dialysis barrier and equilibrate with the bulk solution. The assays were mixed continuously and sampled at regular intervals. Cations that passed through the 0.1 um filter are operationally defined as dissolved. Coupled direct and indirect endospore-forsterite interactions were assessed in assays where forsterite powder and endospores were added together into the same solution, permitting direct contact between the cell and mineral surfaces. All assays were continuously mixed end-over-end to maintain a homogeneous solution of endospores and mineral powder. Once collected, samples from both indirect and direct assays were passed through a 0.1 or 0.22 μm Millipore Isopore membrane filter, pH adjusted if necessary, and stored at 4 °C prior to chemical analysis.

The forsterite dissolution assays without endospores provide a baseline for Mg behavior during abiotic dissolution in the 25 mM $NaClO_4$ solution matrix. The abiotic dialysis and homogenous assays behaved similarly in terms of dissolution rate and dissolution product composition, indicating that the dialysis tubing itself had minimal impact on abiotic forsterite dissolution (Fig. 1). During the incubation period from which samples were analyzed for Mg isotopes (10-43 days), the dissolution rates for the dialysis and homogenous assays were approx. equivalent at $-11.38 \pm 0.07$ and $-11.39 \pm 0.34$ $molg^{-1}s^{-1}$ (2SD; Harrold, 2014). These rates are similar to those from previous studies (Olsen and Rimstidt, 2008; Pokrovsky and Schoot, 2000; Wogelius and Walther, 1991). Both assays also exhibit congruent forsterite dissolution over the entire incubation period, with an approximate aqueous Mg:Si ratio of 1.80:1 ($1.63 \pm 0.62$ and $1.72 \pm 0.30$, 2SD, for the dialysis and homogenous assays, respectively), reflecting the initial composition of the mineral powder (Harrold, 2014; Fig. 1). The abiotic assays provide a basis for comparison to assess the effects of endospores on forsterite dissolution.

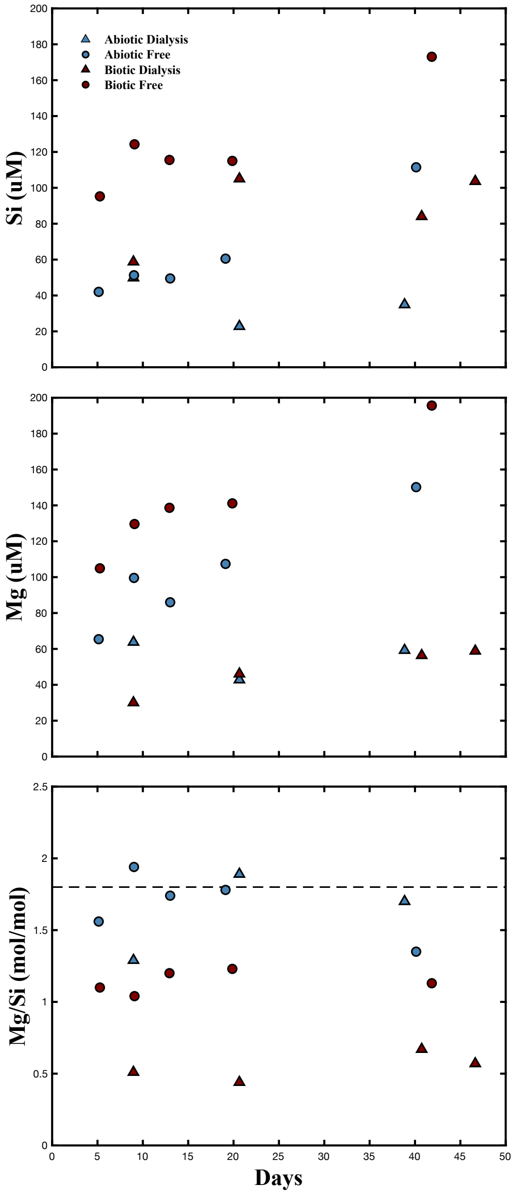

**Figure 1:** (a) Mg concentration (µM), (b) Si concentration (µM), and (c) Mg:Si ratio in solution over the duration of the incubation period. The triangles represent the dialysis assays and the circles represent the homogenous assays, while the red and blue symbols represent the biotic and abiotic assays, respectively. The dashed line in Panel C represents the Mg:Si ratio of the pristine forsterite. Data are from Harrold (2014). Data are reported in Table 1.

| **Incubation Period (days)** | **$\delta^{26}$Mg (‰)** | **2SD** | **$\delta^{25}$Mg (‰)** | **2SD** | **Mg Concentration (ppm)** | **Si Concentration (ppm)** | **Mg/Si** |
|---|---|---|---|---|---|---|---|
| *Abiotic Free Assay* | | | | | | | |
| 10 | -0.36 | 0.06 | -0.17 | 0.07 | 1.59 | 1.18 | 1.56 |
| 16 | -0.34 | 0.06 | -0.19 | 0.07 | 2.42 | 1.44 | 1.94 |
| 20 | -0.39 | 0.06 | -0.18 | 0.07 | 2.09 | 1.39 | 1.74 |
| 26 | -0.37 | 0.06 | -0.18 | 0.07 | 2.61 | 1.70 | 1.76 |
| 37 | -0.28 | 0.06 | -0.12 | 0.07 | 3.65 | 3.13 | 1.58 |
| **Avg** | **-0.35** | **0.08** | **-0.17** | **0.06** | **2.47** | **1.77** | **1.72** |
| *Abiotic Dialysis Assay* | | | | | | | |
| 17 | -0.33 | 0.06 | -0.17 | 0.07 | 1.55 | 1.40 | 1.29 |
| 30 | -0.26 | 0.09 | -0.08 | 0.11 | 1.04 | 0.64 | 1.89 |
| 39 | -0.35 | 0.05 | -0.19 | 0.07 | 1.44 | 0.98 | 1.70 |
| **Avg** | **-0.31** | **0.09** | **-0.15** | **0.12** | **1.34** | **1.01** | **1.63** |
| *Endospore Dialysis Assay* | | | | | | | |
| 17 | -0.12 | 0.07 | -0.04 | 0.06 | 0.73 | 1.65 | 0.51 |
| 30 | -0.08 | 0.07 | +0.02 | 0.06 | 1.12 | 2.95 | 0.44 |
| 36 | -0.10 | 0.06 | -0.01 | 0.07 | 1.37 | 2.36 | 0.67 |
| 41 | -0.17 | 0.06 | -0.10 | 0.07 | 1.43 | 2.91 | 0.57 |
| 43 | -0.10 | 0.06 | -0.04 | 0.07 | 1.52 | 2.22 | 0.79 |
| **Avg** | **-0.11** | **0.07** | **-0.03** | **0.09** | **1.23** | **2.42** | **0.60** |
| *Endospore Free Assay* | | | | | | | |
| 11 | -0.21 | 0.06 | -0.11 | 0.07 | 2.69 | 2.84 | 1.09 |
| Duplicate | -0.27 | 0.06 | -0.10 | 0.07 | 2.41 | 2.51 | 1.11 |
| 20 | -0.22 | 0.09 | -0.11 | 0.11 | 3.15 | 3.49 | 1.04 |
| 25 | -0.27 | 0.05 | -0.08 | 0.08 | 3.44 | 3.21 | 1.24 |
| Duplicate | -0.27 | 0.06 | -0.15 | 0.07 | 3.30 | 3.28 | 1.16 |
| 32 | -0.27 | 0.05 | -0.10 | 0.07 | 3.43 | 3.23 | 1.23 |
| 43 | -0.30 | 0.05 | -0.13 | 0.07 | 5.04 | 5.23 | 1.11 |
| Replicate | -0.27 | 0.06 | -0.13 | 0.07 | | | |
| Duplicate | -0.26 | 0.05 | -0.09 | 0.07 | 4.47 | 4.49 | 1.15 |
| **Avg** | **-0.26** | **0.06** | **-0.11** | **0.04** | **3.49** | **3.54** | **1.14** |
| *Forsterite Mineral* | -0.23 | 0.06 | -0.12 | 0.05 | | | |
| Duplicate | -0.23 | 0.06 | -0.12 | 0.05 | | | |
| Duplicate | -0.26 | 0.06 | -0.14 | 0.05 | | | |
| **Avg** | **-0.24** | **0.03** | **-0.13** | **0.02** | | | |

**Table 1:** Mg and Si concentrations and Mg isotope compositions of the assay solutions and initial forsterite powder. 2SD for each samples is two times the standard deviation of the population of n (n > 12) repeat measurements of the standards during an analytical session. 2SD for the average of each assays is two times the standard deviation of the sample population.

In the biotic indirect (or dialysis) assays, any changes in dissolution behavior associated with the endospores can be attributed to the adsorption of dissolved Mg onto the endospore surfaces (Harrold and Gorman-Lewis, 2013), decreasing the chemical activity of Mg in the bulk solution (Harrold, 2014). While forsterite dissolution is expected to always be far from equilibrium at these temperature and pressure conditions (Olsen and Rimstidt, 2008; White and Brantley, 1995), it is possible that the preferential leaching of Mg from the crystal lattice could result in a Si-rich layer that can polymerize at the experimental pH of 7.5 (Pokrovsky and Schott, 2000a, 2000b). Magnesium dissolution products may be required to diffuse through this layer, and the rate of diffusion would be dependent upon the Mg activity of the bulk solution (Pokrovsky and Schott, 2000a, 2000b). Therefore, Mg adsorption onto the endospores would increase the rate of forsterite dissolution. An increased adsorption rate was initially observed; however, the rates had returned to the abiotic level (-11.40 ± 0.09 $molg^{-1}s^{-1}$, 2SD) prior to the period for which samples were tested for Mg isotope (10-43 days) (Harrold, 2014). Magnesium is also highly depleted relative to Si in the dissolution products over the entire incubation period due to Mg adsorption onto the endospore surfaces, with an average Mg:Si ratio of approximately 0.60 ± 0.28 (2SD, Harrold, 2014; Fig. 1).

In the biotic homogenous (or free) assays, the endospores can adhere directly to the mineral surfaces in addition to interacting with the aqueous dissolution products. Endospore adhesion onto the mineral surfaces occurs via the complexation of anionic oxygen moieties on the endospore surface with Mg on the mineral surface (Harrold, 2014). This complexation shifts the electron density from the oxygen in the Si-O-Mg forsterite structure to the Mg-ligand bond, making the breaking of the bridging O bond more thermodynamically favorable (Olsen and Rimstidt, 2008). Again, the dissolution rate did initially increase, but returned to approx. abiotic levels (-10.97 ± 0.37, 2SD) prior to the period for which Mg isotopes were analyzed (Harrold, 2014). Magnesium is also depleted relative to Si in the dissolution products over the entire incubation period, but less depleted than in the dialysis assays, with an average Mg:Si ratio of approximately 1.14 ± 0.12 (2SD), again due to Mg adsorption onto the endospore surfaces (Harrold, 2014; Fig. 1). It is possible that the direct forsterite-endospore interaction in the homogenous endospore assays may also release excess Si into solution compared to the abiotic assays (Harrold, 2014).

### *2.4. Chemical Analyses*

In Harrold, (2014), magnesium and iron concentrations were measured on an inductively coupled plasma optical emission spectrometer (ICP-OES). Silicon concentrations were measured using the molybdenum blue colorimetric method, which quantifies the concentrations of aqueous monomeric and dimeric silicic acid. Cation and silica concentrations generated during the biotic and abiotic forsterite dissolution assays are characterized and discussed in detail in Harrold (2014).

### *2.5. Magnesium Isotope Analyses*

Magnesium isotope analyses were performed at the Isotope Laboratory in the Department of Earth and Space Sciences at the University of Washington. All procedures are similar to those discussed in previous papers (Li et al., 2010; Teng et al., 2007, 2010a; Teng and Yang, 2014; Yang et al., 2009).

Filtered samples were transferred to Savillex screw-top Teflon beakers and dried. To ensure complete dissolution, the dried samples were subjected to a 6:1 HF-$HNO_3$ acid digestion followed by a 3:1 HCl-$HNO_3$ acid digestion. The samples were kept in each acid at approx.

125°C for several days. To achieve cation separation, the samples were passed twice through a column containing 1.8 ml Bio-Rad 200-400 mesh AG50W-X8 cation exchange resin in a 1N $HNO_3$ media, and were eluted using 1N $HNO_3$. The collected aliquot contains >99% of the Mg in the sample to prevent isotope fractionation within the column, and limits the concentrations of other elements to less than 5% of the concentration of Mg.

Magnesium isotope compositions were analyzed using the sample-standard bracketing method on a Nu Plasma II MC-ICP-MS. Mg isotope data is expressed in standard δ-notation:

$$\delta^{x}Mg\ (‰) = \left[\frac{\left(\frac{^{x}Mg}{^{24}Mg}\right)_{Sample}}{\left(\frac{^{x}Mg}{^{24}Mg}\right)_{Standard}} - 1\right] * 1000$$

where x refers to masses 25 or 26. The reference materials Seawater (n = 8) and San Carlos Olivine (n = 10) were analyzed at least once during each analytical session, each time yielding a $\delta^{26}$Mg value of -0.83 ± 0.07‰ and -0.25 ± 0.07‰ (Table 2). These values agree with previously published data (Foster et al., 2010; Hu et al., 2016; Ling et al., 2011; Teng et al., 2015).

### *2.6 Saturation State Modeling*

Saturation indices were modeled using the PHREEQC geochemical modeling software. $K_{sp}$ at 298 K and 1 atm and relevant equilibrium phases were obtained from the phreeqc.dat database. Solution conditions were 25 mM NaCl ionic strength, a pH of 7.5, and a temperature of 298 K.

| Sample | $\delta^{26}$Mg (‰) | 2SD | $\delta^{25}$Mg (‰) | 2SD |
|---|---|---|---|---|
| *San Carlos Olivine* | -0.29 | 0.06 | -0.09 | 0.07 |
| Duplicate | -0.23 | 0.09 | -0.11 | 0.11 |
| Replicate | -0.25 | 0.09 | -0.13 | 0.11 |
| Replicate | -0.22 | 0.09 | -0.08 | 0.11 |
| Replicate | -0.28 | 0.09 | -0.13 | 0.11 |
| Duplicate | -0.27 | 0.05 | -0.15 | 0.08 |
| Replicate | -0.26 | 0.07 | -0.12 | 0.06 |
| Replicate | -0.26 | 0.07 | -0.16 | 0.06 |
| Replicate | -0.27 | 0.07 | -0.14 | 0.06 |
| Replicate | -0.30 | 0.05 | -0.16 | 0.07 |
| *Seawater* | -0.85 | 0.06 | -0.43 | 0.07 |
| Replicate | -0.88 | 0.06 | -0.44 | 0.07 |
| Duplicate | -0.83 | 0.09 | -0.41 | 0.11 |
| Duplicate | -0.88 | 0.05 | -0.49 | 0.08 |
| Duplicate | -0.88 | 0.07 | -0.46 | 0.06 |
| Replicate | -0.84 | 0.07 | -0.41 | 0.06 |
| Replicate | -0.88 | 0.07 | -0.41 | 0.06 |
| Replicate | -0.88 | 0.05 | -0.46 | 0.07 |

**Table 2:** Mg isotope composition of reference materials. 2SD = Two standard deviation of the population of n (n > 12) repeat measurements of the standards during an analytical session.

## 3. Results

The Mg isotope composition of the samples overall ranged from $\delta^{26}$Mg = -0.39 ± 0.06 ‰ to -0.08 ± 0.07 ‰. The Mg isotope composition of each of the four assays remained approximately constant within experimental error over the duration of the incubation period (10-43 days). The homogenous abiotic control assay ranged from $\delta^{26}$Mg = -0.39 ± 0.06 ‰ to -0.28 ± 0.06 ‰ with an average Mg isotope composition of $\delta^{26}$Mg = -0.35 ± 0.08 ‰, while the abiotic dialysis assay ranged from $\delta^{26}$Mg = -0.35 ± 0.05 ‰ to -0.26 ± 0.09 ‰ with an average Mg isotope composition of $\delta^{26}$Mg = -0.31 ± 0.09 ‰ (Fig. 2). There is no statistically significant difference in Mg isotope composition between the abiotic free and dialysis assays (two-tailed t-test, p = 0.5360), and therefore, the two assays will be discussed together. The biotic homogenous assay ranged from $\delta^{26}$Mg = -0.30 ± 0.05 ‰ to -0.21 ± 0.06 ‰ with an average Mg isotope composition of $\delta^{26}$Mg = -0.26 ± 0.06‰, and the biotic dialysis assay ranged from $\delta^{26}$Mg = -0.17 ± 0.06 ‰ to -0.08 ± 0.07 ‰ with an average Mg isotope composition of $\delta^{26}$Mg = -0.11 ± 0.07 ‰ (Fig. 2). These two biotic assays are statistically distinct from each other (p = 0.0012) and from the abiotic assays (p = 0.0455 and 0.0005 for the free and dialysis assays, respectively). All sample data is reported in Table 1, and all reference material data is reported in Table 2.

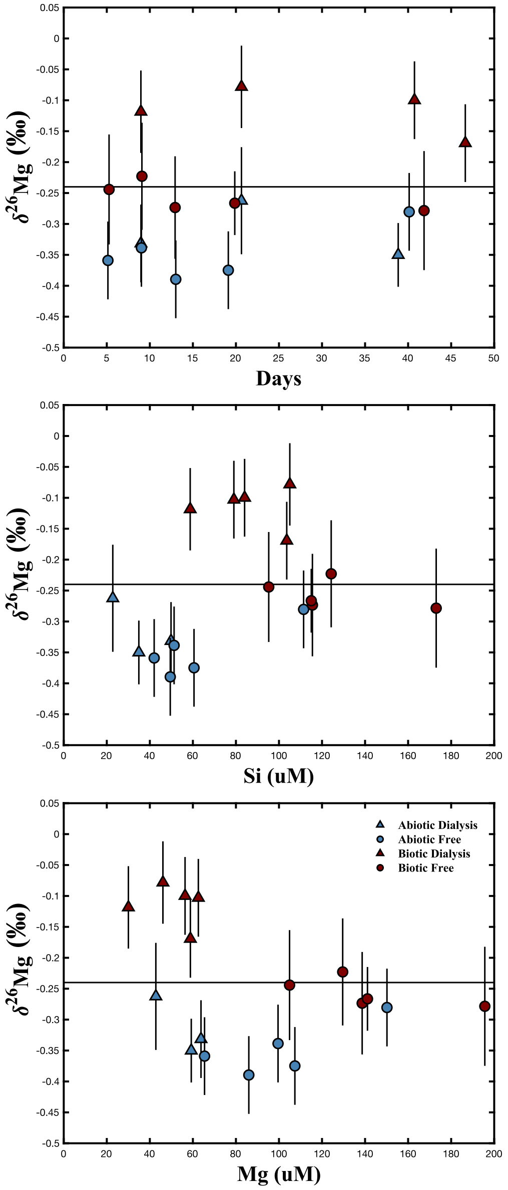

**Figure 2:** Mg isotope composition (a) over the duration of the incubation period, (b) as a function of aqueous Si concentration (μM), and (c) as a function of aqueous Mg concentration (μM). Error bars represent the 2SD for each sample. The triangles represent the dialysis assays and the circles represent the homogenous assays, while the red and blue symbols represent the biotic and abiotic assays, respectively. The solid line represents the Mg isotope composition of the pristine forsterite. Mg and Si concentration data are from Harrold (2014). Data are reported in Table 1.

## 4. Discussion

In this section, we first describe the Mg isotope fractionation associated with forsterite dissolution. We then examine the fractionation of aqueous Mg during secondary mineral precipitation and adsorption onto the endospore surfaces. Finally, we discuss the implications of these findings for our understanding of chemical weathering and the future of Mg isotope research.

### *4.1 Mg isotope fractionation during forsterite dissolution*

Forsterite dissolution resulted in the preferential release of $^{24}$Mg into solution for both biotic and abiotic assays. Because additional processes, such as adsorption and/or secondary mineral precipitation, are involved in producing the measured aqueous Mg isotope composition, the effects of these processes must be excluded prior to determining the composition of the dissolution products. Congruent forsterite dissolution will produce aqueous Mg:Si molar ratios reflecting the original mineral composition (~1.8:1), and any change in that Mg:Si ratio is likely due to additional processes. The percent of dissolved Mg that was removed from solution due to adsorption and/or precipitation can be estimated by comparing the measured aqueous Mg concentration to the Mg concentration calculated based on measured aqueous Si concentration and assuming a Mg:Si ratio of 1.8.

$$\%\, Mg\ Removed = \left(1 - \frac{\mu M\ Mg_{Measured}}{1.8 * \mu M\ Si_{Measured}}\right) * 100$$

It is assumed that no Si is lost due to precipitation or adsorption. A few abiotic samples exhibit minimal (<15%) Mg removal from solution based on this calculation. The Mg isotope composition of these samples ranges from $\delta^{26}$Mg = -0.39 ± 0.06 to -0.35 ± 0.05 ‰, isotopically lighter than the initial mineral powder ($\delta^{26}$Mg = -0.24 ± 0.03 ‰) (Table 1; Fig. 3). The Mg isotope fractionation due exclusively to dissolution in the other samples (with >15% aqueous Mg removal) can be estimated and compared to these measured values. The Mg isotope composition across the four assays varies approx. linearly with Mg:Si (mol/mol) and % Mg removed (Fig. 3). We can therefore perform a linear regression and calculate the Mg isotope composition of the dissolution products in the biotic and abiotic assays at 0% aqueous Mg removed (Fig. 4). The calculated aqueous Mg isotope composition of the dissolution products in the biotic assays is -0.41‰, comparable to the pristine abiotic assays (average $\delta^{26}$Mg = -0.37 ± 0.02 ‰) and the measured isotope composition of samples at <15% Mg removal (average $\delta^{26}$Mg = -0.37 ± 0.03 ‰) (Fig. 3). Based on the similarity between the dissolution product compositions of the biotic and abiotic assays, we conclude that biological processes, such as direct cell surface-mineral

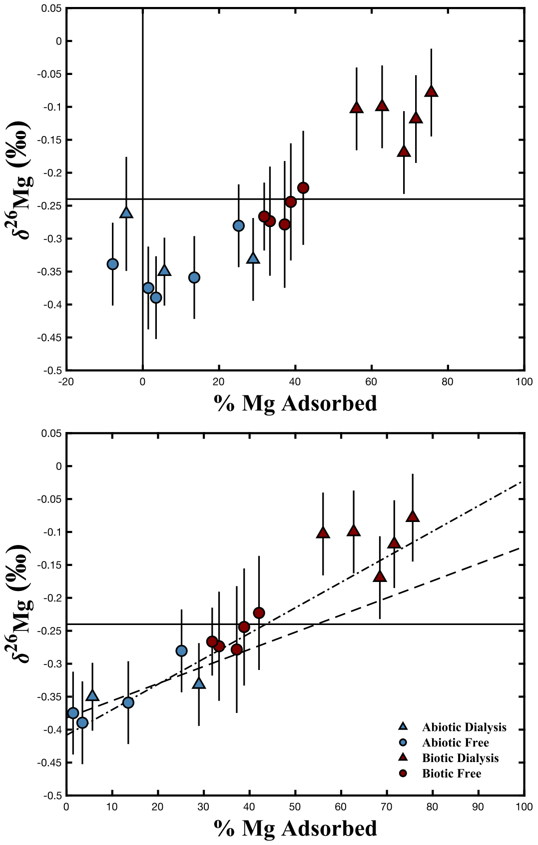

**Figure 3:** (a) Mg isotope composition as a function of Mg:Si molar ratio. The solid lines represent the Mg isotope composition and Mg:Si ratio of the pristine forsterite. (b) Mg isotope composition as a function of % Mg removed from solution due to adsorption. The solid line represents the Mg isotope composition of the pristine forsterite. The dashed and dashed-dotted lines represent linear regressions of the abiotic and biotic data, respectively. The triangles represent the dialysis assays and the circles represent the homogenous assays, while the red and blue symbols represent the biotic and abiotic assays, respectively. Mg and Si concentration data are from Harrold (2014). Data are reported in Table 1.

adhesion, did not have a resolvable effect on Mg isotope fractionation during dissolution. In both biotic and abiotic assays, forsterite dissolution resulted in the preferential release of $^{24}$Mg into solution.

The partial dissolution of Mg-bearing minerals during chemical weathering is known to produce an isotopically light aqueous phase at conditions far from equilibrium, as exhibited in these dissolution experiments. This fractionation occurs because $^{24}$Mg forms slightly weaker bonds than $^{26}$Mg within the crystal structure of a mineral, so $^{24}$Mg is more readily leached during dissolution (Li et al., 2010, 2014; Liu et al., 2014; Pogge von Strandmann et al., 2012; Teng et al. 2010b; Wimpenny et al., 2010). The aqueous Mg and Si concentrations continued to increase at a steady rate throughout the incubation period in these assays, indicating that the system did not approach equilibrium, as expected at these experimental conditions (Harrold, 2014; Fig. 1). Magnesium isotope composition also did not vary systematically with time or with aqueous Mg or Si concentration (Fig. 2). These results confirm that forsterite dissolution rapidly (<10 days) produces an isotopically light aqueous phase compared to the initial mineral composition, but the progressive effects of dissolution do not exert a strong influence on the Mg isotope composition of the dissolution products for the remaining length of the incubation period (10-43 days).

Two abiotic samples exhibit Mg:Si ratios above 1.8 as well as relatively heavy Mg isotope compositions at $\delta^{26}$Mg = -0.26 ± 0.09 and -0.34 ± 0.06 ‰ (Fig. 3a). We attribute this anomaly to a combination of two processes: complete dissolution of forsterite fines and Si adsorption onto secondary Fe-oxide mineral surfaces. Given the observed variety of Fo powder surface area observed in Harrold (2014), some samples are likely to have a higher fraction of fines than others. If these fines are completely dissolved during the assay, mass balance dictates that the Mg isotope composition of their dissolution products will reflect the original mineral composition ($\delta^{26}$Mg = -0.24 ± 0.03‰) and will therefore be isotopically heavy compared to the dissolution products of partially dissolved larger grains. If even small amounts of Si are also adsorbed onto secondary precipitates, then the dissolution products of these fines will be isotopically heavy and have Mg:Si ratios above 1.8 like the observed samples (Fig. 3a). Given these results, we exclude these two samples from further consideration in this discussion.

### *4.2 Effects of secondary mineral precipitation*

Some secondary mineral precipitation likely occurs across the measured incubation period. The expected precipitates are primarily Fe-oxides, particularly hematite, and these minerals are known to adsorb silicic acid at the circumneutral pH conditions present in these experiments (Fein et al., 2002). This adsorption will decrease aqueous Si and alter the steady state of the dissolution system (Harrold, 2014). Because of this aqueous Si sink, the observed decrease in Mg:Si ratios due to endospore surface adsorption of Mg may underestimate the amount of Mg adsorbed. In addition, the mineral precipitates may adsorb aqueous Mg in addition to the endospores.

However, secondary mineral precipitation does not exert a strong control on aqueous Mg isotope composition in these dissolution experiments. The solutions are supersaturated for some Fe-oxide minerals throughout the incubation period, and therefore some precipitation is expected to have occurred (Fig. 4). However, Mg isotope composition is not correlated with the saturation index of these minerals in any of the four assays (Fig. 4). In the biotic assays, the observed Mg isotope fractionation can be primarily attributed to the influence of the endospores as discussed below. A small fractionation effect, likely due to precipitation, is observed in the abiotic assays. Compared to the expected composition of the dissolution products, two abiotic samples exhibit slightly increased Mg isotope compositions ($\delta^{26}$Mg = -0.33 and -0.28 ± 0.06 ‰) and decreased Mg:Si ratios (Mg:Si = 1.29 and 1.35, respectively). These two samples also have the highest saturation indices for various Fe-oxide minerals, such as hematite, from among the abiotic assays (Figs. 3, 4). We therefore conclude that Mg adsorption onto these Fe-oxides preferentially removes $^{24}$Mg from solution, increasing the aqueous Mg isotope composition, although the effect is negligible and likely overshadowed by endospore adsorption in the biotic assays.

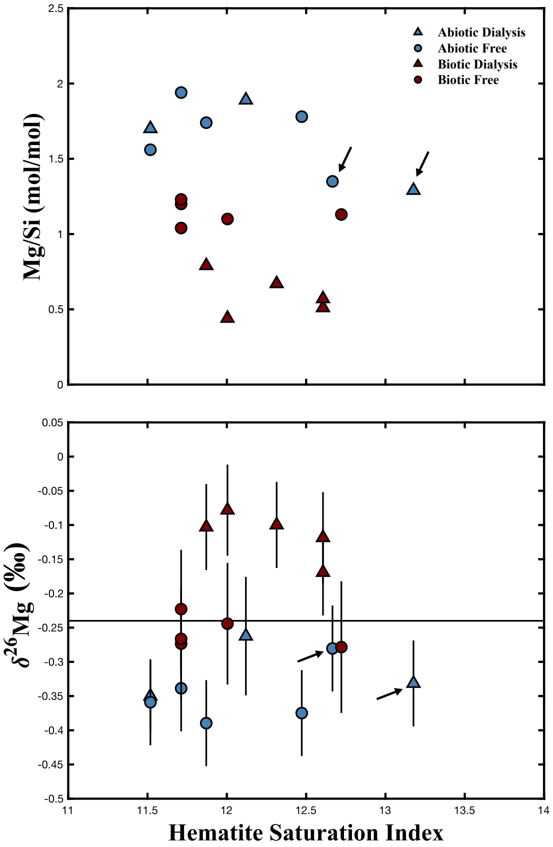

**Figure 4:** (a) Mg/Si (mol/mol) ratio and (b) Mg isotope composition as a function of the saturation index (SI) of hematite, a representative Fe-oxide mineral phase. The two abiotic samples exhibiting the apparent effects of precipitation are identified with arrows. The solid line represents the Mg isotope composition of the pristine forsterite. The triangles represent the dialysis assays and the circles represent the homogenous assays, while the red and blue symbols represent the biotic and abiotic assays, respectively. Mg and Si concentration data are from Harrold (2014). Data are reported in Table 1.

### *4.3 Mg isotope fractionation during endospore surface adsorption*

Surface adsorption has been shown to have a variable impact on Mg isotopes. Studies using natural samples (Brewer et al., 2018; Ma et al., 2015; Opfergelt et al., 2012, 2014) and laboratory experiments (Wimpenny et al., 2014) have found that materials containing high fractions of adsorbed Mg, such as kaolinite, preferentially retain $^{24}$Mg. However, other studies have concluded that adsorbed Mg, on gibbsite for example, is isotopically heavy (Huang et al., 2012; Liu et al., 2014; Pogge von Strandmann et al., 2012). To date, Mg isotope fractionation associated with adsorption onto biological surfaces has not been assessed. This study is therefore a major step towards quantifying the contribution of microbial processes to the Mg cycle and Mg isotope fractionation.

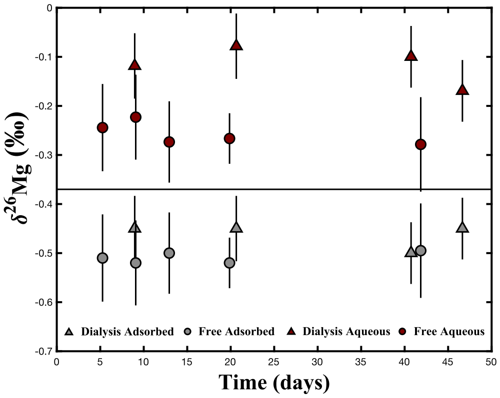

**Figure 5:** Calculated isotope composition of the Mg adsorbed onto the endospore surfaces (grey symbols) compared to aqueous Mg (red symbols) over time. The triangles represent the dialysis assays and the circles represent the homogenous assays. Mg and Si concentration data are from Harrold (2014). The solid line represents the Mg isotope composition of the forsterite dissolution products ($\delta^{26}$Mg = -0.37‰) based on the abiotic dissolution assays.

*B. subtilis* endospore surfaces preferentially adsorb aqueous $^{24}$Mg, much like some mineral surfaces (Brewer et al., 2018; Ma et al., 2015; Opfergelt et al., 2012, 2014; Wimpenny et al., 2014). In the biotic dialysis assays, the endospores are separated from the forsterite powder by dialysis tubing and cannot interact with the minerals directly. However, the endospores do adsorb the Mg dissolution products, as evidenced by the decreased Mg:Si ratios in the biotic assays (Fig. 1). The endospore dialysis assay has a significantly decreased Mg:Si ratio at 0.60 ± 0.14 (SD), compared to the initial forsterite mineral at ~1.8, and a correspondingly heavy average aqueous Mg isotope composition at -0.11 ± 0.07 ‰. It is known that silicon exhibits little adsorption onto endospore surfaces (Harrold, 2014), and the effects of secondary mineral precipitation on Mg are thought to be minimal as discussed in the previous section. Therefore, we attribute the decreased Mg:Si ratio and increased Mg isotope composition to Mg adsorption onto the endospore surfaces in the biotic dialysis assay.

The biotic homogenous assays also have elevated Mg isotope compositions and decreased Mg:Si ratios due to Mg adsorption onto the endospores, although to a lesser degree than the biotic dialysis assays. The average Mg:Si ratio is 1.14 ± 0.08 (SD), which is lower than the ratio expected during congruent dissolution (~1.8), indicating that some aqueous Mg is adsorbed, but a lower fraction than in the dialysis endospore assay (average Mg:Si = 0.60 ± 0.14, SD). The endospores in both assays have approx. the same Mg adsorption capacity (0.51 ± 0.14 and 0.40 ± 0.11 mg in the dialysis and free assays, respectively); however the free assay has a higher concentration of dissolution products than the dialysis assay. The free assay reached Si concentrations ~2-fold higher than the dialysis assay (Table 1), and, assuming congruent dissolution, total Mg dissolved will be ~2-fold higher as well. Because the aqueous Mg concentration is higher in the free assays, the endospores, which have a finite adsorption capacity, are capable of adsorbing a smaller percentage of the dissolved Mg (~37%) compared to the dialysis assay (~67%). The relatively low degree of Mg adsorption in the free assay also produces an intermediate aqueous Mg isotope composition (avg. $\delta^{26}$Mg = -0.26 ± 0.06 ‰) that is higher than the pristine abiotic assays (avg. $\delta^{26}$Mg = -0.37 ± 0.02 ‰) but lower than the dialysis endospore assay (avg. $\delta^{26}$Mg = -0.11 ± 0.07 ‰) (Table 1, Fig. 3).

The adsorption of aqueous Mg onto the endospore surfaces is the primary mechanism by which endospores fractionate Mg isotopes. As forsterite dissolves, $^{24}$Mg is more readily leached into solution, resulting in light aqueous Mg isotope compositions but aqueous Mg:Si ratios that are the same as the dissolving mineral (Fig. 3). Due to endospore adsorption, aqueous Mg:Si ratios decrease and Mg isotope ratios increase relative to the abiotic fluid composition with no effects from adsorption (Figs. 3, 5). The Mg isotope composition across the biotic assays is negatively correlated with Mg:Si ratio and positively correlated with the % of Mg adsorbed

(Figs. 3, 5), which demonstrates that $^{24}$Mg is preferentially adsorbed onto the endospore surfaces, leaving the solution relatively enriched in $^{26}$Mg. A basic mass balance calculation allows us to estimate the isotope composition of the Mg adsorbed on the endospore surfaces (Fig. 5). Assuming a Mg isotope composition of -0.37‰ for the forsterite dissolution products based on the abiotic dissolution assays, the average isotope composition of the adsorbed Mg was -0.48‰ and -0.51‰ for the dialysis and free assays, respectively. The calculated adsorbed composition does not vary with time over the course of the measured incubation period, which, combined with the linear correlation between isotope composition and % Mg adsorbed, indicates that Mg isotope fractionation associated with adsorption is likely an equilibrium process in these assays (Fig. 5).

Because the endospores are metabolically dormant and released minimal organic acids into solution, their impact is limited to these cell surface reactions. The increase in dissolution rate that is associated with the presence of endospores, with and without the dialysis tubing barrier, does not appear to affect the aqueous Mg isotope composition over the analyzed incubation period. However, we cannot rule out any changes in Mg isotope behavior associated with changes in dissolution rate in the first few days of incubation where no Mg isotope data is available. Secondary mineral precipitation appears to play a minimal role in Mg isotope fractionation in the biotic systems. Overall, the endospores affect the Mg isotope systematics of a weathering environment by preferentially adsorbing $^{24}$Mg onto their cell walls.

### *4.4 Implications*

Magnesium is a bioactive element and Mg isotopes can help to elucidate the various biological processes that affect Mg cycling in the environment. Microbes can affect Mg in weathering systems through the production of organic acids, adhesion onto mineral surfaces, uptake and utilization of Mg within the cell, and adsorption onto the cell surface. While previous work has assessed the effects of the biosphere on Mg isotopes in regards to plant uptake (Black et al., 2006, 2008; Bolou-Bi et al., 2010, 2012), biogenic carbonate precipitation (Pogge von Strandmann et al., 2008; Wombacher et al., 2011), and uptake into microbial (Pokharel et al., 2017) and fungal cells (Fahad et al., 2016), this study is the first to examine the Mg isotope fractionation associated with adsorption onto cell surfaces, with endospores here being taken as generally representative of many types of vegetative cells (Borrok and Fein, 2005; Daughney et al., 2001, 2002). These results address cell surface adsorption in isolation as a single facet of the total biological contribution to the Mg cycle. A complete understanding of Mg isotope behavior in the environment requires that the impact of each relevant process be assessed individually. The fluid mobility of Mg in the environment, for example, may be increased by organic acid production, but decreased by adsorption and/or uptake by organisms within the solid substrate, and the relative contribution of each process will likely vary with time and location. A thorough understanding of Mg isotope fractionation during each of these relevant processes would yield important insights into Mg cycling in the environment.

With improvements in our understanding of Mg isotope behavior in weathering environments, including biological effects, Mg isotopes could be used as a biosignature in weathered rocks. This study demonstrates that Mg adsorption onto cell surfaces can retain $^{24}$Mg in the solid phase on immobilized cells, acting counter to purely chemical weathering, which preferentially releases $^{24}$Mg into the hydrosphere. If the effects of various processes involved in weathering, including primary mineral dissolution and alteration, secondary mineral formation, and biological uptake of Mg, can be quantified, it may be possible to parse the individual contribution of each process. A more detailed understanding of the many individual processes involved in rock weathering and their effects on Mg isotopes could permit the use of Mg isotopes as an indicator of biological activity in weathered rocks.

## 5. Conclusions

1. Forsterite dissolution at room temperature and circumneutral pH results in the preferential release of $^{24}$Mg into solution, producing an aqueous Mg isotope composition of $\delta^{26}$Mg = -0.39 to -0.35 ‰, compared to the initial mineral composition of $\delta^{26}$Mg = -0.24 ± 0.03‰.

2. Endospore surfaces preferentially adsorb $^{24}$Mg from solution, resulting in a maximum aqueous Mg isotope composition of $\delta^{26}$Mg = -0.10 ‰ and an average adsorbed Mg isotope composition of $\delta^{26}$Mg = -0.49 ‰.

3. Magnesium adsorption onto the endospore surfaces decreases the Mg:Si ratio of the bulk solution, and therefore aqueous Mg isotope composition is negatively correlated with Mg:Si ratio.

4. A thorough understanding of the Mg isotope fractionation associated with individual biological weathering processes, including cell surface reactivity, will help to elucidate Mg cycling in the environment.

## Acknowledgements

We would like to thank Shui-Jiong Wang and Yan Hu for their assistance throughout this study, Khadijah Karrington Homolka and Jiarui Zhou for their work in the clean lab, and two anonymous reviewers for their careful editing and insightful comments. This work was supported by NSF grant EAR-1340160.

# References

Bennett, P., Rogers, J., Choi, W., Hiebert, F. (2001) Silicates, Silicate Weathering, and Microbial Ecology. Geomicrobiol. J. 18, 3-19.

Black, J.R., Yin, Q.-Z., Casey, W.H. (2006) An experimental study of magnesium-isotope fractionation in chlorophyll-a photosynthesis. Geochim. Cosmochim. Acta 70, 4072-4079.

Black, J.R., Epstein, E., Rains, W.D., Yin, Q.-Z., Casey, W.H. (2008) Magnesium-isotope fractionation during plant growth. Environ. Sci. Technol. 42, 7831-7836.

Bolou-Bi, E.B., Poszwa, A., Leyval, C., Vigier, N. (2010) Experimental determination of magnesium isotope fractionation during higher plant growth. Geochim. Cosmochim. Acta 74, 2523-2537.

Bolou-Bi, E.B., Vigier, N., Poszwa, A., Boudot, J.-P., Dambrine, E. (2012) Effects of biogeochemical processes on magnesium isotope variations in a forested catchment in the Visges Mountains (France). Geochim. Cosmochim. Acta 87, 341-355.

Borrok, D., Fein, J.B., Kulpa, C.F. (2004) Proton and Cd adsorption onto natural bacterial consortia: Testing universal adsorption behavior Geochim. Cosmochim. Acta 68, 3231-3238.

Borrok, D.M., Fein, J.B. (2005) The impact of ionic strength on the adsorption of protons, Pb, Cd, and Sr onto the surfaces of Gram negative bacteria: testing non-electrostatic, diffuse, and triple-layer models. J. Colloid Interface Sci. 286, 110-126.

Brewer, A.B., Teng, F.-Z., Dethier, D. (2018) Magnesium isotope fractionation during granite weathering. Chem. Geo. 501, 95-103.

Daughney, C.J., Fowle, D.A., Fortin, D.E. (2001) The effect of growth phase on proton and metal adsorption by *Bacillus subtilis*. Geochim. Cosmochim. Acta 65, 1025–1035.

Daughney, C.J., Siciliano, S.D., Rencz, A.N., Lean, D., Fortin, D.E. (2002) Hg(II) adsorption by bacteria: A surface complexation model and its application to shallow acidic lakes and wetlands in Kejimkujik National Park, Nova Scotia, Canada. Environ. Sci. Technol. 36, 1546-1553.

Fahad, Z.A., Bolou-Bi, E.B., Kohler, S.J., Finlay, R.D., Mahmood, S. (2016) Fractionation and assimilation of Mg isotopes by fungi is species dependent. Environ. Microbio. Reports 8, 956-965.

Fein, J.B., Boily, J.-F., Yee, N., Gorman-Lewis, D., Turner, B.F. (2005) Potentiometric titrations of *Bacillus subtilis* cells to low pH and a comparison of modeling approaches. Geochim. Cosmochim. Acta 69, 1123-1132.

Fein, J.B., Scott, S., Rivera, N. (2002) The effect of Fe on Si adsorption by *Bacillus subtilis* cell walls: insights into non-metabolic bacterial precipitation of silicate minerals. Chem. Geo. 182, 265-273.

Foster, G.L., Pogge von Strandmann, P.A.E., Rae, J.W.B. (2010) Boron and magnesium isotopic composition of seawater. Geochem, Geophys. Geosys. 11, 1-10.

Friis, A.K., Davis, T.A., Figueira, M.M., Paquette, J., Mucci, A. (2003) Influence of *Bacillus subtilis* cell walls and EDTA on calcite dissolution rates and crystal surface features. Environ. Sci. Technol. 37, 2376-2382.

Gorman-Lewis, D., Fein, J.B., Jensen, M.P. (2006) Enthalpies and entropies of proton and cadmium adsorption onto Bacillus subtilis bacterial cells from calorimetric measurements. Geochim. Cosmochim. Acta 70, 4862-4873.

Harrold, Z.R., (2014) Investigating the effects of *Bacillus subtilis* endospore surface reactivity on low-temperature aqueous geochemical systems. Doctoral dissertation. University of Washington, Seattle, WA, USA.

Harrold, Z.R., Gorman-Lewis, D. (2013) Thermodynamic analysis of *Bacillus subtilis* endospore protonation using isothermal titration calorimetry. Geochim. Cosmochim. Acta 109, 296-305.

Harrold, Z.R., Hertel, M.R., Gorman-Lewis, D. (2011) Optimizing *Bacillus subtilis* spore isolation and quantifying spore harvest purity. J. Microbiol. Methods 87, 325-329.

Hu, Y., Harrington, M.D., Sun, Y., Yang, Z., Konter, J., Teng, F.-Z. (2016) Magnesium isotopic homogeneity of San Carlos olivine: a potential standard for Mg isotopic analysis by multi-collector inductively coupled plasma mass spectrometry. Rapid. Commun. Mass. Sp. 30(19):2123-2132.

Huang, K.-J., Teng, F.-Z., Wei, G.-J., Ma, J-.L., Bao, Z.-Y. (2012) Adsorption- and desorption-controlled magnesium isotope fractionation during extreme weathering of basalt in Hainan Island, China. Earth Planet. Sci. Lett. 359-360, 73-83.

Immenhauser, A., Buhl, D., Richter, D., Niedermayer, A., Reichelmann, D., Dietzel, M., Schulte, U. (2010) Magnesium-isotope fractionation during low-Mg calcite precipitation in a limestone cave – Field study and experiments. Geochim. et. Cosmochim. Acta. 74, 4346-4364.

Kelly, S.D., Boyanov, M.I., Bunker, B.A., Fein, J.B., Fowle, D.A., Yee, N., Kemner, K.M. (2001) XAFS determination of the bacterial cell wall functional groups responsible for complexation of Cd and U as a function of pH. Journal of Synchrotron Radiation 8, 946- 948.

Kelly, S.D., Kemner, K.M., Fein, J.B., Fowle, D.A., Boyanov, M.I., Bunker, B.A., and Yee, N. (2002) X-ray absorption fine structure determination of pH-dependent U-bacterial cell wall interactions. *Geochim. Cosmochim. Acta* **66**, PII S0016-7037(02)00947-X.

Lee, J.-U. and Fein, J.B. (2000) Experimental study of the effects of *Bacillus subtilis* on gibbsite dissolution rates under near-neutral pH and nutrient-poor conditions. Chem. Geo. 166, 193-202.

Li, W., Beard, B.L., Li, C., Johnson, C.M. (2014) Magnesium isotope fractionation between brucite [$Mg(OH)_2$] and Mg aqueous species: Implications for silicate weathering and biogeochemical processes. Earth Planet. Sci. Lett. 394, 82-93.

Li, W.-Y., Teng, F.-Z., Ke, S., Rudnick, R. L., Gao, S., Wu, F.-Y., Chappell B.W. (2010) Heterogeneous magnesium isotopic composition of the upper continental crust. Geochim. Cosmochim. Acta 74, 6867–6884.

Liu, X.-M., Teng, F.-Z., Rudnick, R.R., McDonough, W.F., Cummings, M.L. (2014) Massive magnesium depletion and isotope fractionation in weathered basalts. Geochim. Cosmochim. Acta 135, 336–349.

Ling, M.-X., Sedaghatpour, F., Teng, F.-Z., Hays, P.D., Strauss, J., Sun, W. (2011) Homogeneous magnesium isotopic composition of seawater: an excellent geostandard for Mg isotope analysis. Rapid Commun. Mass Spectrom. 25, 2828-2836.

Ma, L., Teng, F.-Z., Jin, L., Ke, S., Yang, W., Gu, H.-O., Brantley, S.L. (2015) Magnesium isotope fractionation during shale weathering in the Shale Hills Critical Zone Observatory: Accumulation of light Mg isotopes in soils by clay mineral transformation. Chem. Geo. 397, 37-50.

Oelkers, E.H. (2001) An experimental study of forsterite dissolution rates as a function of temperature and aqueous Mg and Si concentrations. Chem. Geo.175, 485-494.

Oelkers, E.H., Benning, L.G., Lutz, S., Mavromatis, V., Pearce, C.R., Plumper, O. (2015) The efficient long-term inhibition of forsterite dissolution by common soul bacteria and fungi at Earth surface conditions. Geochim. Cosmochim. Acta 168, 222–235.

Olsen, A.A., Rimstidt, J.D. (2008) Oxalate-promoted forsterite dissolution at low pH. Geochim. Cosmochim. Acta 72, 1758–1766.

Opfergelt, S., Georg, R.B., Delvaux, B., Cabidoche, Y.-M., Burton, K.W., Halliday, A.N. (2012) Mechanisms of magnesium isotope fractionation in volcanic soil weathering sequences, Guadeloupe. Earth Planet. Sci. Lett. 341-344, 176-185.

Opfergelt, S., Burton, K.W., Georg, R.B., West, A.J., Guicharnaud, R.A. Sigfusson, B., Siebert, C., Gislason, S.R., Halliday, A.N. (2014) Magnesium retention on the soil exchange complex controlling Mg isotope variations in soils, soil solutions and vegetation in volcanic soils, Iceland. Geochim. Cosmochim. Acta 125, 110-130.

Pokrovsky, O.S., Schott, J. (2000a) Forsterite surface composition in aqueous solutions: a combined potentiometric, electrokinetic, and spectroscopic approach. Geochim. Cosmochim. Acta 64, 3299–3312.

Pokrovsky, O.S., Schott, J. (2000b) Kinetics and mechanism of forsterite dissolution at 25Â°C and pH from 1 to 12. Geochim. Cosmochim. Acta 64, 3313-3325.

Pogge von Strandmann, PAE, Burton, KW, James, RH, van Calsteren, P, Gislason, SR, Sigfusson, B. (2008).The influence of weathering processes on riverine magnesium isotopes in a basaltic terrain. Earth Planet Sci Lett 276(1-2):187-197.

Pogge von Strandmann, P.A.E., Opfergelt, S., Lai, Y.-J., Sigfusson, B., Gislason, S.R., Burton, K.W. (2012) Lithium, magnesium and silicon isotope behavior accompanying weathering in a basaltic soil and pore water profile in Iceland. Earth Planet. Sci. Lett. 339-340, 11-23.

Pokharel, R., Gerrits, R., Schuessler, J.A., Floor, G.H., Gorbushina, A.A., von Blanckenburg, F. (2017) Mg isotope fractionation during uptake by a rock-inhabiting, model microcolonial fungus *Knufia petricola* at acidic and neutral pH. Environ. Sc. Technol. 51, 9691-9699.

Rogers, J.R., Bennett, P.C. (2004) Mineral stimulation of subsurface microorganisms: release of limiting nutrients from silicates. Chem. Geo. 203, 91-108.

Siala, A., Hill, I.R., Gray, T.R.G. (1974) Populations of Spore-forming Bacteria in an Acid Forest Soil, with Special Reference to *Bacillus subtilis*. J Gen Microbiol 81, 183- 190.

Song, W., Ogawa, N., Oguchi, C.T., Hatta, T., Matsukua, Y. (2006) Effect of *Bacillus subtilis* on granite weathering: A laboratory experiment. Catena 70, 275-281.

Teng, F.-Z. (2017) Magnesium Isotope Geochemistry. Rev. Mineral. Geochem. vol. 82, 219-287.

Teng, F.-Z., Li, W.-Y., Ke, S., Marty, B., Dauphas, N., Huang, S., Wu, F. Y., Pourmand, A. (2010a) Magnesium isotopic composition of the Earth and chondrites. Geochim. Cosmochim. Acta 74, 4150–4166.

Teng, F.-Z., Li, W.-Y., Rudnick, R.L., Gardner, L.R. (2010b) Contrasting lithium and magnesium isotope fractionation during continental weathering. Earth Planet. Sci. Lett. 300, 63-71.

Teng, F.-Z., Li, W.-Y., Ke, S., Yang, W., Liu, S.-A., Sedaghatpour, S., Wang, S.-J., Huang, K.-J., Hu, Y., Ling, M.-X., Xiao, Y., Liu, X.-M., Li, X.-W., Gu, H.-O., Sio, C.K., Wallace, D.A., Su, B.-X., Zhao, L., Chamberlin, J., Harrington, M., Brewer, A. (2015) Magnesium isotopic compositions of international geological reference materials. Geostand. Geoanal. Res. 29, 329-339.

Teng, F.-Z., Wadhwa, M., Helz, R.T. (2007) Investigation of magnesium isotope fractionation during basalt differentiation: Implications for a chondritic composition of the terrestrial mantle. Earth Planet. Sci. Lett. 261, 84–92.

Teng F.-Z., Yang W. (2014) Comparison of factors affecting the accuracy of high-precision magnesium isotope analysis by multi-collector inductively coupled plasma mass spectrometry. Rapid Commun. Mass Spectrom. 28, 19-24.

Tipper, E.T., Gaillardet, J., Louvat, P., Capmas, F., White, F. (2010) Mg isotope constraints on soil pore-fluid chemistry: Evidence from Santa Cruz, California. Geochim. Cosmochim. Acta 74, 3883-3896.

Tipper, E.T., Galy, A., Bickle, M.J. (2008) Calcium and magnesium isotope systematics in rivers draining the Himalaya-Tibetan-Plateau region: Lithological or fractionation control? Geochim. Cosmochim. Acta 72, 1057-1075.

Uhlig, D., Schuessler, J.A., Bouchez, J., Dixon, J.L., von Blanckenburg, F. (2017) Quantifying nutrient uptake as a driven of rock weathering in forest ecosystems by magnesium stable isotopes. Biogeosciences 14, 3111-3128.

Urey H.C. (1952) The Planets: Their Origin and Development. Yale University Press, New Haven, CT. 245 pp.

Vandevivere, P., Welch, S.A., Ullman, W.J., Kirchman, D.L. (1994) Enhanced Dissolution of Silicate Minerals by Bacteria at Near-Neutral pH. Microbial Ecology 27, 241-251.

White, A.F., Brantley, S.L. (1995) Chemical weathering rates of silicate minerals. Mineralogical Society of America, Washington, D.C.

Whitman, W.B., Coleman, D.C., Wiebe, W.J. (1998) Prokaryotes: The unseen majority. Proc. Nat. Acad. Sci. 95, 6578-6583.

Wightman, P.G., Fein, J.B. (2004) The effect of bacterial cell wall adsorption on mineral solubilities. Chem. Geo 212, 247-254.

Wimpenny, J., Colla, C.A., Yin, Q.-Z., Rustad, J.R., Casey, W.H. (2014) Investigating the behavior of Mg isotopes during the formation of clay minerals. Geochim. Cosmochim. Acta 128, 178-194.

Wimpenny, J., Gislason, S.R., James, R.H., Gannoun, A., Pogge von Strandmann, P.A.E., Burton, K.W. (2010) The behavior of Li and Mg isotopes during primary phase dissolution and secondary mineral formation in basalt. Geochim. Cosmochim. Acta 74, 5259-5279.

Wogelius, R.A., Walther, J.V. (1991) Olivine dissolution at 25 deg C: Effects of pH, CO2, and organic acids. Geochim. Cosmochim. Acta 55, 943-954.

Wombacher, F., Eisenhauer, A., Bohm, F., Gussone, N., Regenberg, M., Dullo, W.-Chr., Ruggeberg, A. (2011) Magnesium stable isotope fractionation in marine biogenic calcite and aragonite. Geochim. Et. Cosmochim. Acta. 75, 5797-5818.

Yang, W., Teng, F.-Z., Zhang, H.-F. (2009) Chondritic magnesium isotopic composition of the terrestrial mantle: A case study of peridotite xenoliths from the North China craton. Earth Planet. Sci. Lett. 288, 475–482.

Yang, W., Teng, F.-Z., Zhang, H.-F., Li S.-G. (2012) Magnesium isotopic systematics of continental basalts from the North China craton: Implications for tracing subducted carbonate in the mantle. Chem. Geol. 328, 185-194.

# CHAPTER 3: Magnesium isotope fractionation during granite weathering

This chapter is published as:

*Brewer, A.B., Teng, F.-Z., Dethier, D. (2018) Magnesium isotope fractionation during granite weathering. Chemical Geology 501, 95-103.*

## Abstract

The Mg isotope compositions of weathering profiles developed on granite and granodiorite bedrock have been analyzed to investigate Mg isotope behavior during the weathering of felsic rocks in a continental environment. $\delta^{26}$Mg generally exhibits a small increase from the bedrock values, which range from -0.17 ± 0.06 ‰ to +0.07 ± 0.06 ‰, until the upper two meters in which a decrease is observed, producing near surface values between -0.14 ± 0.06 ‰ and +0.09 ± 0.06 ‰. The small observed increase in isotopic composition below 2 m is likely due to Mg loss to the hydrosphere during biotite weathering and in situ illite production, while the decrease at depths less than 2 m is likely due to illite weathering near the surface, with a possible minor contribution from downslope deposition of less weathered material. One hydrothermally altered profile shows more extreme fractionation, reaching $\delta^{26}$Mg values as heavy as +0.55 ± 0.06 ‰ in the near surface component of the section. The fractionation associated with Mg loss during weathering can be modeled by Rayleigh distillation with fractionation factors between the residual rock and fluid ranging from $\alpha = 1.00001$ to 1.00040. The Mg isotope composition is primarily controlled by the behavior of illite in the weathering profile, as Mg isotope composition is positively correlated with the illite fraction of major Mg-bearing minerals. A thorough understanding of Mg isotope systematics in these complex clay minerals may permit the use of Mg isotopes in paleosols as paleoclimate indicators.

## 1. Introduction

Continental weathering is a major geochemical control on the state of the atmosphere, hydrosphere, and lithosphere. Chemical weathering of silicates, in combination with carbonate precipitation, removes carbon dioxide from the atmosphere, influencing the long-term atmospheric $CO_2$ budget (Urey, 1952). Weathering also breaks down igneous rocks, providing the components for the formation of clays and other sedimentary rocks, while controlling river water composition, which in turn affects seawater composition (Edmond et al., 1979). Finally, the subduction of weathered crustal material may have an impact on the chemical and isotopic composition of the middle and lower crust as well as upwelling magmas (Hofmann, 2003; Planck, 2014).

Weathering profiles are one of the primary ways of investigating continental weathering. These profiles demonstrate the progressive effects of weathering, from the pristine bedrock to the highly weathered regolith. Weathering characteristics, including mineral dissolution, the formation of secondary minerals, changes in elemental concentrations, and isotope fractionation effects, vary significantly based on bedrock composition and environmental variables such as temperature, pH, precipitation, and atmospheric composition. The chemical and geological variations across a weathering profile can be exploited to elucidate these weathering processes.

Magnesium is both water-soluble and ubiquitous, and can be found in significant concentrations in the hydrosphere, biosphere, and lithosphere. Magnesium has three stable isotopes ($^{24}Mg$, $^{25}Mg$, and $^{26}Mg$), and the 8% mass difference between $^{24}Mg$ and $^{26}Mg$ permits observable mass dependent fractionation, particularly during processes associated with low-temperature water-rock interactions (Teng, 2017 and references therein). Granitoids have been shown to exhibit a wide range of Mg isotopic compositions from -0.404 to +0.441 ‰, likely due to the addition of weathered crustal materials into the magma source (Shen et al., 2009; Li et al., 2010; Liu et al., 2010). The removal of Mg from igneous rocks during chemical weathering has been shown to produce an isotopically heavy residue, as heavy as +1.81 ‰ (Liu et al., 2014). River water is isotopically light, at an average of approximately -1.09 ‰ (Brenot et al., 2008; Huang et al., 2012; Li et al., 2010; Ma et al., 2015; Teng et al., 2010b; Tipper et al., 2006, 2008, 2012; Wimpenny et al., 2010). Individual clay minerals assessed to date exhibit a wide range of compositions, from -1.85 (kaolinite) to +0.18 ‰ (illite), most likely due to the different Mg bonding environments found within the different clays, so clay-rich rocks will also exhibit large compositional variations (Li et al., 2010; Ma et al., 2015; Opfergelt et al., 2014; Wimpenny et al., 2014a). Carbonates, on the other hand, are isotopically light, between -5.54 ‰ and -0.47 ‰ (Higgins and Schrag, 2010; Immenhauser et al., 2010; Pokrovsky et al., 2011). The isotopic composition of loess varies significantly based on its source and transport processes (from -2.04 to +0.25 ‰, Huang et al., 2013; Li et al., 2010; Wimpenny et al., 2014b).

Weathering profiles have previously been analyzed for their Mg isotope compositions, mainly for mafic rocks, such as basalt (Huang et al., 2012; Liu et al., 2014; Pogge von Strandmann et al., 2012) and diabase (Teng et al., 2010b), as well as for shale (Ma et al., 2015). However, granite and granodiorite weathering profiles have not been the subject of systematic study to date. Granite and granodiorite are important components of the continental crust, given that granodiorite is representative of the bulk chemical composition of the upper crust, while granites are the most abundant rock-type in the upper crust (Rudnick and Gao, 2003; Wedepohl, 1995). Therefore, an understanding of granite and granodiorite weathering is crucial to an understanding of weathering on the continents, and Mg isotopes may provide important insights into these weathering environments. This study investigates Mg isotope fractionation during the dissolution and alteration of primary Mg-bearing minerals in felsic rocks, the formation and behavior of secondary clay minerals, and the lateral deposition of aeolian and/or upslope sediment. It represents a first step towards a thorough understanding of Mg isotope systematics in felsic, continental weathering environments.

## 2. Samples

The weathering profiles studied here consist of the Boulder Creek granodiorite (1.65 Ga) and the Silver Plume granite (1.4 Ga) collected around the upland portion of Boulder Creek, Colorado, USA. By 60 Ma, these rocks were uplifted during the Laramide orogeny, coinciding with the removal of their overlying Paleozoic sedimentary rocks (Kelley and Chapin, 2004). Low-grade hydrothermal alteration occurred periodically during the late Mesozoic through the mid-Cenozoic (Dethier and Bove, 2011). Prior to the late Pliocene, down-cutting drainages were responsible for local erosion of these rocks, and glaciers subsequently advanced down the drainage valleys across the region (Thompson, 1991). The modern climate varies with elevation with a mean annual temperature range between 11°C and -4°C and mean annual precipitation between 46 cm and >100 cm (Dethier and Bove, 2011). The late Pleistocene was likely between 8 and 12°C cooler with increased discharge from glaciers (Leonard, 1989).

Three weathering profiles, Magnolia Road, Cave Creek South, and Lee Hill Road, contain 3 to 10 m thick sequences consisting of, in order of increasing depth, regolith (grus or soil), saprolite, oxidized bedrock, and unaltered bedrock (Dethier and Bove, 2011). One additional profile from Hurricane Hill experienced hydrothermal alteration as well as weathering processes, and includes hydrothermally altered regolith, saprolite, and bedrock (Dethier and Bove, 2011). Within the bedrock, plagioclase and biotite are most often altered, and clays including illite, smectite, and kaolinite are commonly present (Dethier and Bove, 2011). Within the saprolites, the alteration sequence is plagioclase > biotite > microcline > quartz, with clay concentrations increasing with degree of weathering (Dethier and Bove, 2011). Soils contain minor aeolian contributions as well as laterally transported upslope material (Dethier and Bove, 2011).

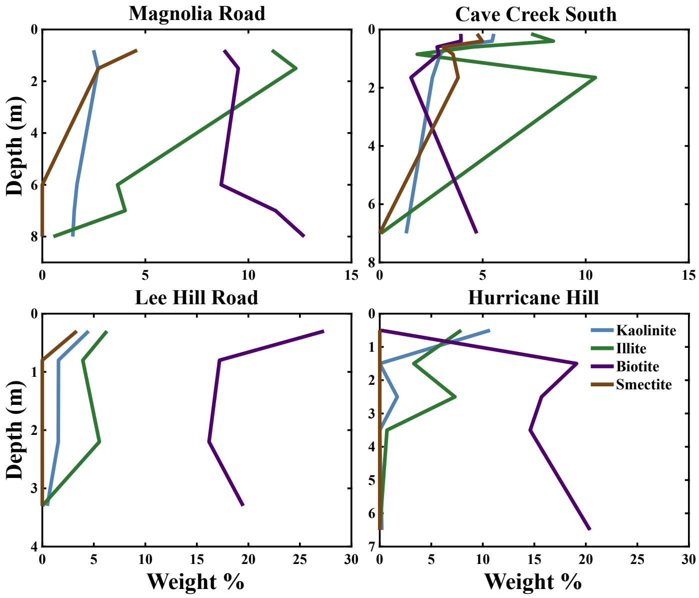

**Figure 1:** Variation of mineral composition (wt%) with depth for each of the four profiles. Note the differences in both x and y-axis scales between the panels. Data are from Dethier and Bove (2011) and are reported in Table 1.

The mineralogy of the samples follows the expected trends in regard to Mg-bearing minerals, with primary biotite generally decreasing with decreasing depth, being replaced by clay minerals, primarily illite, but also kaolinite and smectite in some cases. In the Magnolia Road profile, biotite concentrations decrease 3.89 wt% from the bedrock to the near surface regolith, with a corresponding 4.60 wt% increase in smectite, 10.60 wt% increase in illite, and 1.01 wt% increase in kaolinite (Table 1; Figure 1). The Lee Hill Road profile is slightly more complex, with a 2.29 wt% decrease in biotite from the bedrock to the upper portion of the saprolite, but then a 10.14 wt% increase from the saprolite to the regolith (Figure 1). There is a sharp increase in kaolinite (2.92 wt%), smectite (3.34 wt%), and illite (2.34 wt%) across that saprolite/regolith

| Sample | Biotite | Illite | Smectite | Kaolinite | Chlorite | Calcite | Rock Type |
|---|---|---|---|---|---|---|---|
| *Hurricane Hill* | | | | | | | |
| LC-03-31a | 20.4 | 0.0 | 0.0 | 0.2 | 0.9 | 0.00 | Bedrock |
| LC-03-31b | 14.6 | 0.7 | 0.0 | 0.0 | 0.9 | 0.00 | Oxidized Bedrock |
| LC-03-31c | 15.7 | 7.3 | 0.0 | 1.7 | 1.7 | 0.00 | Oxidized Bedrock |
| LC-03-31d | 19.1 | 3.3 | 0.0 | 0.0 | 0.7 | 0.00 | Oxidized Bedrock |
| LC-03-31f | 0.10 | 7.9 | 0.0 | 10.7 | 0.2 | 0.00 | Regolith (hydrothermal) |
| *Magnolia Road* | | | | | | | |
| LC-03-32a | 12.71 | 0.54 | 0.00 | 1.48 | | 0.29 | Bedrock |
| LC-03-32b | 11.32 | 4.02 | 0.00 | 1.55 | | 0.02 | Oxidized Bedrock |
| LC-03-32c | 8.68 | 3.65 | 0.00 | 1.68 | | 0.00 | Oxidized Bedrock |
| LC-03-32d | 9.51 | 12.30 | 2.73 | 2.70 | | 0.07 | Saprolite |
| LC-03-32e | 8.82 | 11.14 | 4.60 | 2.49 | | 0.09 | Regolith (grus) |
| *Cave Creek South* | | | | | | | |
| LC-04-02 | 4.71 | 0.06 | 0.00 | 1.29 | | 0.00 | Bedrock |
| TC-05-S-01a1 | 1.52 | 10.47 | 3.81 | 2.56 | | 0.00 | Saprolite |
| TC-05-S-01b1 | 2.87 | 1.82 | 3.56 | 2.94 | | 0.00 | Saprolite |
| TC-05-S-01c2 | 2.79 | 4.52 | 3.07 | 3.28 | | 0.00 | Saprolite |
| TC-05-S-01d1 | 3.95 | 8.43 | 4.98 | 5.46 | | 0.00 | Regolith (soil) |
| TC-05-S-01e1 | 3.94 | 7.35 | 4.73 | 5.54 | | 0.00 | Regolith (soil) |
| *Lee Hill Road* | | | | | | | |
| TC-05-S-02a | 19.49 | 0.00 | 0.00 | 0.48 | | 0.20 | Bedrock |
| TC-05-S-02b | 16.18 | 5.54 | 0.00 | 1.55 | | 0.10 | Saprolite |
| TC-05-S-02c | 17.20 | 3.93 | 0.00 | 1.57 | | 0.05 | Saprolite |
| TC-05-S-02d | 27.34 | 6.27 | 3.34 | 4.49 | | 0.05 | Regolith (soil) |
| *Additional Samples* | | | | | | | |
| DC-04-110 | 16.31 | 0.94 | 0.00 | 0.72 | | 0.29 | Bedrock |
| DC-04-116 | | | | | | | Bedrock |
| DC-04-117 | | | | | | | Bedrock |
| DC-05-01 | 11.77 | 0.00 | 0.00 | 0.68 | | 0.00 | Bedrock |

**Table 1:** Mineralogical compositions of weathering profile samples. Quantitative XRD data for Magnolia Road, Cave Creek South, Lee Hill Road, and additional samples from Dethier and Bove (2011). All data are expressed in weight percent.

| Sample | $\delta^{26}$Mg | 2SD | $\delta^{25}$Mg | 2SD | Depth (m) | Rock Type | MgO (wt%) | Mg Norm |
|---|---|---|---|---|---|---|---|---|
| *Hurricane Hill* | | | | | | | | |
| LC-03-31a | -0.07 | 0.06 | -0.05 | 0.07 | 6.50 | Bedrock | 2.44 | 1.00 |
| LC-03-31b | -0.15 | 0.06 | -0.08 | 0.07 | 3.50 | Oxidized Bedrock | 2.05 | 1.03 |
| LC-03-31c | +0.07 | 0.06 | +0.07 | 0.07 | 2.50 | Oxidized Bedrock | 2.00 | 0.77 |
| LC-03-31d | -0.15 | 0.06 | -0.07 | 0.07 | 1.50 | Oxidized Bedrock | 2.39 | 0.97 |
| LC-03-31f | +0.55 | 0.06 | +0.30 | 0.07 | 0.50 | Regolith (hydrothermal) | 0.30 | 0.17 |
| *Magnolia Road* | | | | | | | | |
| LC-03-32a | -0.17 | 0.06 | -0.10 | 0.07 | 8.00 | Bedrock | 1.61 | 1.00 |
| LC-03-32b | -0.12 | 0.06 | -0.06 | 0.07 | 7.00 | Oxidized Bedrock | 2.09 | 1.17 |
| LC-03-32c | -0.10 | 0.06 | -0.08 | 0.07 | 6.00 | Oxidized Bedrock | 1.33 | 1.00 |
| LC-03-32d | 0.00 | 0.06 | +0.04 | 0.07 | 1.50 | Saprolite | 2.33 | 0.91 |
| LC-03-32e | -0.12 | 0.06 | -0.06 | 0.07 | 0.80 | Regolith (grus) | 0.58 | 0.36 |
| *Cave Creek South* | | | | | | | | |
| LC-04-02 | +0.07 | 0.06 | +0.02 | 0.07 | 7.00 | Bedrock | 0.39 | 1.00 |
| TC-05-S-01a1 | +0.24 | 0.06 | +0.15 | 0.07 | 1.65 | Saprolite | 0.34 | 0.74 |
| TC-05-S-01b1 | +0.10 | 0.06 | +0.03 | 0.07 | 0.85 | Saprolite | 0.36 | 0.88 |
| TC-05-S-01c2 | +0.21 | 0.06 | +0.09 | 0.07 | 0.60 | Saprolite | 0.43 | 0.98 |
| TC-05-S-01d1 | +0.14 | 0.06 | +0.07 | 0.07 | 0.40 | Regolith (soil) | 0.52 | 0.90 |
| TC-05-S-01e1 | +0.09 | 0.06 | +0.07 | 0.07 | 0.15 | Regolith (soil) | 0.77 | 0.67 |
| *Lee Hill Road* | | | | | | | | |
| TC-05-S-02a | -0.17 | 0.06 | -0.07 | 0.07 | 3.30 | Bedrock | 2.79 | 1.00 |
| TC-05-S-02b | -0.04 | 0.06 | +0.01 | 0.07 | 2.20 | Saprolite | 3.14 | 1.07 |
| TC-05-S-02c | -0.12 | 0.06 | -0.06 | 0.07 | 0.80 | Saprolite | 3.17 | 1.11 |
| TC-05-S-02d | -0.14 | 0.06 | -0.07 | 0.07 | 0.30 | Regolith (soil) | 3.73 | 1.19 |
| *Additional Samples* | | | | | | | | |
| DC-04-110 | -0.14 | 0.06 | -0.10 | 0.07 | 0.00 | Bedrock | 2.47 | |
| DC-04-116 | -0.26 | 0.06 | -0.10 | 0.07 | 0.00 | Bedrock | 1.86 | |
| DC-04-117 | -0.18 | 0.06 | -0.09 | 0.07 | 0.00 | Bedrock | 3.69 | |
| DC-05-01 | -0.15 | 0.06 | -0.08 | 0.07 | 0.00 | Bedrock | 1.87 | |
| *Reference Materials* | | | | | | | | |
| Basalt BR | -0.33 | 0.06 | -0.20 | 0.07 | | | | |
| Replicate | -0.35 | 0.06 | -0.17 | 0.07 | | | | |
| Replicate | -0.36 | 0.06 | -0.18 | 0.07 | | | | |
| Replicate | -0.36 | 0.06 | -0.22 | 0.07 | | | | |
| Seawater | -0.85 | 0.06 | -0.42 | 0.07 | | | | |
| Duplicate | -0.87 | 0.06 | -0.46 | 0.07 | | | | |

**Table 2:** Magnesium isotope and chemical compositions of weathering profile samples and reference materials. Elemental data from Dethier and Bove (2011). 2SD = Two standard deviation of the population of n (n=22) repeat measurements of the standards during an analytical session. Mg Norm = $[(MgO/TiO_2)_{sample}/(MgO/TiO_2)_{bedrock}]$.

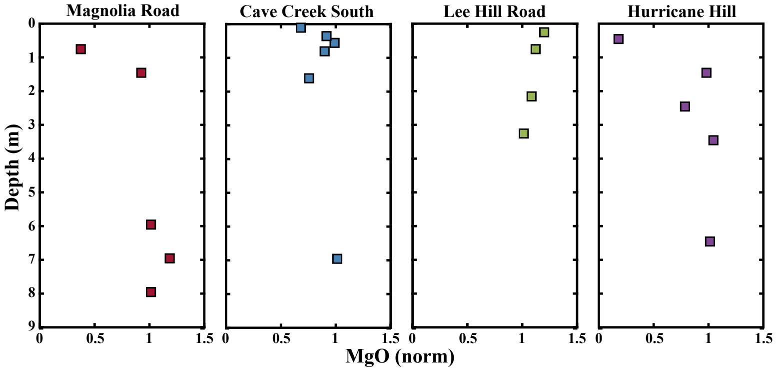

**Figure 2:** Variation of normalized MgO concentration with depth for three weathering profiles (Magnolia Road, Cave Creek South, and Lee Hill Road) and one hydrothermal weathering profile (Hurricane Hill). MgO Norm = $[(MgO/TiO_2)_{sample}/(MgO/TiO_2)_{bedrock}]$. Data are from Dethier and Bove (2011) and are reported in Table 2.

boundary as well (Figure 1). The Cave Creek South profile exhibits a 3.19 wt% decrease in biotite from the bedrock to the saprolite, but then an increase up through the saprolite and regolith; kaolinite increases consistently from 1.29 wt% to 5.54 wt%, but the trends in illite and smectite are more erratic, increasing and decreasing across the profile (Figure 1). Finally, the Hurricane Hill profile contains 20.4 wt% biotite in the unaltered bedrock, which decreases to only 0.1 wt% in the upper regolith, with corresponding increases in kaolinite (0.2 to 10.7 wt%) and illite (0 to 7.9 wt%) (Figure 1).

The Mg concentration of these four profiles also demonstrates the effect of weathering (Figure 2). The Magnolia Road, Cave Creek South, and Hurricane Hill profiles exhibit a decrease in Mg concentration, as expressed in terms of normalized MgO (MgO Norm = $(MgO/TiO_2)_{sample}/(MgO/TiO_2)_{bedrock}$), between the bedrock and the upper ~2 meters of the profile. At Magnolia Road, Cave Creek South, and Hurricane Hill, this decrease is approximately 9%, 26%, and 23% respectively; then in the upper ~2 meters, Mg is depleted again, dropping a further 55%, 7%, and 60%, respectively (Figure 2). The Lee Hill Road profile does not follow this trend, and instead demonstrates a 19% increase in Mg from the bedrock to the near surface regolith, likely due to the deposition of less weathered upslope material (Figure 2). The profiles generally exhibit a decrease in MgO concentration with increasing chemical index of weathering

(CIW = $(Al_2O_3/(Al_2O_3 + CaO + Na_2O))*100$), as is expected given that Mg-bearing minerals are progressively lost during weathering (Figure 3).

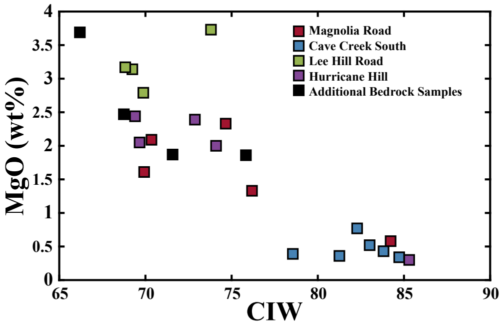

**Figure 3:** Variation of Mg concentration (wt% MgO) with chemical index of weathering (CIW), where CIW = $[Al_2O_3/(Al_2O_3+CaO+Na_2O)]*100$. Data are reported in Table 2.

## 3. Methods

All Mg isotope analyses were performed at the Isotope Laboratory at the University of Washington, and follow the procedures reported in previous studies (Li et al., 2010; Teng et al., 2007, 2010a; Teng and Yang, 2014; Yang et al., 2009).

Powdered samples in Savillex screw-top beakers were dissolved in two stages to ensure complete dissolution. First, concentrated HF and $HNO_3$ were added in a 3:1 ratio, and the samples were heated for at least one week at approximately 125°C, after which the sample was completely dried. Second, concentrated HCl and $HNO_3$ were added in a 3:1 ratio, heated for several days, again at approximately 125°C, and finally dried. To achieve Mg purification, the samples were passed through columns containing Bio-Rad 200-400 mesh AG50W-X8 cation exchange resin, and were eluted using 1N $HNO_3$. This procedure ensures that the collected fraction contains > 99% of the total sample Mg to prevent fractionation within the column, and that the matrix elements were limited to less than 5% of the concentration of Mg to prevent matrix effects (Teng and Yang, 2014).

Magnesium isotope compositions were analyzed using the sample-standard bracketing method on a Nu Plasma II MC-ICP-MS. Mg isotope data is expressed in standard δ-notation:

$$\delta^{x}Mg\ (‰) = \left[\frac{\left(\frac{{}^{x}Mg}{{}^{24}Mg}\right)_{Sample}}{\left(\frac{{}^{x}Mg}{{}^{24}Mg}\right)_{Standard}} - 1\right] * 1000$$

where x refers to masses 25 or 26. The reference materials Seawater (n=2) and Basalt BR (n=4) were analyzed at least once during each analytical session, each time yielding a $\delta^{26}$Mg value of -0.83 ± 0.07‰ and -0.41 ± 0.09‰ (Table 2). These values agree with previously published data (Foster et al., 2010; Ling et al., 2011; Teng et al., 2015).

The mineralogy of the Hurricane Hill samples was analyzed at the Space Science and Astrobiology Division at NASA's Ames Research Center. Bulk samples were crushed and passed through a 250 μm sieve, spiked with 10% $\alpha$-$Al_2O_3$ as an internal standard, and micronized in ethanol using a McCrone Mill. The micronized samples were dried under a heat lamp, saturated with Vertrel® and vortexed with plastic beads to promote random orientation. The samples were then sieved (250 μm) and side-loaded into an XRD mount. All powdered samples were analyzed on a Rigaku Smartlab diffractometer using Cu k-alpha radiation and a scintillation detector with 1° divergence and receiving slits. Samples were scanned from 5° to 65° at 0.02° 2θ steps with a 2 second per step count time. Quantitative mineralogy was calculated using the full pattern peak-fitting program RockJock 11 (Eberl, 2009).

## 4. Results

Magnesium isotope compositions for weathering profile samples and reference materials are reported in Table 2, along with major element data for the rock samples, including those from Dethier and Bove (2011). The mineralogy of the Hurricane Hill samples, together with others from Dethier and Bove (2011), is reported in Table 1.

The Mg isotope composition of the non-hydrothermally altered samples generally increases slightly from the bedrock to the upper ~2 meters of the profile, and then above 2 m decreases again back to near bedrock values. At Magnolia Road, $\delta^{26}$Mg increases from -0.17 ± 0.06 ‰ in the bedrock, to 0.00 ± 0.06 ‰ in the saprolite at 1.5 meters depth, and then decreases to -0.12 ± 0.06 ‰ in the overlying grus. Cave Creek South exhibits an increase in $\delta^{26}$Mg from +0.07 ± 0.06 ‰ in the bedrock to +0.24 ± 0.06 ‰ in the saprolite at 1.65 meters, and then decreases to +0.09± 0.06 ‰ in the uppermost soil sample at 0.15 meters. At Lee Hill Road, the trend continues, moving from a $\delta^{26}$Mg value of -0.17 ± 0.06 ‰ in the bedrock to -0.04 ± 0.06 ‰ in the saprolite at 2.20 meters, and then decreasing to -0.14 ± 0.06 ‰ in the soil at 0.30 meters. The Hurricane Hill hydrothermal sample shows a major increase in one near surface sample (0.5 m), from a bedrock value of -0.07 ± 0.06 ‰ to +0.55 ± 0.06 ‰ at the surface (Figure 4). However, the profiles generally exhibit a small increase in Mg isotope composition with decreasing depth from the bedrock, until the upper 2 meters in which a decrease is observed in the non-hydrothermal profiles (Figure 4). While the bedrock compositions of these samples vary widely, from -0.17 to +0.07 ‰, the effects of weathering within each profile are apparent, and reveal a consistent trend of Mg isotope fractionation.

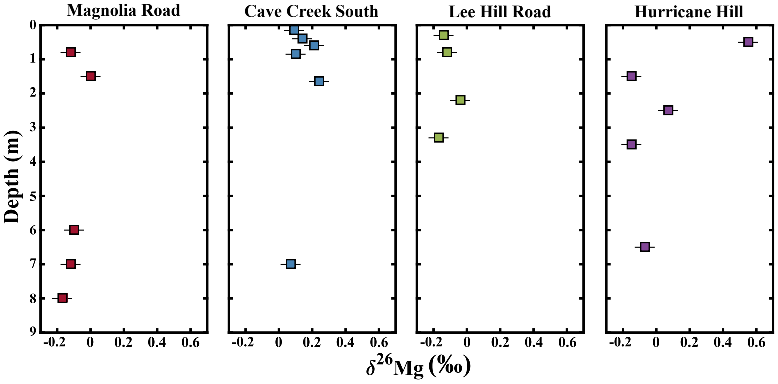

**Figure 4:** $\delta^{26}$Mg variations with depth for the three weathering profiles (Magnolia Road, Cave Creek South, and Lee Hill Road) and one hydrothermal weathering profile (Hurricane Hill). Error bars represent two times the standard deviation (± 0.06 ‰). Data are reported in Table 2.

## 5. Discussion

In this section, we discuss three possible mechanisms for Mg isotope fractionation during granite weathering: lateral deposition, primary mineral alteration and dissolution, and the formation, alteration, and dissolution of secondary minerals. We then compare these granite and granodiorite weathering profiles with other weathering profiles that have been analyzed for Mg isotopes to date. Finally, we discuss the implications of constraining the effects of granite weathering on Mg isotopes for Mg cycling on the continents, the historical shift of continental crust composition, and the reconstruction of paleo-weathering environments.

### *5.1 Lateral Transport*

Aeolian deposition in the upper section of a weathering profile can alter its Mg isotope composition (e.g., Liu et al., 2014). Loess, for example, is known to demonstrate a variety of Mg isotopic compositions, depending on its source material and transport processes (Huang et al., 2013; Li et al., 2010; Wimpenny et al., 2014b). Because carbonate minerals tend to be isotopically light in regard to Mg, loess containing a significant carbonate fraction typically has a low Mg isotope composition, while more silicate-rich loess tends to be heavier (Huang et al., 2013; Li et al., 2010; Liu et al., 2014; Wimpenny et al., 2014b). To produce the observed near-surface decrease in $\delta^{26}$Mg, the deposited material would almost certainly need to contain a significant carbonate fraction. However, the calcite concentration in these profiles never exceeds 0.3 wt% and no other carbonate minerals are observed, so it is unlikely that carbonate could play a role in controlling Mg isotope composition (Table 1). Therefore, while aeolian sediments may be present in the near-surface portion of the profiles, they are unlikely to be responsible for the observed shift towards lighter $\delta^{26}$Mg values, given the low levels of carbonate present throughout the profiles.

The lateral transport of less weathered silicate material from upslope may also play a role in the decrease in Mg isotope composition in the near surface samples (Liu et al., 2014). The Cave Creek South and Lee Hill Road locations exhibit an increase in biotite content in this portion of the sections, most likely indicating the deposition of less-weathered sediment (Figure 1). The addition of relatively pristine material could result in a decrease in $\delta^{26}$Mg, given that rock gradually loses light Mg to the hydrosphere during weathering. However, no systematic increase in Mg concentration is observed, which one would expect if such deposition had occurred (Figure 2). With the current data, it is not possible to quantify the extent of these additions, given that the nature of the source materials and the fraction of the total Mg that they contributed are unknown, but given the absence of increased Mg concentrations, the effect on Mg isotopes is likely minimal.

### *5.2 Primary and secondary mineral behavior*

Previous weathering profile studies focusing on mafic lithologies have found that $^{26}$Mg/$^{24}$Mg ratios generally increase with increased weathering intensity (Huang et al., 2012; Liu et al., 2014; Teng et al., 2010b; Pogge von Strandmann et al., 2012); a trend which is also observed in these more felsic profiles. Magnesium in the unweathered granite and granodiorite bedrock in these profiles is primarily contained in biotite, and the loss of biotite in the rock may affect its Mg isotope composition (Ryu et al., 2011). In these profiles however, very little Mg is removed from the rock until the upper two meters of the profile (Figure 2). The Mg remains within secondary minerals, primarily illite, with minor contributions from oxides and other clays. This transition from primary biotite to secondary minerals results in limited Mg isotope fractionation because nearly all of the Mg is preserved in the rock, retaining the original isotope composition. The small decrease in Mg concentration at depths below two meters is likely responsible for the small increase in Mg isotope composition in those sections, as heavy Mg is preferentially incorporated into secondary clay minerals, while light Mg is lost to the hydrosphere. The weathering of primary minerals, largely biotite, therefore has a small but observable impact on Mg isotopes in these granite and granodiorite weathering environments, imparting a relatively heavy isotopic signature in the residual rock at depths greater than 1.5-2 m.

The Mg isotope composition of these weathering profiles is mainly controlled by the formation and loss of secondary clay minerals. A decrease in the Mg isotope ratios is observed in the upper two meters of each non-hydrothermal profile primarily due to changes in secondary mineral abundance, particularly the illite content. Illite can be produced in situ during weathering or hydrothermal activity as an alteration product of feldspars and micas, and can subsequently be lost due to further weathering (Meunier and Velde, 2004). The Mg in illite, like in biotite, is primarily structural, while Mg in clays such as kaolinite is primarily adsorbed onto surface and interlayer sites (Drever, 1988). Structural sites in clays and similar minerals show a systematic preference for the heavy isotope of Mg, while Mg adsorbed onto clay surfaces is typically isotopically light (Opfergelt et al., 2012, 2014; Wimpenny et al., 2014a). As the illite fraction of total major Mg-bearing minerals (biotite, illite, chlorite, and smectite) increases, so does the Mg isotope composition (Figure 5). However, the upper two meters of the non-hydrothermal profiles show a decrease in Mg isotope composition, and the Magnolia Road and Cave Creek South locations also show a general decrease in illite (Figures 1 and 4). As illite is weathered in the profile, Mg likely shifts from being primarily present in structural sites to being adsorbed onto surface sites in minerals such as kaolinite, resulting in heavy Mg being lost to the hydrosphere and leaving the solid phase enriched in light Mg. The strong positive correlation between $\delta^{26}$Mg and the illite fraction of total major Mg-bearing minerals (biotite, illite, chlorite, and smectite) is likely primarily due to a combination of in situ illite production below 2 m and subsequent loss in the near surface samples (Figure 5).

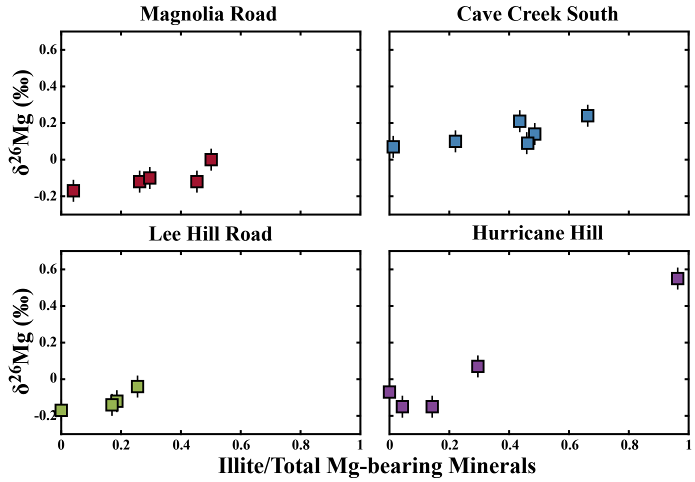

**Figure 5:** $\delta^{26}$Mg variation with illite fraction of Mg-bearing minerals, expressed in terms of weight percent. The Mg-bearing minerals considered here are illite, biotite, smectite, and chlorite (illite fraction = [(wt% illite / (wt% illite + wt% biotite + wt% smectite + wt% chlorite)]. The Mg contribution from other minerals is negligible. Error bars represent two times the standard deviation for $\delta^{26}$Mg (± 0.06 ‰). Data are reported in Tables 1 and 2.

The observed Mg isotope fractionation associated with Mg loss to the hydrosphere can be modeled using Rayleigh fractionation, as also observed in the weathering profiles of other rock types (Teng, 2017). Note that Rayleigh fractionation models provide only a limited approximation of isotope behavior in natural weathering systems. The models assume a constant fractionation factor between the solid and liquid phases during rock leaching. However, a natural weathering system is comprised of many complex chemical interactions, and some of these processes, such as adsorption onto secondary minerals, are not accounted for in the Rayleigh models. The equation governing Rayleigh fractionation is $\delta^{26}Mg_{residual\ rock} = (\delta^{26}Mg_{bedrock}+1000)f^{(1/\alpha - 1)} - 1000$, where f = fraction of bedrock Mg remaining in the weathered sample ($Mg_{residual\ rock}/Mg_{bedrock}$). The apparent fractionation factor (α) values [$\alpha=(^{26}Mg/^{24}Mg)_{residual\ rock}/(^{26}Mg/^{24}Mg)_{fluid}$] vary from 1.00001 to 1.00040 for these samples (Figure 6), similar to the values observed during the weathering of mafic rocks ($1.00005 < \alpha < 1.0004$; Liu et al., 2014). The Hurricane Hill hydrothermal profile samples reflect a higher

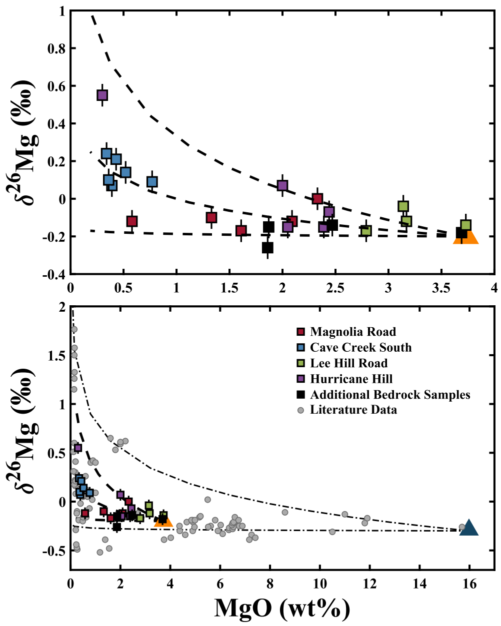

**Figure 6:** Panel (A) shows Mg concentration (wt% MgO) correlated with $\delta^{26}$Mg for all measured samples. Magnolia Road (red squares), Cave Creek South (blue squares), Lee Hill Road (green squares), and Hurricane Hill (purple squares) profiles are included, as well as additional bedrock samples (black squares) from the area. Dashed curves represent Rayleigh distillation models of Mg loss and Mg isotope fractionation for three different values of the fractionation factor α (top: 1.00040, middle: 1.00015, bottom: 1.00001). The orange triangle represents the pristine bedrock used in the Rayleigh distillation models (MgO wt% = 3.73 and $\delta^{26}$Mg = -0.20 ‰). Panel (B) shows the experimental (colored squares) and modeling data (dashed lines) from Panel (A) as well as weathering profile data from other regions and lithologies (grey circles). Literature data from Huang et al., (2012), Liu et al., (2014), Pogge von Strandmann et al., (2012) and Teng et al., (2010b). The dotted lines represent Rayleigh distillation models of Mg removal from pristine bedrock and its effect on Mg isotope composition. For the upper line α = 1.00040, and for the bottom line α = 1.00001. The blue triangle represents the pristine bedrock used in the Rayleigh distillation models (MgO wt% = 16.0 and $\delta^{26}$Mg = -0.25 ‰). Data are reported in Table 2.

fractionation factor, falling near 1.00040, while the Lee Hill Road samples exhibit minimal fractionation with Mg loss and therefore have a low α near 1.00001 (Figure 6). This range of α values is similar to that found in other weathering profiles (Figure 6b). Despite the complications associated with the clay mineralogies in these profiles, they still display behavior broadly typical of Rayleigh fractionation.

### *5.3 Comparison with other weathering profiles*

Compared to the other weathering profiles analyzed for Mg isotopes, primarily with mafic lithologies, these granite and granodiorite profiles exhibit a small degree of fractionation;

however, this difference is unsurprising given the mineralogical and weathering conditions present in each profile. Profiles developed on diabase and basalt bedrock exhibit more extreme fractionation, -0.24 to +1.81 ‰ in one basalt profile, for example (Figure 6b; Liu et al., 2014). The samples in those profiles have experienced much more extreme Mg depletion, often greater than 99%, while the non-hydrothermal granite and granodiorite profiles have only lost up to 64% Mg (Table 2; Huang et al., 2012; Liu et al., 2014; Teng et al., 2010b). The hydrothermal profile lost 83% Mg, which may explain its more dramatic Mg isotope fractionation than the other profiles (Table 2). Given that one of the dominant controls on Mg isotope fractionation in weathering environments is the preferential loss of $^{24}$Mg to the hydrosphere, leaving a rock residue enriched in $^{26}$Mg, it makes sense that more extreme Mg depletion will produce more extreme Mg isotope fractionation. The explanation for the more extreme weathering observed in these other profiles is likely primarily the result of mineralogical differences. The abundant Mg-bearing minerals in the mafic profiles, primarily pyroxene, are more readily weathered than biotite in these felsic profiles, so Mg is more readily lost to the hydrosphere (Ehlers and Blatt 1982). The Mg isotope fractionation in the granite and granodiorite profiles is less dramatic than that previously observed in mafic profiles; however, Mg isotopes remain informative regarding weathering in these lithologies.

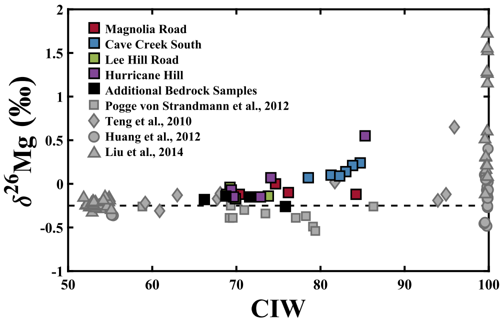

**Figure 7:** $\delta^{26}$Mg correlation with Chemical Index of Weathering, where CIW = $[Al_2O_3/(Al_2O_3+CaO+Na_2O)]*100$. Cation concentrations are expressed in terms of weight percent. Magnolia Road (red squares), Cave Creek South (blue squares), Lee Hill Road (green squares), and Hurricane Hill (purple squares) profiles are included, as well as additional bedrock samples (black squares) from the area. The grey symbols represent literature data from other weathering profiles. The dashed black line expresses the average upper continental crust Mg isotope composition, $\delta^{26}$Mg = -0.22 ‰ (Li et al., 2010). Data are reported in Table 2.

### *5.4 Implications*

Granite and granodiorite weathering processes play a major role in Mg cycling in many continental surface environments and Mg isotopes could help elucidate these processes. In these environments, the sources of Mg in groundwater, soils, and the biosphere may be limited to the weathering of felsic rocks and aeolian deposition. To understand Mg isotope behavior in these regions, it is therefore important to have a clear picture of these weathering processes, and how they affect the isotopic composition of the Mg that is released into near-surface environments. In particular, the ability to differentiate the effects of primary mineral alteration and dissolution, secondary mineral formation, alteration, and dissolution, and lateral transport would permit significant insights into surface processes. The variety of trends observed in these four profiles is evident in the correlation between $\delta^{26}$Mg and the chemical index of weathering (CIW), a measure of weathering and alteration intensity, demonstrating the complexity of Mg isotope behavior in these systems (Figure 7). The Cave Creek South and Hurricane Hill samples show a strong positive correlation, while the Magnolia Road and Lee Hill Road profiles show no variation in $\delta^{26}$Mg with CIW (Figure 7). Magnesium isotopes are clearly sensitive to the specific mechanisms of chemical weathering, sensitive enough to exhibit different behaviors even within profiles from the same locale, and a complete understanding of this Mg isotope behavior could provide valuable insight into these complex weathering systems.

Magnesium isotope behavior during continental weathering may also help explain the role of preferential Mg weathering in the compositional shift of the continental crust from basalt to andesite. During weathering, MgO, $Na_2O$, and CaO are leached from the crustal rock into the hydrosphere, while other components, such as $SiO_2$, $Fe_2O_3$, and $TiO_2$, are more likely to be retained in the rock (Garrels and McKenzie, 1971). $Na_2O$ remains in solution or is precipitated as an evaporite and CaO is precipitated as carbonate, but MgO is primarily fixed in oceanic crust, and ultimately subducted (Holland, 1984; Rudnick, 1995). MgO is thus recycled from the crust back into the mantle, which may have contributed to the transition in the crust from more mafic lithologies to the modern andesitic composition (Rudnick, 1995). The present study demonstrates that, with the exception of the near surface samples, the weathering of granite and granodiorite results in a progressive increase in $\delta^{26}$Mg in the residual rock as MgO is lost to the hydrosphere, which is in agreement with previous studies of the effects of weathering on other lithologies (Huang et al., 2012; Liu et al., 2014; Ma et al., 2015; Pogge von Strandmann et al., 2012; Teng et al., 2010b). The Mg isotope composition of the continental crust varies significantly (-0.52 to +0.92 ‰; Li et al. 2010). If sedimentary and formerly sedimentary material comprises a significant fraction of the crust, the crust overall should evolve towards a heavy Mg isotope composition, which can be tested by systematic studies of crustal compositions through time.

Magnesium isotope fractionation during the weathering of felsic lithologies, particularly the fractionation effects observed during the formation of secondary minerals, may be applied as an indicator of past climate and lithological conditions. The type and composition of clays and other secondary minerals are controlled by the lithology of the rock being weathered and environmental factors, such as pH, temperature, and water availability, so these variables indirectly determine the Mg isotope composition of a profile. For example, the transition from biotite, with primarily structural Mg, to kaolinite, with primarily exchangeable Mg, is associated with a change in Mg isotope composition (Drever, 1988; Opfergelt et al., 2012, 2014; Wimpenny et al., 2014a). In pristine weathering profiles, the clay mineralogy itself could be used a tracer of the weathering environment, but in paleosol profiles that have been heavily altered by metamorphism, the clay composition may not be preserved. However, the Mg isotope composition of a rock is not significantly affected by metamorphism (Geske et al., 2012; Li et al., 2011; Wang et al., 2015), so this isotopic indicator of climate may remain. While this study focuses Mg isotope behavior during the transitions between biotite, illite, and kaolinite, the relationships between other primary and secondary minerals during weathering could be used in a similar way. With a thorough understanding of the relationship between Mg isotopes and clay mineralogy, Mg isotopes in preserved weathering profiles may be used to reconstruct paleo-weathering environments (Huang et al., 2016).

## 6. Conclusions

Based on the Mg isotope analysis of four weathering profiles from granite and granodiorite lithologies from Boulder Creek, Colorado, USA, the following conclusions are drawn:

1. The Mg isotope composition of three non-hydrothermal weathering profiles varies from -0.17 ± 0.06 ‰ to +0.07 ± 0.06 ‰ in the bedrock to -0.14 ± 0.06 ‰ to +0.09 ± 0.06 ‰ near the surface, and -0.07 ± 0.06 ‰ to +0.55 ± 0.06 ‰ in one hydrothermal section.
2. Magnesium isotope fractionation is primarily controlled by the illite content in the rocks, increasing with illite production at depths greater than ~2 m, then decreasing in the near surface samples, most likely from illite weathering with a small contribution from the lateral transport of less weathered material.
3. Magnesium isotope fractionation can be described by Rayleigh distillation with α values from 1.00001 to 1.00040.
4. With additional study, magnesium isotopes may be used as paleoclimate indicators in preserved felsic weathering profiles, even altered profiles, because they are sensitive to clay mineralogy.

## Acknowledgements

We would like to thank Shui-Jiong Wang, Yan Hu, and Lie-Meng Chen for their assistance throughout this study, Khadijah Karrington Homolka for her work in the clean lab, Keith Morrison and Tom Bristow for their help with the XRD analyses, and Kang-Jun Huang and Diana Carlsson for their careful editing and insightful comments. This work was supported by NSF grant EAR-1340160.

## References

Brenot, A., Cloquet, C., Vigier, N., Carignan, J., France-Lanord, C., 2008. Magnesium isotope systematics of the lithologically varied Moselle river basin, France. Geochim. Cosmochim. Acta 72, 5070-5089.

Dethier, D.P., Bove, D.J., 2011. Mineralogical and geochemical changes from alteration of granitic rocks, Boulder Creek Catchment, Colorado. Vadose Zone J. 10, 858-866.

Drever, J.I., 1988. The Geochemistry of Natural Waters. Prentice Hall, New Jersey.

Eberl, D.D., 2009. User's guide to rockjock: A program for determining quantitative mineralogy from powder X-ray diffraction data. U.S. Geological Survey, Open-file report 03-78.

Edmond, J.M., Measures, C., McDuff, R.E., Chan, L.H., Collier, R., Grant, B., Gordon, L.I., Corliss, J.B., 1979. Ridge crest hydrothermal activity and the balances of the major and minor elements in the ocean: The Galapagos data. Earth Planet. Sci. Lett. 46, 1-18.

Ehlers, E.G., Blatt, H., 1982. Petrology: Igneous, Sedimentary, and Metamorphic. W.H. Freeman and Company, California.

Foster, G.L., Pogge von Strandmann, P.A.E., Rae, J.W.B., 2010. Boron and magnesium isotopic composition of seawater. Geochem, Geophys. Geosys. 11, 1-10.

Garrels, R.M., MacKenzie, F.T., 1971. Evolution of sedimentary rocks. Norton, New York.

Geske, A., Zorlu, J., Richter, D.K., Buhl, D., Niedermayr, A., Immenhauser, A., 2012. Impact of diagenesis and low grade metamorphosis on isotope ($\delta^{26}$Mg, $\delta^{13}$C, $\delta^{18}$O and $^{87}$Sr/$^{88}$Sr) and elemental (Ca, Mg, Mn, Fe and Sr) signatures of Triassic sabkha dolomites. Chem. Geol. 332-333, 45-64.

Higgins, J.A., Schrag, D.P., 2010. Constraining magnesium cycling in marine sediments using magnesium isotopes. Geochim. Cosmochim. Acta 74, 5039-5053.

Hofmann, A.W., 2003. Sampling mantle heterogeneity through oceanic basalts: Isotopes and trace elements, in: Carlson, R.W., (Ed.), The Mantle and Core. Treatise on Geochemistry. Elsevier-Pergamon, Oxford, pp. 61-101.

Holland, H.D., 1984. The chemical evolution of the atmosphere and oceans. Princeton Univ. Press, Princeton, NJ.

Huang, K.-J., Teng, F.-Z., Wei, G.-J., Ma, J-.L., Bao, Z.-Y., 2012. Adsorption- and desorption-controlled magnesium isotope fractionation during extreme weathering of basalt in Hainan Island, China. Earth Planet. Sci. Lett. 359-360, 73-83.

Huang, K.-J., Teng, F.-Z., Elsenouy, A., Li ,W.-Y., Bao, Z.-Y., 2013. Magnesium isotopic variations in loess: Origins and implications. Earth Planet. Sci. Lett. 374, 60-70.

Huang, K.-J., Teng, F.-Z., Shen, B., Xiao, S., Lang, X., Ma, H.-R., Fu, Y., Peng, Y., 2016. Episode of intense chemical weathering during the termination of the 365 Ma Marinoan glaciation. PNAS 113 (520), 14904-14909.

Immenhauser, A., Buhl, D., Richter, D., Niedermayer, A., Reichelmann, D., Dietzel, M., Schulte, U., 2010. Magnesium-isotope fractionation during low-Mg calcite precipitation in a limestone cave – Field study and experiments. Geochim. Cosmochim. Acta. 74, 4346-4364.

Kelley, S.A., Chapin, C.E., 2004. Denudation history and internal structure of the Front Range and Wet Mountains, Colorado, based on apatite-fission-track thermochronology. New Mexico Bureau of Geology & Mineral Resources Bulletin 160, 41-77.

Leonard, E.M., 1989. Climatic change in the Colorado Rocky Mountains: Estimates based on modern climate at late Pleistocene equilibrium lines. Arctic and Alpine Research 21, 245-255.

Li, W.-Y., Teng, F.-Z., Ke, S., Rudnick, R. L., Gao, S., Wu, F.-Y., Chappell, B. W., 2010. Heterogeneous magnesium isotopic composition of the upper continental crust. Geochim. Cosmochim. Acta 74, 6867–6884.

Li, W.-Y., Teng, F.-Z., Xiao, Y., Huang, J., 2011. High-temperature inter-mineral magnesium isotope fractionation in eclogite from the Dabie orogeny, China. Earth Planet. Sci. Lett. 304, 224-230.

Ling, M.-X., Sedaghatpour, F., Teng, F.-Z., Hays, P.D., Strauss, J., Sun, W., 2011. Homogeneous magnesium isotopic composition of seawater: an excellent geostandard for Mg isotope analysis. Rapid Commun. Mass Spectrom. 25, 2828-2836.

Liu, S.A., Teng, F.-Z., He, Y., Ke, S., Li, S., 2010. Investigation of magnesium isotope fractionation during granite differentiation: Implication for Mg isotopic composition of the continental crust. Earth Planet. Sci. Lett. 297, 646-654.

Liu, X.-M., Teng, F.-Z., Rudnick, R.R., McDonough, W.F., Cummings, M.L., 2014. Massive magnesium depletion and isotope fractionation in weathered basalts. Geochim. Cosmochim. Acta 135, 336–349.

Ma, L., Teng, F.-Z., Jin, L., Ke, S., Yang, W., Gu, H.-O., Brantley, S.L., 2015. Magnesium isotope fractionation during shale weathering in the Shale Hills Critical Zone Observatory: Accumulation of light Mg isotopes in soils by clay mineral transformation. Chem. Geol. 397, 37-50.

Meunier, A., Velde, B., 2004. Illite: Origins, Evolution and Metamorphism. Springer-Verlag Berlin Heidelberg, New York.

Opfergelt, S., Georg, R.B., Delvaux, B., Cabidoche, Y.-M., Burton, K.W., Halliday, A.N., 2012. Mechanisms of magnesium isotope fractionation in volcanic soil weathering sequences, Guadeloupe. Earth Planet. Sci. Lett. 341-344, 176-185.

Opfergelt, S., Burton, K.W., Georg, R.B., West, A.J., Guicharnaud, R.A. Sigfusson, B., Siebert, C., Gislason, S.R., Halliday, A.N., 2014. Magnesium retention on the soil exchange complex controlling Mg isotope variations in soils, soil solutions and vegetation in volcanic soils, Iceland. Geochim. Cosmochim. Acta 125, 110-130.

Plank, T., 2014. The chemical composition of subducting sediments, in: Rudnick, R.L., (Ed.) The Crust. Treatise on Geochemistry. Elsevier, Oxford, pp. 607-629.

Pogge von Strandmann, P.A.E., Opfergelt, S., Lai, Y.-J., Sigfusson, B., Gislason, S.R., Burton, K.W., 2012. Lithium, magnesium and silicon isotope behavior accompanying weathering in a basaltic soil and pore water profile in Iceland. Earth Planet. Sci. Lett. 339-340, 11-23.

Pokrovsky, B.G., Mavromatis, V., Pokrovsky, O.S., 2011. Co-variation of Mg and C isotopes in late Precambrian carbonates of the Siberian Platform: A new tool for tracing the change in weathering regime? Chem. Geol. 290, 67-74.

Rudnick, R.L., Gao, S., 2003. Composition of the Continental Crust, in: Carlson, R.W., (Ed.), The Crust. Treatise on Geochemistry. Elsevier-Pergamon, Oxford, pp. 1-64.

Ryu, J.-S., Jacobson, A.D., Holmden, C., Lundstrom, C., Zhang, Z., 2011. The major ion, $\delta^{44/40}$Ca, $\delta^{44/42}$Ca, and $\delta^{26/24}$Mg geochemistry of granite weathering at pH = 1 and T = 25 °C: power-law processes and the relative reactivity of minerals. Geochim. Cosmochim. Acta 75, 6004–6026.

Shen, B., Jacobsen, B., Lee, C.-T.A., Yin, Q.-Z., Morton, D.M., 2009. The Mg isotopic systematics of granitoids in continental arcs and implications for the role of chemical weathering in crust formation. Proc. Natl. Acad. Sci. 106, 20652-20657.

Teng, F.-Z., Wadhwa, M., Helz, R.T., 2007. Investigation of magnesium isotope fractionation during basalt differentiation: Implications for a chondritic composition of the terrestrial mantle. Earth Planet. Sci. Lett. 261, 84–92.

Teng, F.-Z., Li, W.-Y., Ke, S., Marty, B., Dauphas, N., Huang, S., Wu F. Y., Pourmand, A., 2010a. Magnesium isotopic composition of the Earth and chondrites. Geochim. Cosmochim. Acta 74, 4150–4166.

Teng, F.-Z., Li, W.-Y., Rudnick, R.L., Gardner, L.R., 2010b. Contrasting lithium and magnesium isotope fractionation during continental weathering. Earth Planet. Sci. Lett. 300, 63-71.

Teng, F.-Z., Yang, W., 2014. Comparison of factors affecting the accuracy of high-precision magnesium isotope analysis by multi-collector inductively coupled plasma mass spectrometry. Rapid Commun. Mass Spectrom. 28, 19-24.

Teng, F.-Z., Li, W.-Y., Ke, S., Yang, W., Liu, S.-A., Sedaghatpour, S., Wang, S.-J., Huang, K.-J., Hu, Y., Ling, M.-X., Xiao, Y., Liu, X.-M., Li, X.-W., Gu, H.-O., Sio, C.K., Wallace, D.A., Su, B.-X., Zhao, L., Chamberlin, J., Harrington, M., Brewer, A., 2015. Magnesium isotopic compositions of international geological reference materials. Geostand. Geoanal. Res. 29, 329-339.

Teng, F.-Z., 2017. Magnesium Isotope Geochemistry. Rev. Mineral. Geochem. vol. 82, 219-287.

Thompson, R.S., 1991. Pliocene environments and climates in the western United States. Quat. Sci. Rev. 10, 115-132.

Tipper, E.T., Galy, A., Gaillardet, J., Bickle, M.J., Elder- field, H., Carder, E.A., 2006. The magnesium isotope budget of the modern ocean: Constraints from riverine magnesium isotope ratios, Earth Planet. Sci. Lett. 250, 241–253.

Tipper, E.T., Galy, A., Bickle, M.J., 2008. Calcium and magnesium isotope systematics in rivers draining the Himalaya-Tibetan-Plateau region: Lithological or fractionation control? Geochim. Cosmochim. Acta 72, 1057-1075.

Tipper, E.T., Calmels, D., Gaillardet, J., Louvat, P., Capmas, F., Dubacq, B., 2012. Positive correlation between Li and Mg isotope ratios in the river waters of the Mackenzie Basin challenges the interpretation of apparent isotopic fractionation during weathering. Earth Planet. Sci. Lett. 333-334, 35-45.

Urey, H.C., 1952. The Planets: Their Origin and Development. Yale University Press, New Haven, CT. 245 pp.

Wang, S.-J., Teng, F.-Z., Li, S.-G., Hong, J.-A., 2015. Magnesium isotopic systematics of mafic rocks during continental subduction. Geochim. Cosmochim. Acta 143, 34-48.

Wedepohl, K.H., 1995. The composition of the continental crust. Geochim. Cosmochim. Acta 59, 1217-1232.

Wimpenny, J., Gislason, S.R., James, R.H., Gannoun, A., Pogge von Strandmann, P.A.E., Burton, K.W., 2010. The behavior of Li and Mg isotopes during primary phase dissolution and secondary mineral formation in basalt. Geochim. Cosmochim. Acta 74, 5259-5279.

Wimpenny, J., Colla, C.A., Yin, Q.-Z., Rustad, J.R., Casey, W.H., 2014a. Investigating the behavior of Mg isotopes during the formation of clay minerals. Geochim. Cosmochim. Acta 128, 178-194.

Wimpenny, J., Yin, Q.-Z., Tollstrup, D., Xie, L.-W., Sun, J., 2014b. Using Mg isotope ratios to trace Cenozoic weathering changes: A case study from the Chinese Loess Plateau. Chem. Geol. 376, 31-43.

Yang, W., Teng, F.-Z., Zhang, H.-F., 2009. Chondritic magnesium isotopic composition of the terrestrial mantle: A case study of peridotite xenoliths from the North China craton. Earth Planet. Sci. Lett. 288, 475–482.

# CHAPTER 4: Magnesium Isotopes as a Tracer of Crustal Materials in Volcanic Arc Magmas in the Northern Cascade Arc

This chapter is published as:

*Brewer, A.B., Teng, F.-Z., Mullen, E. (2018) Magnesium isotopes as a tracer of crustal materials in volcanic arc magmas in the Northern Cascade Arc. Frontiers in Earth Sciences 6:21.*

## Abstract

Fifteen North Cascade Arc basalts and andesites were analyzed for Mg isotopes to investigate the extent and manner of crustal contributions to this magmatic system. The $\delta^{26}$Mg of these samples vary from within the range of ocean island basalts (the lightest being -0.33 ± 0.07‰) to heavier compositions (as heavy as -0.15 ± 0.06‰). The observed range in chemical and isotopic composition is similar to that of other volcanic arcs that have been assessed to date in the circum-pacific subduction zones and in the Caribbean. The heavy Mg isotope compositions are best explained by assimilation and fractional crystallization within the deep continental crust with a possible minor contribution from the addition of subducting slab-derived fluids to the primitive magma. The bulk mixing of sediment into the primitive magma or mantle source and the partial melting of garnet-rich peridotite are unlikely to have produced the observed range of Mg isotope compositions. The results show that Mg isotopes may be a useful tracer of crustal input into a magma, supplementing traditional methods such as radiogenic isotopic and trace element data, particularly in cases in which a high fraction of crustal material has been added.

## 1. Introduction

Volcanic arcs involve significant crust-mantle interactions, particularly through assimilation and fractional crystallization as magma rises to the surface and/or the addition of subducted sediment, altered oceanic crust, and slab-derived fluids to the mantle source or the primitive magma (Kelemen et al., 2007; Plank, 2014). This varied crustal material can be a major determinant of the final composition of these igneous rocks. Quantifying the crustal contribution to these magmas, and the mechanism(s) by which these materials were added, informs our understanding of the petrogenetic history of volcanic arcs, motivating the development of chemical tracers of these processes.

The unique systematics of Mg isotopes in mantle and crustal materials offer a new approach for tracing crustal additions to arc magmas. With a few exceptions, most significant Mg isotope fractionation occurs at the low temperatures of Earth's surface, while little fractionation occurs at high temperatures and pressures (Teng, 2017 and references therein). The Mg isotope compositions of uncontaminated mid-ocean ridge basalts and of the mantle are $\delta^{26}$Mg = -0.25 ± 0.07‰ and -0.25 ± 0.04‰, respectively (Teng et al., 2010a). Large deviations from the well-constrained mantle Mg isotope composition in an unweathered mafic rock may be indicative of crustal input to the magma. Surface material displays a wide range of $\delta^{26}$Mg values, from -5.57 to +1.81‰, reflecting the variety of fractionation mechanisms possible at low temperatures (Teng, 2017). During chemical weathering, for example, light isotopes are preferentially removed from a rock, which in combination with variations in watershed lithology, produces isotopically light river (Pogge von Strandmann et al., 2008; Tipper et al., 2008; Teng et al., 2010b; Huang et al., 2012) and ocean water (-0.83 ± 0.07‰; Foster et al., 2010; Ling et al., 2011). The residual silicate rock and sediment is typically isotopically heavy due to these same processes (as heavy as +1.81‰; Tipper et al., 2008, 2010; Li et al., 2010; Teng et al., 2010b; Liu et al., 2014). This chemical weathering and other associated processes, such as carbonate precipitation, have produced an extremely heterogeneous upper crust in regard to Mg isotopes, and the subduction of this material has also resulted in isotopically heterogeneous lower crust and mantle wedge material (Li et al., 2010; Teng et al., 2013; Yang et al., 2016; Wang et al., 2017).

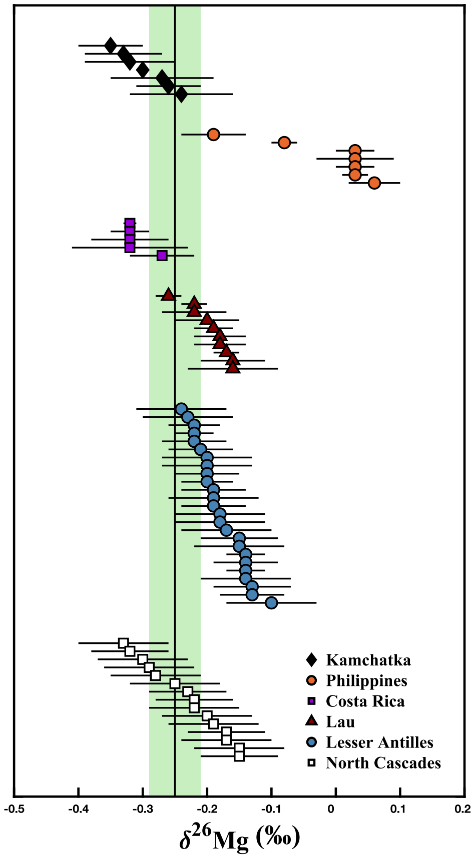

**Figure 1:** Mg isotope composition of volcanic arc samples. Lesser Antilles data from Teng et al., (2016); Kamchatka, Philippines, Costa Rica, and Lau data from Li et al., (2017); North Cascade data from the present study. The black line and green bar represent the mantle composition based on peridotite xenoliths ($\delta^{26}$Mg = -0.25 ± 0.04‰) from Teng et al., (2010a). North Cascade data are reported in Table 1. Error bars represent the 2SD for each sample.

Recent investigations into the Mg isotope systematics of volcanic arc systems in the circum-Pacific subduction zones and in the Caribbean have found samples with a wide range of Mg isotope compositions (-0.35 ± 0.05‰ to +0.06 ± 0.04‰), which has been attributed to variable slab-derived fluid additions (Figure 1; Teng et al., 2016; Li et al., 2017). To explore the effects of crustal contamination on Mg isotopes in volcanic arcs, we measured 15 samples from the North Cascade Volcanic Arc, where both uncontaminated primary magma and contaminated, evolved magmas have been previously observed. These samples are geochemically well characterized and thought to record a range of crustal content due the addition of subducted material and/or crustal assimilation during magma transport (Figure 2; Mullen and Weis, 2013, 2015; Mullen and McCallum, 2014;

Mullen et al., 2017). Our results show that the Mg isotope compositions of these arc magmas vary from within the established values for uncontaminated mantle-derived mafic magmas to relatively heavy compositions, likely due to crustal contamination (Figure 1). The use of Mg isotopes as a tracer of crustal material in magma is not limited to specific sites, but could be applicable to a variety of volcanic arc settings (Teng et al., 2016; Li et al., 2017).

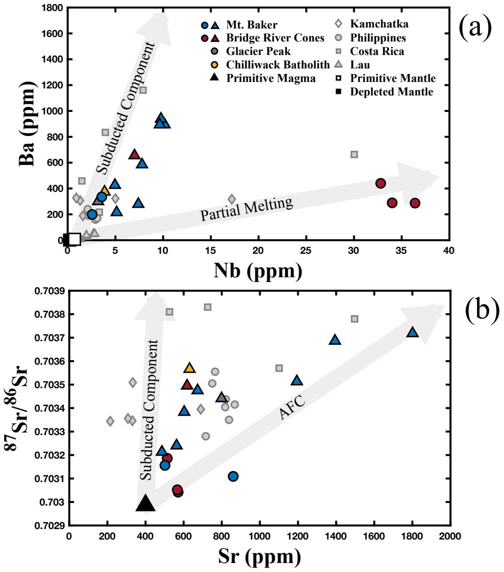

**Figure 2:** (a) Ba and Nb contents of the North Cascade samples, as well as literature data from other volcanic arcs where available. The first labeled gray arrow approximates the effects of the addition of a subducted component (bulk sediment) prior to 10% partial melting of the depleted mantle, and the second approximates the effects of partial melting of the primitive mantle for the North Cascade based on Mullen and Weis, (2013). Primitive mantle composition is from Sun and McDonough, (1989). Depleted mantle composition is from Salters and Stracke, (2004). (b) Sr isotope composition and Sr content of the North Cascade samples, as well as literature data from other volcanic arcs where available. The first labeled gray arrow approximates the effects of the addition of a subducted component (bulk sediment) to a primitive magma and the second approximates the effects of assimilation and fractionalization of a gabbro assimilant for the North Cascade based on Mullen and Weis, (2013). The primitive magma composition is based on Mullen and Weis, (2013). The colored circles represent those samples identified as most primitive from Mt. Baker and the Bridge River Cones, while the colored triangles represent samples that exhibit crustal contamination. North Cascade data are reported in Table 1. Literature data are represented by gray symbols and are from Li et al., (2017).

## 2. Samples

The Cascade Arc, located on the western margin of North America, is the result of the subduction of the Juan de Fuca plate beneath the North American plate. Most of the associated magmatic rocks contain geochemical evidence for the addition of subducted material, derived from both oceanic crust and sediment, to their mantle sources (Mullen et al., 2017). In addition, some magmas assimilated continental crust during transit to the surface (Mullen et al., 2017). We choose 15 samples from the North Cascade Volcanic Arc for Mg isotope analysis in an effort to cover samples exhibiting a wide range of known crustal content, from negligible to considerable, based on trace element compositions and Sr-Nd-Hf-Pb isotope data. The analyzed samples represent a range of locations and rock types within the northern segment of the Cascade Arc, including the Mt. Baker volcanic field, the Bridge River Cones, Glacier Peak, and the Chilliwack batholith (Tepper, 1996; Mullen and Weis, 2013, 2015; Mullen and McCallum, 2014; Mullen et al., 2017). To ensure that no weathering has occurred, all samples were collected from the interior of lava flows, were confirmed to have low LOI contents (<1%), and were examined for signs of weathering in thin section (Mullen and Weis, 2013).

The North Cascade samples fall into three petrologic groups: (1) alkali basalts from the Bridge River Cones; (2) calc-alkaline arc basalts from Mt. Baker, Glacier Peak, and the Chilliwack batholith; and (3) andesites from Mt. Baker and the Bridge River Cones. The alkali basalts from the Bridge River Cones display trace element and Sr-Nd-Hf-Pb isotope compositions that indicate an enriched mantle source and the absence of a subducted component (Figure 2; Mullen and Weis, 2013). A slab gap between the stagnant Explorer and Juan de Fuca plates near the northern termination of the arc likely facilitated upwelling of enriched asthenosphere that produced these alkali basalts nearly free of slab input (Mullen and Weis, 2013, 2015; Mullen et al., 2017). One andesite from the Bridge River Cones does show signs of crustal assimilation, like other andesites from the North Cascade (Figure 2; Mullen and Weis, 2013). Previous work has found that the calc-alkaline basalts from Mt. Baker, Glacier Peak, and the Chilliwack batholith, as well as andesites from Mt. Baker and the Bridge River Cones, demonstrate a clear subducted component, marked by elevated abundances of lead (Pb), large ion lithophile elements (LILE), and light rare earth elements (LREE) relative to high field strength elements (HSFE) (Figure 2; Mullen and McCallum, 2014; Mullen and Weis, 2013, 2015). Furthermore, the $^{87}Sr/^{86}Sr$ versus Sr systematics indicate the involvement of assimilation and fractional crystallization in the deep crust in some samples (Figure 2; Mullen and McCallum, 2014; Mullen and Weis, 2013, 2015).

## 3. Methods

Magnesium isotope analyses were performed at the Isotope Laboratory in the Department of Earth and Space Sciences at the University of Washington. All procedures are similar to those reported in previous publications (Teng et al., 2007, 2010a; Yang et al., 2009; Li et al., 2010; Teng and Yang, 2014).

The powdered rock samples were dissolved in Savillex screw-top Teflon beakers on a hotplate at approximately 125°C using a 3:1 HF-$HNO_3$ acid mixture followed by a 3:1 HCl-$HNO_3$ acid mixture. The samples were kept in each acid mixture for several days to ensure complete dissolution. To achieve cation separation, the samples were passed twice through a column containing Bio-Rad 200-400 mesh AG50W-X8 cation exchange resin in a 1N $HNO_3$ media, and were eluted using 1N $HNO_3$. The resulting Mg cut contains >99% of the Mg in the sample to prevent isotope fractionation within the column, and limits the concentrations of the other elements to less than 5% of the concentration of Mg (Teng et al., 2007).

The purified Mg samples were then analyzed on a Nu Plasma MC-ICP-MS using the standard-sample bracketing method. The Mg concentrations of the sample and standard solutions were matched to within 5% to prevent mass bias caused by a concentration mismatch (Teng and Yang, 2014). The solutions contained approx. 300 ppb Mg in 3% nitric acid. The samples were introduced using the "wet" plasma method and $^{24}Mg$, $^{25}Mg$, and $^{26}Mg$ were analyzed simultaneously using three Faraday cups (H5, Ax, and L4). Results are presented in delta notation:

$$\delta^{x}Mg\ (‰) = \left[ \frac{\left(\frac{{}^{x}Mg}{{}^{24}Mg}\right)_{Sample}}{\left(\frac{{}^{x}Mg}{{}^{24}Mg}\right)_{Standard}} - 1 \right] * 1000$$

where x refers to mass 25 or 26.

The precision of the measured $^{26}Mg/^{24}Mg$ ratio for one sample solution at the 2SD level, based on repeat standard analyses during a single analytical session, is < ± 0.07‰, comparable to previous Mg isotope studies (Li et al., 2010; Teng et al., 2010a; Ling et al., 2011; Teng and Yang, 2014). The reference materials San Carlos Olivine (n=4) and Seawater (n=3) were each analyzed at least once during an analytical session, each time yielding a $\delta^{26}Mg$ value within the established 2SD of -0.25‰ and -0.83‰ respectively. These values agree with previously published data (Teng et al., 2015; Hu et al., 2016a).

## 4. Results

Magnesium isotopic compositions, MgO concentrations, relevant trace element data, and Sr isotope compositions for the North Cascade Arc are reported in Table 1. The Mt. Baker samples range from $\delta^{26}Mg$ = -0.32 to -0.15 ± 0.06 ‰; the Bridge River Cones samples range from $\delta^{26}Mg$ = -0.33 to -0.22 ± 0.07 ‰; the Mg isotope composition of the Chilliwack Batholith and Glacier Peak samples is $\delta^{26}Mg$ = -0.23 and -0.22 ± 0.07 ‰, respectively. Weak correlations between $\delta^{26}Mg$ and MgO content, $^{87}Sr/^{86}Sr$, Th/Yb, and Pb/Ce may be evident in these samples, but given the number of processes that can affect the chemical and isotopic composition of arc magmas, clear correlations are not expected (Figures 3 and 5). No correlation is observed between Mg isotope composition and Ba/Th, Dy/Yb, or Sm/Yb (Figures 4 and 5). The increase in $\delta^{26}Mg$ from the MORB-like composition is small; however, it is resolvable with the current precision (≤0.07‰).

| Sample | $\delta^{26}$Mg (‰) | 2SD | $\delta^{25}$Mg (‰) | 2SD | MgO (wt%) | Sm/Yb | Dy/Yb | Th/Yb | Pb/Ce | Ba/Th | Ba (ppm) | Nb (ppm) | Sr (ppm) | $^{87}$Sr/$^{86}$Sr |
|---|---|---|---|---|---|---|---|---|---|---|---|---|---|---|
| *North Cascade Arc* | | | | | | | | | | | | | | |
| *Mt. Baker* | | | | | | | | | | | | | | |
| Tarn Plateau | -0.28 | 0.07 | -0.19 | 0.06 | 7.76 | 2.199 | 2.078 | 1.295 | 0.122 | 155.8 | 335 | 3.57 | 860 | 0.703109 |
| Sulphur Creek | -0.23 | 0.06 | -0.13 | 0.04 | 5.42 | 1.878 | 2.069 | 0.446 | 0.084 | 206.7 | 279 | 7.40 | 563 | 0.703240 |
| Lake Shannon | -0.29 | 0.07 | -0.19 | 0.06 | 6.44 | 1.586 | 1.918 | 0.410 | 0.100 | 195.5 | 215 | 5.13 | 486 | 0.703213 |
| Park Butte | -0.32 | 0.06 | -0.18 | 0.04 | 8.38 | 1.470 | 1.939 | 0.303 | 0.088 | 331.7 | 199 | 2.56 | 502 | 0.703156 |
| Cathedral Crag | -0.15 | 0.07 | -0.11 | 0.06 | 3.96 | 2.944 | 2.219 | 1.163 | 0.097 | 229.0 | 426 | 4.95 | 1194 | 0.703513 |
| Coleman Pinnacle 101B | -0.15 | 0.06 | -0.09 | 0.04 | 1.36 | 1.929 | 1.688 | 3.326 | 0.192 | 120.0 | 894 | 10.16 | 603 | 0.703383 |
| Coleman Pinnacle 105 | -0.17 | 0.06 | -0.10 | 0.04 | 2.84 | 3.949 | 2.178 | 3.010 | 0.185 | 158.2 | 938 | 9.77 | 1801 | 0.703718 |
| Coleman Pinnacle 86 | -0.20 | 0.07 | -0.08 | 0.06 | 2.59 | 3.110 | 1.991 | 2.749 | 0.187 | 148.5 | 894 | 9.65 | 1394 | 0.703686 |
| Table Mountain | -0.17 | 0.07 | -0.12 | 0.06 | 3.08 | 1.963 | 1.817 | 1.846 | 0.169 | 132.1 | 585 | 7.79 | 673 | 0.703475 |
| *Bridge River Cones* | | | | | | | | | | | | | | |
| Tuber Hill East Dot | -0.22 | 0.06 | -0.08 | 0.04 | 3.44 | 2.272 | 1.685 | 1.568 | 0.173 | 257.9 | 655 | 7.0 | 618 | 0.703495 |
| Tuber Hill East Cap | -0.30 | 0.07 | -0.16 | 0.06 | 4.60 | 2.928 | 2.432 | 0.808 | 0.043 | 143.1 | 289 | 34.0 | 571 | 0.703042 |
| Tuber Hill East Plateau | -0.33 | 0.07 | -0.16 | 0.06 | 3.10 | 2.752 | 2.314 | 0.625 | 0.077 | 212.6 | 440 | 32.8 | 514 | 0.703186 |
| Nichols Valley | -0.25 | 0.07 | -0.14 | 0.06 | 4.44 | 3.043 | 2.361 | 0.816 | 0.037 | 140.0 | 287 | 36.4 | 567 | 0.703052 |
| *Chilliwack Batholith* | | | | | | | | | | | | | | |
| Mount Sefrit | -0.23 | 0.07 | -0.09 | 0.06 | 6.80 | 2.550 | 2.015 | 1.329 | 0.164 | 161.3 | 300 | 3.19 | 799 | 0.703441 |
| *Glacier Peak* | | | | | | | | | | | | | | |
| Dishpan Gap | -0.22 | 0.07 | -0.14 | 0.06 | 4.47 | 2.129 | 1.817 | 1.378 | 0.139 | 112.7 | 374 | 3.87 | 631 | 0.703566 |
| *Standards* | | | | | | | | | | | | | | |
| Seawater | -0.81 | 0.07 | -0.43 | 0.06 | | | | | | | | | | |
| Replicate | -0.88 | 0.07 | -0.54 | 0.06 | | | | | | | | | | |
| Replicate | -0.83 | 0.07 | -0.50 | 0.06 | | | | | | | | | | |
| SC Olivine | -0.23 | 0.07 | -0.05 | 0.06 | | | | | | | | | | |
| Duplicate | -0.25 | 0.07 | -0.20 | 0.06 | | | | | | | | | | |
| Duplicate | -0.31 | 0.06 | -0.15 | 0.04 | | | | | | | | | | |
| Replicate | -0.24 | 0.06 | -0.11 | 0.04 | | | | | | | | | | |

**Table 1:** Magnesium isotope and trace element compositions of samples and standards. North Cascade major and trace element data from Mullen et al., (2017), Mullen and McCallum, (2013, 2014), Mullen and Weis, (2015). 2SD = Two standard deviation of the population of n (15 < n < 22) repeat measurements of the standards during an analytical session.

## 5. Discussion

### *5.1 Mg isotope variations in the North Cascade Volcanic Arc*

The alkali basalts from the Bridge River Cones are essentially free of crustal contamination based on trace element and Sr-Nd-Hf-Pb isotope data; a conclusion which is supported by Mg isotope systematics (Figure 2; Mullen and Weis, 2013). The samples, with $\delta^{26}$Mg between -0.33 and -0.25 ± 0.07 ‰, fall within the range of Mg isotope compositions exhibited by MORBs ($\delta^{26}$Mg = -0.31 to -0.19‰) and OIBs ($\delta^{26}$Mg = -0.35 to -0.18‰) (Teng et al., 2010a). They do not reach the heavier compositions found elsewhere in the North Cascade, for example at Mt. Baker (Figure 3). Thus, the Mg isotope composition of these basalts supports the conclusion that the Bridge River Cones likely reflect the melting of a primitive mantle source with little to no contribution from subducted material or assimilated continental crust (Figure 3; Mullen and Weis, 2013).

The calc-alkaline arc basalts from Mt. Baker, Glacier Peak, and the Chilliwack batholith and the andesites from Mt. Baker and the Bridge River Cones do show the influence of subducted material and/or assimilation and fractional crystallization of the continental crust (Mullen and McCallum, 2014). While all of these samples are thought to exhibit some crustal contamination, we consider the Tarn Plateau and Park Butte samples to be the most primitive, given their high MgO contents (>7 wt%), high Mg# (>0.6), and relatively high compatible trace element content (e.g. Cr >200 ppm) (Mullen and Weis, 2013, 2015; Mullen and McCallum, 2014). The Mg isotope compositions of these samples are also quite light (-0.28 ± 0.07 ‰ and -0.32 ± 0.07 ‰, respectively), similar to the primitive alkali basalts from the Bridge River Cones, which are known to contain little crustal contamination (Figure 3). The remainder of the calc-alkaline basalts and andesites display variable crustal involvement from subducted material and/or assimilated continental crust (Tepper, 1996; Mullen and Weis, 2013, 2015; Mullen and McCallum, 2014). The relatively heavy Mg isotope compositions of these samples likely reflects the addition of isotopically heavy crustal material, such as subducted sediment ($\delta^{26}$Mg = -3.65 to +0.52‰), altered oceanic crust ($\delta^{26}$Mg = -2.76 to +0.21‰), and deep continental crust ($\delta^{26}$Mg = -0.76 to +0.19‰) (Figure 3; Huang, 2013; Teng et al., 2013; Hu et al., 2017; Yang et al., 2016). The following sections will examine the possible causes of the elevated Mg isotope compositions of these arc samples.

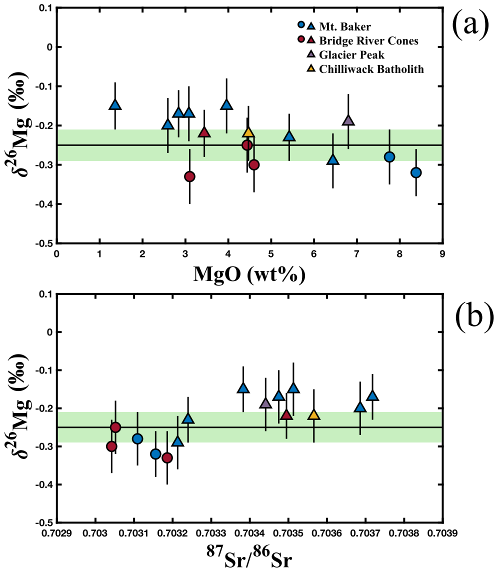

**Figure 3:** (a) Variation of $\delta^{26}$Mg with wt% MgO. (b) Variation of $\delta^{26}$Mg with $^{87}$Sr/$^{86}$Sr. The colored circles represent those samples identified as most primitive from Mt. Baker and the Bridge River Cones, while the colored triangles represent samples that exhibit crustal contamination. The black line and green bar represent the mantle composition based on peridotite xenoliths ($\delta^{26}$Mg = -0.25 ± 0.04‰) from Teng et al., (2010a). North Cascade data are reported in Table 1. Error bars represent the 2SD for each sample.

### *5.2 Hypotheses for Mg Isotope Variations*

The observed increase in Mg isotope composition may be the result of one of three processes, or a combination thereof: the primary melt was derived from partial melting of garnet-rich peridotite, isotopically heavy subducted material was added to the primitive magmas or the mantle source, or the primitive magmas underwent assimilation and fractional crystallization during transport within the continental crust.

Garnet has a light Mg isotope composition compared to coexisting silicates (Li et al., 2011, 2016; Wang et al., 2012, 2014; Huang et al., 2013). The difference in Mg coordination between garnet (8-fold) and most silicate minerals (6-fold) causes $^{24}$Mg to be preferentially incorporated into garnet, leaving the surrounding minerals enriched in $^{26}$Mg (Li et al., 2011, 2016; Wang et al., 2012, 2014; Huang et al., 2013). Both equilibrium and disequilibrium inter-mineral fractionation can occur between garnet and coexisting silicates (Li et al., 2016). Therefore, partial melting that leaves a garnet-rich residue could produce a melt with a relatively heavy Mg isotope composition. However, the trace element data do not support this explanation for the origin of the isotopically heavy magmas. Because of the affinity of the HREE for garnet, partial melts leaving a garnet-rich residue would also display relatively high Sm/Yb and Dy/Yb ratios (Lassiter and DePaolo, 1997). Therefore, $\delta^{26}$Mg should be positively correlated with Sm/Yb and Dy/Yb, which is not observed in the North Cascade or any other volcanic arc assessed to date (Figure 4). Furthermore, previous work has ruled out residual garnet for Mt. Baker and Glacier Peak based on trace element modeling (Mullen and Weis, 2013, 2015). Residual garnet associated with the Bridge River Cones is likely, however, those samples do not exhibit heavy Mg isotope compositions (Mullen and Weis, 2013). We therefore conclude

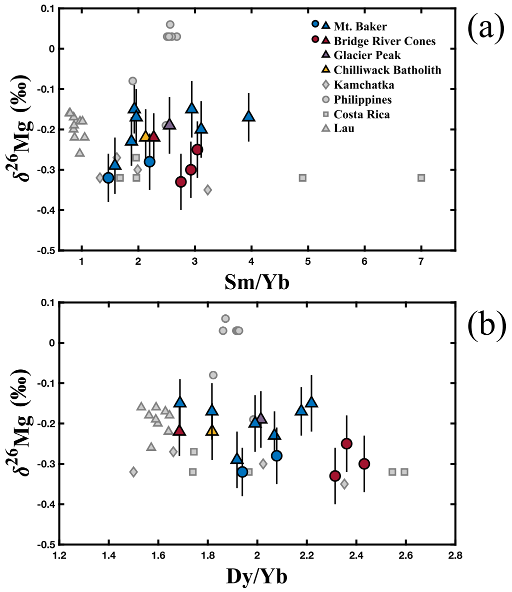

**Figure 4:** Variation of $\delta^{26}$Mg with (a) Sm/Yb and (b) Dy/Yb ratios. The colored circles represent those samples identified as most primitive from Mt. Baker and the Bridge River Cones, while the colored triangles represent samples that exhibit crustal contamination. North Cascade data are reported in Table 1. Literature data are represented by gray symbols and are from Li et al., (2017). Error bars represent the 2SD for each North Cascade sample.

that partial melting in the presence of garnet is unlikely to have produced the observed Mg isotope compositions.

The addition of a crustal component to the magmas is more consistent with the Mg isotope data. Because crustal material, such as subducted sediment, generally has lower MgO contents than the mantle source and primitive magmas (McDonough and Sun, 1995; Rudnick and Gao, 2003; Plank, 2014), crustal input into a magma is generally associated with a decrease in MgO. Fractional crystallization can produce similar changes in chemical composition; however, fractional crystallization does not fractionate Mg isotopes, with the exception of processes associated with garnet (Teng, 2017 and references therein). A heavy Mg isotope composition in these samples is also associated with increased $^{87}Sr/^{86}Sr$, which is expected given that crustal materials have elevated $^{87}Sr/^{86}Sr$ compared to most mantle-derived melts (Kelemen et al., 2007; Plank, 2014). Slab-derived fluid additions to the mantle wedge are typically associated with increases in Pb/Ce and Ba/Th ratios, while

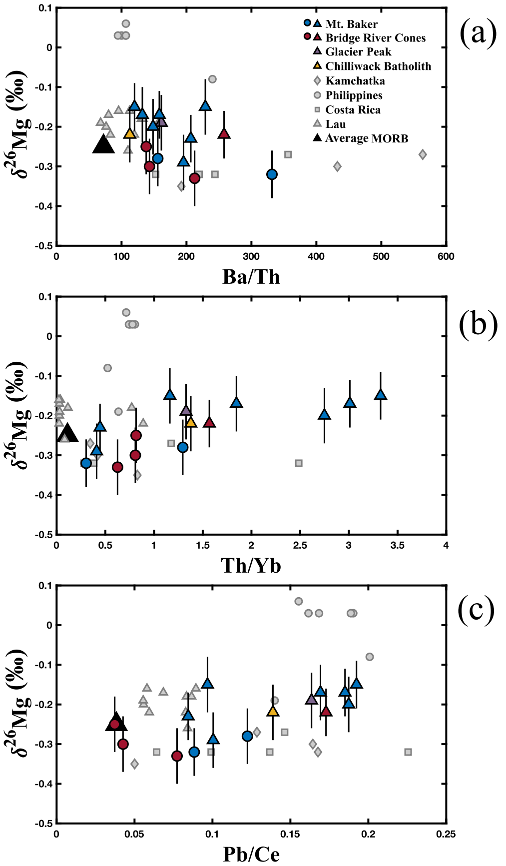

**Figure 5:** Variation of $\delta^{26}$Mg with, Ba/Th (a), Th/Yb (b), and Pb/Ce (c). The black triangles represent the average MORB composition. MORB $\delta^{26}$Mg value (-0.25 ± 0.07‰) is from Teng et al., (2010a), Th/Yb (0.1113), Pb/Ce (0.0384), and Ba/Th (72.2772) are from Gale et al., (2013). The colored circles represent those samples identified as most primitive from Mt. Baker and the Bridge River Cones, while the colored triangles represent samples that exhibit crustal contamination. Literature data are represented by gray symbols and are from Li et al., (2017). North Cascade data are reported in Table 1. Error bars represent the 2SD for each North Cascade sample.

subducted sediment melts are typically associated with increased Th/Yb ratios. Weak correlations between $\delta^{26}$Mg and Pb/Ce and Th/Yb may be present in these samples, but no correlation with Ba/Th is observed (Figure 3). Taken together, the North Cascade Volcanic Arc samples exhibit a range of Mg isotope compositions that is best explained by crustal additions, rather than garnet involvement.

### *5.3 Modeling Crustal Input*

To investigate the origin of crustal contributions to the North Cascade Arc, an AFC model (DePaolo, 1981) combining primitive magma and lower continental crust and two different two-component bulk-mixing models (primitive magma + subducted sediment and depleted mantle + subducted sediment) were constructed for the North Cascade Arc (Figure 6). The models are designed to be representative of the calc-alkaline arc basalts from Mt. Baker, Glacier Peak, and the Chilliwack batholith and the andesites from Mt. Baker and the Bridge River Cones, but not the alkali basalts from the Bridge River Cones since they are known to be petrogenetically distinct from the other samples. All end-member compositions and other model parameters are listed in Table 2.

| Sample | $\delta^{26}$Mg (‰) | MgO (wt%) | Sr (ppm) | $^{87}$Sr/$^{86}$Sr |
|---|---|---|---|---|
| *End-Member Compositions* | | | | |
| Depleted Mantle | -0.25[1] | 38.2[4] | 9.8[4] | 0.70260[4] |
| Primitive Magma | -0.30 | 8.38 | 502 | 0.70311 |
| Lower Crust | -0.05[2] | 6.57[5] | 401[5] | 0.70400[5] |
| Subducted Sediment | +0.20[3] | 2.53[6] | 323[6] | 0.71490[6] |
| *Modeling Parameters* | | | | |
| $D_{Sr}$ | 3.2[7] | | | |
| $D_{MgO}$ | 3.0[7] | | | |
| r | 0.5[7] | | | |

[1] Teng et al., (2010a)
[2] Yang et al., (2016)
[3] Hu et al., (2017)
[4] Salters and Stracke, (2004)
[5] Mullen and Weis, (2013)
[6] Plank, (2014)
[7] Teng et al., (2016)

**Table 2:** Modeling parameters and end-member compositions

The primitive magma composition was selected based on the samples judged to be the most primitive in the Mt. Baker dataset (Tarn Plateau and Park Butte). The depleted mantle composition is from Salters and Stracke, (2004), with the exception of the Mg isotope composition (-0.25 ‰), which is the canonical mantle value described in Teng et al., (2010a) and

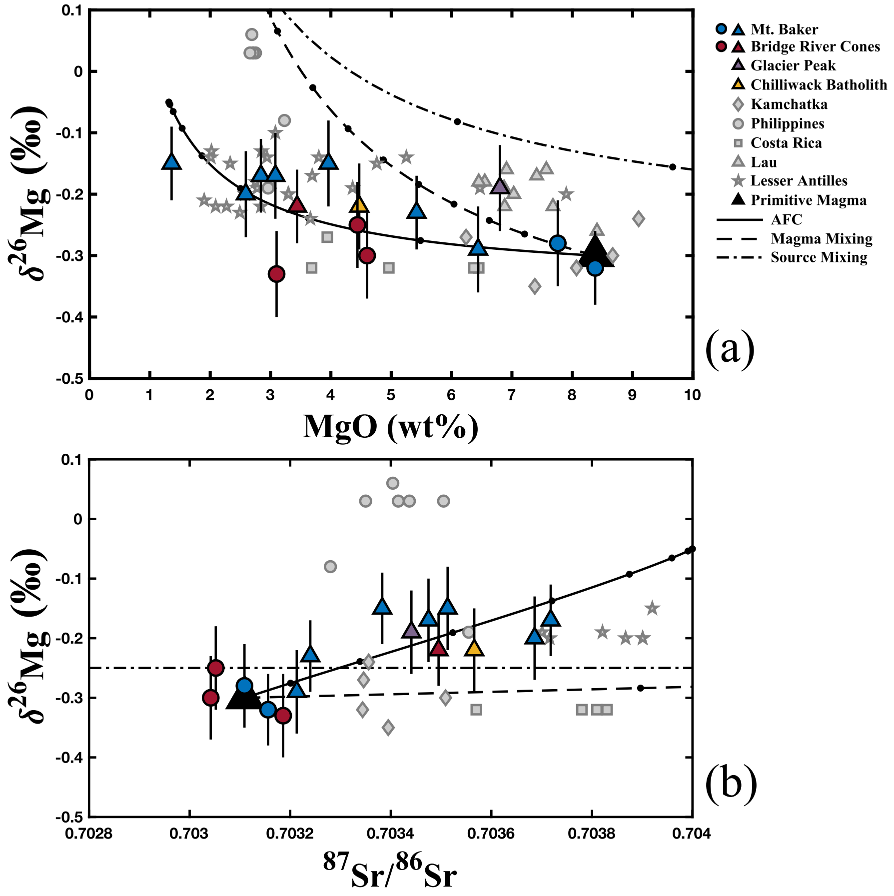

**Figure 6:** AFC (assimilation-fractional crystallization) and bulk mixing models for $\delta^{26}$Mg vs. wt% MgO (a) and $^{87}$Sr/$^{86}$Sr (b) for the North Cascade samples and available literature data. The colored circles represent those samples identified as most primitive from Mt. Baker and the Bridge River Cones, while the colored triangles represent samples that exhibit crustal contamination. The dashed and dotted line represents bulk mixing between depleted mantle and subducted sediment; the dashed line represents bulk mixing between primitive magma and subducted sediment; the solid line represents assimilation and fractional crystallization of lower continental crust by the primitive magma. Table 2 contains the end-member compositions, modeling parameters, and their sources. The black circles along the modeled curves represent 10% bulk mixing increments, and 10% crystallization increments in the AFC model. The black triangle represents the initial primitive magma end-member. Error bars represent the 2SD for each North Cascade sample. North Cascade data are reported in Table 1. Literature data (grey symbols) are from Li et al., (2017) and Teng et al., (2016).

elsewhere (Huang et al., 2011; Hu et al., 2016b; Wang et al., 2016). The lower continental crust composition is based on the North Cascade lower crust end-member from Mullen and Weis, (2013). The Mg isotope composition of the lower crust in this region is unknown, so a reasonable composition (-0.05 ‰) was selected based on the range exhibited by lower crustal material in Yang et al., (2016). Finally, the subducted sediment end-member is based on the subducted sediment at the Cascade from Plank, (2014). However, the Mg isotope composition of the subducted sediment component affecting the mantle source or primitive magma is unknown, so again a reasonable value (+0.20 ‰) was selected based on Hu et al., (2017). For the AFC models, the ratio of assimilation to crystallization was fixed at 0.5, and the bulk partition coefficients for MgO and Sr were estimated and fixed at 3.0 and 3.2, respectively, after the volcanic arc modeling of Teng et al., (2016). Minor changes in the bulk partition coefficients have little impact on the model. Although some of the relevant modeling parameters can only be estimated, these models do demonstrate that AFC is a feasible explanation for the observed data, while bulk mixing alone is not.

The North Cascade Arc two-component bulk mixing models are unable to reproduce the observed trends in the data, particularly the Sr isotope compositions. To approximate the MgO content and Mg isotope composition of some North Cascade samples with the primitive magma mixing model, the sediment must contribute more than 50% of the final magma, which is unreasonably high (Figure 6a). The Sr and Mg isotope primitive magma mixing model predicts very little change in Mg isotope composition across the whole range of Sr isotope compositions observed in the samples, which does not agree with the observed data (Figure 5b). The two-component mantle source mixing model requires an even higher fraction of crustal material (more than 80%) to produce the observed Mg isotope compositions given the high MgO content of the mantle, and again no change in Mg isotope composition is predicted for the observed range in Sr isotopes (Figure 5). Therefore, bulk sediment additions to the primitive magma or mantle source are unlikely to be the cause of the elevated Mg isotope compositions found in the North Cascade Arc samples.

Assimilation and fractional crystallization in the deep continental crust, on the other hand, can match the observed trends without an excessively high crustal contribution. The observed major element and isotopic trends can be reproduced with between 100% and 60% liquid remaining in the system (Figure 6). Unlike the bulk mixing models, AFC can approximate the observed increase in Mg isotope composition within the range of Sr isotope compositions exhibited by the samples (Figure 6). Given the elevated Pb/Ce and Ba/Th ratios, and the apparent correlation between $\delta^{26}$Mg and Pb/Ce in these samples, fluid additions may also have made a minor contribution to the final Mg isotope compositions. However, quantifying the slab-derived fluid effect on Mg isotopes is not currently possible given our limited understanding of Mg isotope behavior during slab dehydration. Assimilation and fractional crystallization is the favored explanation for the increase in Mg isotope composition, and while minor effects from the addition of slab-derived fluids to the mantle source and primitive may have occurred, those processes are unlikely to the primary cause of the heavy Mg isotope compositions observed in the North Cascade Volcanic Arc.

The Mg isotope compositions exhibited by the North Cascade Volcanic Arc samples are similar to those from previously analyzed volcanic arcs (Figure 1). Li et al., (2017) analyzed arc samples from Kamchatka ($\delta^{26}$Mg = -0.35 ± 0.05 to -0.24 ± 0.08 ‰), the Philippines (-0.19 ± 0.05 to +0.06 ± 0.04 ‰), Costa Rica (-0.32 ± 0.01 to -0.27 ± 0.05 ‰), and Lau (-0.26 ± 0.02 to -0.16 ± 0.05 ‰), while Teng et al., (2016) analyzed samples from the Lesser Antilles (-0.24 ± 0.07 to -

0.10 ± 0.07 ‰). The Cascade samples (-0.33 ± 0.07 to -0.15 ± 0.06 ‰) have similar Mg isotope compositions to the samples from all of those locations except the Philippines, which have unusually heavy compositions (Li et al., 2017). The present dataset fills in a gap in the Mg isotope data for arc volcanics from the circum-Pacific subduction zones, representing the margin along the northwestern coast of North America. The similarity to these other arc samples, including those from the Lesser Antilles in the Caribbean, demonstrates that the processes affecting Mg isotopes are likely consistent from margin to margin. Much of the combined data for the volcanic arcs worldwide can be approximated by the same assimilation and fractional crystallization model used with the North Cascade samples (Figure 6). AFC processes are, therefore, the most likely explanation for the range in Mg isotope data observed in volcanic arcs. Small differences in the Mg isotope compositions of the primitive magma, subducted sediment, and assimilated lower crust between and within different arcs likely do impact the final magma composition, producing the observed variety between the arcs.

Although crustal input to the North Cascade magmas produced only small, just beyond two-sigma analytical uncertainty, variations from normal mantle values, this likely required a significant crustal addition. Nonetheless, improvements in analytical precision may make possible the use of Mg isotopes as a valuable tracer of crustal recycling that is complementary to established methods such as Sr-Nd-Hf-Pb isotopic and trace element data. The crustal materials that may be involved in arc volcanism, including subducted sediment and sediment melt, altered oceanic crust, slab-derived fluids, and assimilated continental crust, have extremely varied Mg isotope compositions. This variability, along with the lack of fractionation during most high temperature processes, may permit Mg isotopes to be a valuable tool in tracing arc volcanic processes. With a thorough understanding of the composition of these different reservoirs, Mg isotope systematics, combined with existing geochemical indicators, would elucidate the nature of crustal input in a given arc. Furthermore, Mg isotopes may provide a solution for detecting crustal input in settings where commonly-used radiogenic isotopes are ambiguous due to lack of isotopic contrast between the crust and primary magmas (e.g. Mullen et al., 2017). These findings also represent a significant step in our understanding of the Mg cycle by demonstrating that silicate material from the crust can alter the isotopic composition of a magma.

## 6. Summary

The main conclusions from this study are:

1. The Mg isotope composition of samples from the North Cascade Arc range from -0.33 ± 0.07‰ to -0.15 ± 0.06‰.
2. The alkali basalts from the Bridge River Cones reflect the partial melting of the mantle source with minimal crustal contamination, while the calc-alkaline basalts and andesites from Mt. Baker, Glacier Peak, Chilliwack Batholith, and the Bridge River Cones do have Mg isotope compositions indicative of variable crustal contamination.
3. The samples with high $\delta^{26}$Mg are best explained by the addition of isotopically heavy deep continental crust to primitive magmas through assimilation and fractional crystallization with a possible minor contribution from slab-derived fluids.
4. With further study and analytical improvements, Mg isotopes will become a useful tool in understanding the generation and evolution of magmatic rocks.

## Acknowledgements

We would like to thank Shui-Jiong Wang for his extensive help throughout this study, Florence Yuen, Khadijah Karrington Homolka, and Jiarui Zhou for their work in the clean lab, and Kwan-Nang Pang and I. Stewart McCallum for their insightful comments. P. Adam and J.

Tepper are acknowledged for providing samples from the Bridge River Cones and the Chilliwack batholith, respectively. We would also like to thank Julia Ribeiro for her careful editing and Thomas Zambardi and two anonymous reviewers for their constructive comments on a previous version of this manuscript. This work was supported by an NSF grant (EAR-17407706).

## References

DePaolo DJ (1981). Trace element and isotopic effects of combined wallrock assimilation and fractional crystallization. Earth Planet Sc Lett 53:189-202 doi:10.1016/0012-821X(81)90153-9

Foster GL, Pogge von Strandmann PAE, Rae JWB (2010). Boron and magnesium isotope composition of seawater. Geochem Geophy Geosy 11(8) doi:10.1029/2010GC003201

Gale A, Dalton CA, Langmuir CH, Su Y, Schilling JG (2013). The mean composition of ocean ridge basalts. Geochem Geophy Geosy 14(3):1525-2027 doi:10.1029/2012GC004334

Hu Y, Harrington MD, Sun Y, Yang Z, Konter J, Teng FZ (2016a). Magnesium isotopic homogeneity of San Carlos olivine: a potential standard for Mg isotopic analysis by multi-collector inductively coupled plasma mass spectrometry. Rapid Commun Mass Sp 30(19):2123-2132 doi:10.1002/rcm.7700

Hu Y, Teng FZ, Zhang HF, Xiao Y, Su BX (2016b) Metasomatism-induced mantle magnesium isotopic heterogeneity: Evidence from pyroxenites. Geochim Cosmochim Ac 185:88-111 doi:10.1016/j.gca.2015.11.001

Hu Y, Teng FZ, Plank T, Huang KJ (2017) Magnesium isotopic composition of subducting marine sediments. Chem Geol 466:15-31 doi:10.1016/j.chemgeo.2017.06.010

Huang F, Chen LJ, Wu ZQ, Wang W (2013). First-principles calculations of equilibrium Mg isotope fractionations between garnet, clinopyroxene, orthopyroxene, and olivine: Implications for Mg isotope thermometry. Earth Planet Sc Lett 367:61-70 doi:10.1016/j.epsl.2013.02.025

Huang F, Zhang ZF, Lundstrom CC, Zhi XC (2011) Iron and magnesium isotopic compositions of peridotite xenoliths from Eastern China. Geochim Cosmochim Ac 75:3318-3334 doi:10.1016/j.gca.2011.03.036

Huang KJ (2013) The behavior of magnesium isotopes during low-temperature water-rock interactions. PhD Dissertation. China University of Geosciences, Wuhan, China.

Huang KJ, Teng FZ, Wei GJ, Ma JL, Bao ZY (2012). Adsorption- and desorption-controlled magnesium isotope fractionation during extreme weathering of basalt in Hainan Island, China. Earth Planet Sc Lett 359:73-83 doi:10.1016/j.epsl.2012.10.007

Kelemen PB, Hanghoj K, Greene AR (2007). One view of the geochemistry of subduction-related magmatic arcs, with an emphasis on primitive andesite and lower crust. In: Holland HD, Turekian KK (ed) Treatise on Geochemistry 2nd Edition, vol The Crust. Elsevier, Oxford, pp 1-70 doi:10.1016/B0-08-0435751/03035-8

Lassiter JC, Depaolo DJ (1997). Plume/Lithosphere interaction in the generation of continental and oceanic flood basalts: Chemical and isotopic constraints. In: Mahoney JJ, Coffin MF (ed) Large Igneous Provinces: Continental, Oceanic, and Planetary Flood Volcanism, American Geophysical Union, Washington D.C. doi:10.1029/GM100p0335

Li SG, Yang W, Ke S, Meng X, Tian H, Xu L, et al. (2017). Deep carbon cycles constrained by a large-scale mantle Mg isotope anomaly in eastern China. Nat. Sci. Review 4(1): 111-120. doi:10.1093/nsr/nww070

Li WY, Teng FZ, Ke S, Rudnick RL, Gao S, Wu FY, et al. (2010). Heterogeneous magnesium isotopic composition of the upper continental crust. Geochim Cosmochim Ac 74(23):6867-6884 doi:10.1016/j.gca.2010.08.030

Li WY, Teng FZ, Xiao YL, Gu HO, Zha XP, Huang J (2016). Empirical calibration of the clinopyroxene-garnet magnesium isotope geothermometer and implications. Contrib Mineral Petrol 171:61 doi:10.1007/s00410-016-1269-1

Li WY, Teng FZ, Xiao YL, Huang JA (2011). High-temperature inter-mineral magnesium isotope fractionation in eclogite from the Dabie orogen, China. Earth Planet Sc Lett 304(1-2):224-230 doi:10.1016/j.epsl.2011.01.035

Ling MX, Sedaghatpour F, Teng FZ, Hays PD, Strauss J, Sun WD (2011). Homogeneous magnesium isotopic composition of seawater: an excellent geostandard for Mg isotope analysis. Rapid Commun Mass Sp 25(19):2828-2836 doi:10.1002/rcm.5172

Liu XM, Teng FZ, Rudnick RL, McDonough WF, Cummings ML (2014). Massive magnesium depletion and isotope fractionation in weathered basalts. Geochim Cosmochim Ac 135:336-349 doi:10.1016/j.gca.2014.03.028

McDonough WF, Sun SS (1995). The Composition of the Earth. Chem Geol 120(3-4):223-253 doi:10.1016/0009-2541(94)00140-4

Mullen EK, McCallum IS (2013). Coexisting pseudobrookite, ilmenite, and titanomagnetite in hornblende andesite of the Coleman Pinnacle flow, Mount Baker, Washington: Evidence for a highly oxidized arc magma. Am Mineral 98(2-3):417-425 doi:10.2138/am.2013.4185

Mullen EK, McCallum IS (2014). Origin of Basalts in a Hot Subduction Setting: Petrological and Geochemical Insights from Mt. Baker, Northern Cascade Arc. J Petrol 55(2):241-281 doi:10.1093/petrology/egt064

Mullen EK, Weis D (2013). Sr-Nd-Nf-Pb isotope and trace element evidence for the origin of alkali basalts in the Garabaldi Belt, northern Cascade arc. Geochem Geophy Geosy 14:3126-3155 doi:10.1002/ggge.20191

Mullen EK, Weis D (2015). Evidence for trench-parallel mantle flow in the northern Cascade Arc from basalt geochemistry. Earth Planet Sc Lett 414:100-107 doi:10.1016/j.epsl.2015.01.010

Mullen EK, Weis D, Marsh NB, Martindale M (2017). Primitive arc magma diversity: New geochemical insights in the Cascade Arc. Chem Geol 448:43-70 doi:10.1016/j.chemgeo.2016.11.006

Plank T (2014). The chemical composition of subducting sediments. In: Holland HD, Turekian KK (ed) Treatise on Geochemistry 2nd Edition, vol The Crust. Elsevier, Oxford, pp 607-629 doi:10.1016/B978-0-08-095975-7.00319-3

Pogge von Strandmann PAE, Burton KW, James RH, van Calsteren P, Gislason SR, Sigfusson B (2008). The influence of weathering processes on riverine magnesium isotopes in a basaltic terrain. Earth Planet Sc Lett 276(1-2):187-197 doi:10.1016/j.epsl.2008.09.020

Rudnick RL, Gao S (2003). Composition of the Continental Crust. In: Rudnick RL, Holland HD, Turekian KK (ed) Treatise on Geochemistry, vol The Crust. Elsevier, Oxford, pp 1-64 doi:10.1016/B0-08-043751-6/03016-4

Salters VJM, Stracke A (2004). Composition of the depleted mantle. Geochem Geophy Geosy 5(5) doi:10.1029/2003GC000597

Sun W, McDonough WF (1989) Chemical and isotopic systematics of oceanic basalts: Implications for mantle composition and processes. Geological Society, London, Special Publications vol. 42, 313-345 doi:10.1144/GSL.SP.1989.042.01.19

Teng FZ (2017). Magnesium Isotope Geochemistry. Reviews in Mineralogy and Geochemistry vol. 82, 219-287 doi:10.2138/rmg.2017.82.7

Teng FZ, Li WY, Ke S, Yang W, Liu SA, Sedaghatpour F, et al. (2015). Magnesium isotopic composition of international geostandards. Geochem Geophy Geosy 39:329-339 doi: 10.1111/j.1751-908X.2014.00326.x

Teng FZ, Hu Y, Chauvel C (2016). Magnesium isotope geochemistry in arc volcanism. P Natl Acad Sci USA 113(26):7082-7087 doi:10.1073/pnas.1518456113

Teng FZ, Li WY, Ke S, Marty B, Dauphas N, Huang SC, et al. (2010a). Magnesium isotopic composition of the Earth and chondrites. Geochim Cosmochim Ac 74(14):4150-4166 doi:10.1016/j.gca.2010.04.019

Teng FZ, Li WY, Rudnick RL, Gardner LR (2010b). Contrasting lithium and magnesium isotope fractionation during continental weathering. Earth Planet Sc Lett 300(1-2):63-71 doi:10.1016/j.epsl.2010.09.036

Teng FZ, Wadhwa M, Helz RT (2007). Investigation of magnesium isotope fractionation during basalt differentiation: Implications for a chondritic composition of the terrestrial mantle. Earth Planet Sc Lett 261(1-2):84-92 doi:10.1016/j.epsl.2007.06.004

Teng FZ, Yang W (2014). Comparison of factors affecting the accuracy of high-precision magnesium isotope analysis by multi-collector inductively coupled plasma mass spectrometry. Rapid Commun Mass Sp 28(1):19-24 doi:10.1002/rcm.6752

Teng FZ, Yang W, Rudnick RL, Hu Y (2013). Heterogeneous magnesium isotopic composition of the lower continental crust: A xenolith perspective. Geochem Geophy Geosy 14(9):3844-3856 doi:10.1002/ggge.20238

Tepper JH (1996). Petrology of mafic plutons associated with calc-alkaline granitoids, Chilliwack Batholith, north Cascade, Washington. J Petrol 37(6):1409-1436 doi:10.1093/petrology/37.6.1409

Tipper ET, Galy A, Bickle MJ (2008). Calcium and magnesium isotope systematics in rivers draining the Himalaya-Tibetan-Plateau region: Lithological or fractionation control? Geochim Cosmochim Ac 72(4):1057-1075 doi:10.1016/j.gca.2007.11.029

Wang SJ, Teng FZ, Li SG, Hong JA (2014). Magnesium isotopic systematics of mafic rocks during continental subduction. Geochim Cosmochim Ac 143:34-48 doi:10.1016/j.gca.2014.03.029

Wang SJ, Teng FZ, Li SG, Zhang LF, Du JX, He YS, et al. (2017). Tracing subduction zone fluid-rock interactions using trace element and Mg-Sr-Nd isotopes. Lithos 290-291:94-103 doi:10.1016/j.lithos.2017.08.004

Wang SJ, Teng FZ, Scott JM (2016) Tracing the origin of continental HIMU-like intraplate volcanism using magnesium isotope systematics. Geochim Cosmochim Ac 185:78-87 doi:10.1016/j.gca.2016.01.007

Wang SJ, Teng FZ, Williams HM, Li SG (2012). Magnesium isotopic variations in cratonic eclogites: Origins and implications. Earth Planet Sc Lett 359:219-226 doi:10.1016/j.epsl.2012.10.016

Yang W, Teng FZ, Li WY, Liu SA, Ke S, Liu YS, et al. (2016). Magnesium isotopic composition of the deep continental crust. Am Mineral 101(1-2):243-252 doi:10.2138/am-2016-5275

Yang W, Teng FZ, Zhang HF (2009). Chondritic magnesium isotopic composition of the terrestrial mantle: A case study of peridotite xenoliths from the North China craton. Earth Planet Sc Lett 288(3-4):475-482 doi:10.1016/j.epsl.2009.10.009

# CHAPTER 5: Recovery of rare earth elements from geothermal fluids through bacterial cell surface adsorption

This chapter is in revision for publication as:

*Brewer, A.B., Chang, E., Park, D.M., Kou, T., Li, Y., Lammers, L.N., Jiao, Y. (2018) Recovery of rare earth elements from geothermal fluids through bacterial cell surface adsorption. Environmental Science & Technology.*

## Abstract

Rare earth elements (REEs) are in increasing demand in the modern economy and yet meaningful REE production is limited to only a few locations worldwide, which motivates the development of novel strategies to enable cost-effective REE recovery from non-traditional feedstocks. We investigate biosorption as a potential means of recovering REEs from geothermal fluids, a low-grade but abundant REE source. We have previously engineered *E. coli* to express lanthanide binding tags (LBTs) on the cell surface and the resulting strain showed an increase in both REE adsorption capacity and selectivity. Here we examined how REE adsorption by the engineered *E. coli* is affected by various geochemical factors relevant to geofluids, including total dissolved solids (TDS), temperature, pH, and the presence of specific competing metals. REE biosorption is robust to high TDS concentrations, with high extraction efficiency and selectivity observed in geofluids containing REE concentrations as low as 100 ppb and TDS as high as 165,000 ppm. Among several metals tested, U, Al, and Pb were found to be the most competitive, causing significant reductions (>25%) in REE biosorption when present at concentrations ~3 to 11-fold higher than the REEs. Optimal REE biosorption occurs between pH 5-6, with significant loss in sorption capacity (~65%) as pH decreases from 6 to 2. REE

extraction efficiency and selectivity increase as a function of temperature up to ~70°C, which can be explained by the thermodynamic properties of metal complexation on the bacterial surface. Together, these data demonstrate the potential utility of biosorption for selective REE recovery from geothermal fluids by defining the optimal and boundary conditions for this extraction technology.

## Introduction

Rare earth elements (REEs) are becoming increasingly significant to the international economy with the emergence and development of new technologies, particularly in the area of clean energy. Common applications of REEs include automotive and industrial catalysts, permanent magnets, and electronics. However, the supply of these metals is uncertain and potentially at risk globally. As of 2011, more than 95% of REE production came from China, even though there are significant reserves worldwide.[1] Given the limited sources of REE production and the increasing demand for these metals around the world, it is crucial to explore new REE feedstocks and to develop new and improved methods of REE extraction.[1-5]

Biosorption has gained interest in recent years as a potential clean, sustainable method for REE recovery. The high binding affinity of native cell surfaces for REEs relative to most non-REEs permits selective extraction of these valuable metals from low-grade feedstocks.[4, 6-8] Microbes are relatively inexpensive to produce in large quantities, and native biomass has a naturally high capacity for REE adsorption.[4, 9-13] Cell surfaces can withstand multiple cycles of adsorption and desorption, enabling reuse of biomass.[14] Furthermore, biosorption processes are not expected to contribute hazardous chemical wastes to a REE extraction scheme, unlike some conventional methods such as solvent extraction.[15, 16] Microbial surface adsorption could present a clean and effective means of REE recovery from a variety of feedstocks, including those that are low-grade and traditionally unexploited.

We have previously bioengineered *Escherichia coli* to express lanthanide binding tags (LBTs) on the cell surface to enhance their natural adsorptive properties, improving both extraction efficiency and selectivity for REEs.[17] LBT display increased REE adsorption capacity from ~13 to ~28 mg Tb / g dry cell weight in a simple buffer solution and also improved REE binding selectivity 2 to 10-fold over most non-REE metals present in mine tailing leachates.[17] The native cell surface functional groups, primarily carboxylate and phosphate,[18-21] do continue to play a major role in REE recovery with the LBT-displayed cells. In this study, we investigate the REE adsorption performance of the engineered LBT-displayed strain of *E. coli* under various geochemical conditions characteristic of geofluids.

Geothermal fluids are abundant, low-grade feedstocks that are currently being investigated as a potential source of REEs.[4, 6, 22, 23] Total REE concentrations reported in geofluids range from sub-ppb to low-ppm levels.[24] Fluids with REE concentrations at ppb levels or higher are nearly always acidic (pH <3.5), likely due to increased metal leaching at lower pH.[22, 24] Optimal REE biosorption typically occurs at pH ~6 and decreases with pH; therefore, pH adjustment may be required for the acidic, REE-rich feedstocks.[14, 25, 26] The temperature of geofluids varies greatly, and previous studies have demonstrated that temperatures as high as 80°C can lead to increased REE adsorption onto organic surfaces.[26-28] Total dissolved solids (TDS) in geofluids can be as high as hundreds of thousands of ppm, several orders of magnitude higher than the REEs.[24] The major contributors to TDS, such as Na and Mg, have low affinities for cell surface binding sites compared to the REEs but are present at such high concentrations that they may still be competitive. In addition, some metals, such as U and Pb, although present at much lower concentrations, are likely competitive because they have high affinities for the relevant surface sites.[17]

Although they have relatively low REE concentrations, geofluids are abundant and have the advantage of requiring minimal pretreatment prior to REE extraction, unlike solid feedstocks such as ion adsorption clays, where chemical leaching is generally required.[17, 23, 30] The geochemical characteristics of geofluids, such as elevated temperature, non-optimal pH, and high TDS can have a major impact on REE biosorption. Herein, we systematically examined the effects of these factors on REE extraction efficiency and purity. Results define the geochemical conditions that are amenable to REE biosorption, information that is key to the future development of a high-performance biosorption technology for REE recovery from geofluids.

## Methods

### *Bacterial strains and growth conditions*

The *E. coli* strain harboring a *lpp-ompA*-dLBT expression plasmid was grown in LB media supplemented with 50 µg/mL ampicillin. Expression of lpp-ompA-dLBT was induced at mid-exponential phase using 0.002% arabinose for 3 h at 37 °C. For a full description of plasmid construction and LBT expression see Park et al. (2016) and (2017).[14, 17] Cells were harvested, washed once in 10 mM MES (2-(N-morpholino)-ethanesulfonic acid) pH 6, normalized by $OD_{600}$, and used in biosorption experiments.

### *Blue Mountain geofluid REE biosorption*

A natural geofluid (pH = ~6) from the Blue Mountain geothermal area (BMG, Table 1) was obtained from AltaRock Energy Inc (WA, USA). Since the REE concentrations in BMG are <10 ppt, Tb was spiked in at 10 ppb. Cell density was set at $\sim 1 \times 10^8$ cells/ml. After 30 min incubation with the BMG, cells were separated by centrifugation at 20,000 x *g* for 5 min. Cells were washed once in 10 mM MES (pH 6) and resuspended in an equal volume of 5 mM citrate (pH 6) for 60 min for metal desorption. The supernatant was collected for analysis following centrifugation at 20,000 x *g* for 8 min.

*REE biosorption with the Great Salt Lake brine*

To test the effects of TDS and pH on REE biosorption, we used a synthetic geofluid that resembles the Great Salt Lake brine (GSL), but 2x more concentrated (Table 1). For the TDS experiment, aliquots of this GSL solution were diluted 3-, 10-, 100-, and 1000-fold using 10 mM MES buffer (pH 6). Tb concentration was set at 100 ppb and cell density at ~$1\times10^8$ cells/ml. Cells were incubated in the spiked brine solutions for 30 min prior to separation via centrifugation at 20,000 x *g* for 15 min. Then, the cells were washed in 10 mM MES (pH 6) and resuspended in an equal volume of 5 mM citrate pH 6 for 60 min for desorption. The supernatant was collected following centrifugation at 20,000 x *g* for 5 min. Control experiments with no cells revealed <2% Tb extraction at all TDS conditions.

For the pH experiment, the synthetic GSL solution, diluted 2-fold, was spiked to a final Tb concentration of ~16 ppm and adjusted to an initial pH of 2-6 using 10 M NaOH. The cells (~$1\times10^9$ cells/ml) were pelleted at 6000 x *g* for 5 min and resuspended in the respective pH-adjusted GSL feedstock. Following a 30 min incubation, aliquots of the cell suspension was transferred to cellulose acetate centrifuge tube filters (Costar) and spun at 6000 x *g* for 5 min to collect the cells. The cells on the filters were then washed in 10 mM MES (pH 6) and exposed to an equal volume of 5 mM citrate for 60 min for desorption. The cellulose acetate filters extracted <4% Tb at all tested conditions.

*Temperature dependence*

The GSL solution was diluted 2-fold and adjusted to pH 6 using 10 mM MES buffer (pH 6). Tb was added to ~48 ppm and cell density was set at ~$1x10^9$ cells/ml. The cells were incubated in the brine for 25 min at 24°C, 40°C, or 70°C. Cells were collected, washed, and the metals were desorbed with 5 mM citrate (pH 6) at room temperature using the centrifuge tube filters as described above. Two additional experiments were conducted in the low-TDS 10 mM MES buffer (pH 6). First, cells (~$1x10^9$ cells/ml) were exposed to UV radiation or heated to 70°C and cooled back to room temperature before being exposed to ~48 ppm Tb. Second, cells (~$1x10^9$ cells/ml) were exposed to solutions containing ~48 ppm of an individual metal (Tb, Cu, Mg, K, or Ca) at a range of temperatures from 24°C to 70°C.

*Metal competition experiments*

Metal competition experiments were conducted in 10 mM MES buffer (pH 6) by mixing a fixed concentration of Tb (~8 ppm) with different concentrations of the competing metals, including up to 5000 μM copper (Cu), 300 μM aluminum (Al), 500 μM lead (Pb), 1000 μM uranium (U), 100 μM thorium (Th), 250 mM magnesium (Mg), or 2000 mM sodium (Na). The range of metal concentrations was selected based on concentrations commonly found in geofluids (Table 1).[24] Cell density was set at ~$1x10^9$ cells/ml and the adsorption assay was conducted using the centrifugation method as described above.

*ICP-MS analysis*

GSL sample analyses were performed using a Thermo XSeriesII ICP-MS run in standard mode at UC Santa Cruz. The sample introduction system was an ESI PFA-ST nebulizer pumped at 120 μl/min. BMG sample analyses were conducted at Duke University on an Agilent 7900 ICP-MS run in either hydrogen (Ca) or helium gas modes.

*Thermodynamic analysis*

The cell surface complexation thermodynamics of REEs can be described by a linear free energy relationship (LFER) that relates aqueous metal-acetate stability constants to calculated metal-bacterial stability constants.[33] Temperature dependent metal-bacteria stability constants are not available for the majority of metals, so we use available data for Zn(II), Cd(II), and Pb(II) complexation with acetate[34] and *Penicillium simplicissimum*[35] at 20, 30, and 40°C to calibrate T-dependent LFERs (Figure S1). These LFERs maintain high linear correlation coefficients (0.992-0.999) within this temperature range (Figure S1). La-acetate,[36] Na-acetate,[37] Cu-acetate,[34] and $UO_2$-acetate[38] stability constants were input into each LFER to obtain approximate values for the corresponding metal-bacteria stability constants (Figure S1). We restrict our analysis to between 20 and 40°C because metal-bacterial stability constants are not yet available for higher temperatures.

Heats of reaction were evaluated using Van't Hoff plots, which relate thermodynamic stability constants to reaction free energies based on the relationship,

$$\ln K = \frac{-\Delta G}{RT} = \frac{\Delta S}{R} - \frac{\Delta H}{R}\left(\frac{1}{T}\right),$$

where $\Delta G$ is the Gibbs free energy of reaction, $\Delta S$ is the change in entropy, $\Delta H$ is the change in enthalpy, R is the gas constant, and T is temperature in °K.

## Results and Discussion

*REE recovery from the Blue Mountain geothermal fluid*

The low REE concentrations present in most geofluids are a major potential obstacle to economic recovery of REEs from these feedstocks. A natural solution (BMG, pH ~6) from the Blue Mountain geothermal area in Nevada, USA (Table 1) was selected to test the performance of REE biosorption from geofluids with low REE contents. Because the natural REE concentrations in the BMG are <10 ppt, we spiked the solution with a low concentration (10 ppb) of Tb, a REE of high criticality. Given the low REE concentration, a relatively low cell density (~1x$10^8$ cells/ml) was used. The results reported here and throughout this study describe the metals recovered during a single adsorption/desorption cycle. Since 5 mM citrate is known to enable complete elution of adsorbed REEs,[14] the extraction efficiencies and purities are controlled by adsorption rather than desorption behavior.

| | **Total REEs (ppb)** | **Na (ppm)** | **Mg (ppm)** | **K (ppm)** | **Ca (ppm)** | **Cu (ppb)** | **Pb (ppb)** | **U (ppb)** | **Th (ppt)** | **Al (ppb)** | **pH** |
|---|---|---|---|---|---|---|---|---|---|---|---|
| *Sangan Thermal Spring, Iran*[59] | 3166 | 882 | 152 | 477 | 752 | n/a | n/a | n/a | n/a | 2420 | 1.2 |
| *Obuki Hot Spring, Japan*[60] | 220.4 | 34 | 32.8 | 31 | 104 | n/a | n/a | n/a | n/a | 95 | 1.35 |
| *Dagunguo Spring, China*[61] | 87.694 | 1823 | 0.07 | 744.9 | 1.26 | 1.16 | 3.13 | 0.19 | 0.21 | 0.16752 | 8.27 |
| *Valles Caldera, USA*[62] | 338.98 | 12.2 | n/a | 81 | 115 | n/a | n/a | n/a | n/a | 170 | 1.33 |
| *Salton Sea, USA*[62] | 1.3218 | 60500 | n/a | 18800 | 31100 | n/a | n/a | n/a | n/a | bd | 5.70 |
| *Blue Mountain Geofluid, USA* | bd | 1370 | 2.06 | 150 | 21.6 | 0.25 | bd | bd | bd | 105 | 6.15 |
| *Great Salt Lake, USA* | 0.3904 | 25665 | 2585 | 2051 | 162 | n/a | n/a | 5.835 | 6.595 | 164 | 7.92 |

**Table 1:** Chemical composition of several geofluids. Data not available is reported as 'n/a', and below detection limit is reported as 'bd'.

LBT-displayed *E. coli* cells[31] extracted ~76% of the available Tb from the spiked BMG (Figure 1a), and extracted <1% of the Na, Li, and Rb and none of the K, Ca, As, Cs, Ba, or W, whose concentrations in the eluent were below the instrumental detection limits (Figure 1a, Table S1). Among the non-REEs, the biosorption process resulted in >1% extraction for only a few elements, Fe (~29%), Mg (~5%), Mn (~9%), and Sr (~2%) (Figure 1, Table S1). Compared to the feedstock prior to adsorption, the Tb purity in the eluent increased by >100-fold. The purity is defined as the molar ratio of the target metal relative to the total concentration of Na, Mg, K, Ca, and Tb, which approximates the total metals present. The few non-REE metals that showed an increase in purity were Fe (~40-fold), Mg (~10-fold), Mn (~10-fold), and Sr (~3-

fold), largely due to the more effective removal of other metal ions (Figure 1b). These data demonstrate effective and selective recovery of low concentrations of REEs from a complex geofluid matrix. Next, we describe a systematic investigation into the effects of several geochemical variables on REE recovery.

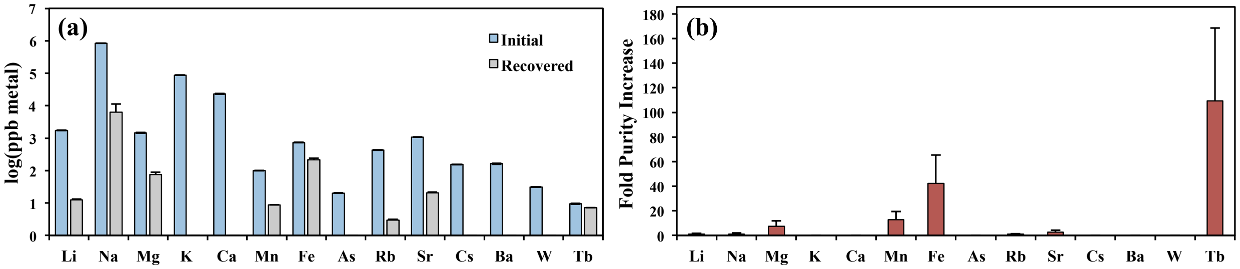

**Figure 1:** (a) Metal concentrations of the initial REE-spiked Blue Mountain geofluid (blue) and the recovered eluent after biosorption (grey). (b) Fold purity increase for each metal, which is defined for metal x relative to total metals as $(x_{eluent}/Total_{eluent})/(x_{feedstock}/Total_{feedstock})$. The initial Tb concentration was 10 ppb and cell concentration was ~1.2x$10^8$ cells/ml. The error bars represent the standard deviations of biological triplicates.

*Effects of high TDS*

The high ratio of total dissolved solids (TDS) to REEs, which in some cases can be on the order of 100,000:1, is a major potential challenge facing efficient recovery of REEs from geofluids.[24] To test the effects of TDS on REE adsorption, we performed REE recovery experiments with a synthetic Great Salt Lake brine (GSL, ~165,000 ppm TDS) that was used either at full strength or diluted 3-, 10-, 100-, and 1000-fold, covering a wide TDS range relevant to geofluids (Table 1). Tb was added to a final concentration of 100 ppb, which falls on the high end of REE concentrations in natural geofluids (Table 1).[24] Cell density was maintained at ~1.2x$10^8$ cells/ml to ensure an excess of surface sites for REE adsorption.

REE recovery by the LBT-displayed cells was largely unaffected by TDS under these experimental conditions. At low TDS conditions (~5.4 ppm), the LBT-displayed cells extracted ~81.5 ± 4.8% of the available Tb (Figure 2). A slight increase in Tb recovery was observed at elevated TDS, with ~95.1 ± 5.6% Tb extracted in the concentrated GSL brine (~165,000 ppm;

Figure 2). Na, K, and Ca were not extracted from the initial feedstock, although some Na was contributed by the sodium citrate eluent (Table S2). A small amount Mg was extracted across the tested TDS range (Table S2). The observed strong cell surface preference for REEs over the major non-REEs in the GSL brine is consistent with previous studies with other feedstock types, demonstrating the efficacy of biosorption for REE recovery from complex feedstocks.[10, 12, 39]

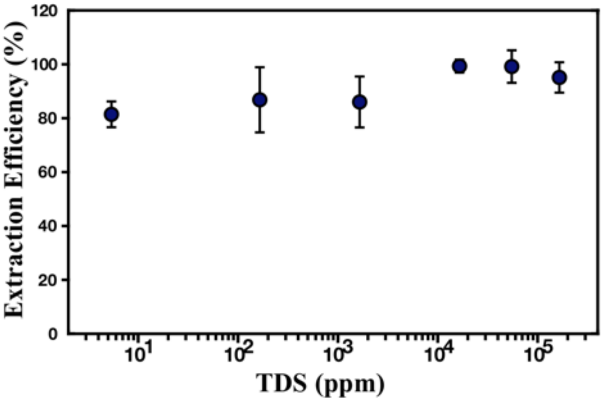

**Figure 2:** (a) REE adsorption efficiency by LBT-displayed *E. coli* at different total dissolved solid (TDS) concentrations. GSL solution was used at full strength (~165,000 ppm) or diluted 3-, 10-, 100-, 1000-fold. The low salt solution (10 mM MES buffer pH 6, ~5.4 ppm) was included for comparison. The initial Tb concentration was 100 ppb and cell concentration was ~$1.2\text{x}10^8$ cells/ml. The error bars represent the standard deviations of biological triplicates.

Previous reports have found that high TDS can have variable effects on metal adsorption onto a variety of surfaces. Increasing TDS may decrease REE adsorption onto mineral surfaces, likely due to competition effects from low affinity cations present at high concentrations.[40, 41] High TDS is also expected to increase surface charge, weakening the electrostatic attraction between the surface and aqueous metals and decreasing adsorption.[42-44] However, other studies have observed that changes in ionic strength do not affect REE adsorption onto surfaces including chelating polysaccharides,[45] clays,[46] and mesoporous silica.[47] It has been suggested that this REE adsorption is dominated by inner sphere complexation at high affinity sites rather than outer sphere complexation; therefore, the REEs cannot be easily displaced by low affinity ions that constitute the majority of the TDS.[47] Based on our findings, at circumneutral pH, the TDS levels typical of geofluids do not strongly affect REE extraction by LBT-displayed *E. coli*.

*Effects of competing metals*

In addition to high TDS, which is primarily contributed by a few major elements present at high concentrations, REE extraction efficiency may also be affected by the presence of low concentration metals with a high affinity for the cell surface. Previous experiments with mine tailing leachates identified certain metals, such as Cu, Al, and Pb, that are adsorbed onto the LBT-displayed cell surface alongside the REEs.[17] In addition, uranium and thorium are cogenetic elements during rare earth mineralization and are thus commonly found in REE-bearing minerals.[48, 49] These five metals (Cu, Al, Pb, U, and Th) were selected for analysis in a series of competition experiments. Sodium (Na) and magnesium (Mg) were also included for comparison, given their abundance in geofluids.

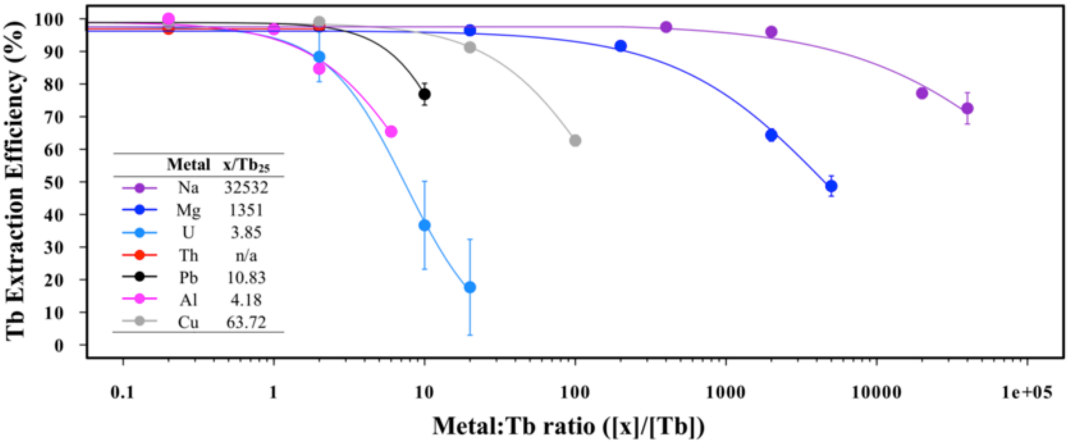

**Figure 3:** The fraction of terbium (Tb) adsorbed in the presence of a competing metal in buffer solution (10 mM MES pH 6). Initial Tb concentration was fixed at ~8 ppm and cell concentration was fixed at ~$1.2 \times 10^9$ cells/ml. The data for each competing metal was fit by a three-parameter log-logistic function using the drc (dose response curve) package in R. [x]/[Tb] represents the ratio of the concentration of the competing metal to that of Tb and x/Tb$_{25}$ refers to the value at which Tb adsorption decreases by 25% from that observed in the absence of any competing metal. The error bars represent the standard deviations of biological triplicates.

In these two-element competition experiments, a fixed concentration of Tb (~8 ppm) was mixed with varying concentrations of an individual competing metal and the amount of Tb adsorbed was compared to conditions without the competing metal. The data for each competition experiment was fit by a three-parameter log-logistic function to approximate the competing metal to Tb concentration ratio ($x/Tb_{25}$) at which Tb adsorption is decreased by 25% (Figure 3). We found that U and Al were the most competitive, with $x/Tb_{25}$ values of 3.85 and 4.81, respectively. Pb and Cu were less competitive, with $x/Tb_{25}$ values of 10.83 and 63.72, respectively. In contrast, Na ($x/Tb_{25}$ = 32,532) and Mg ($x/Tb_{25}$ = 1351) were much less competitive. Tb adsorption was not affected by Th at the tested concentrations, which cover the range found in most geofluids (Table 1).

The mechanism by which competitive metals displace REEs during adsorption is likely distinct from that of major electrolyte ions (e.g., TDS) because these competitive metals have similar affinities for the same cell surface sites as the REEs. Using the known LFER relating metal-acetate and metal-bacteria stability constants shown (Figure S1), we found that the stability constant for cell surface complexation at 20°C for La, a model REE, is similar in magnitude to that of U(VI), ~10-40% higher than for Pb and Cu, and >1300% higher than for Na. When ranked in order of decreasing metal competitiveness for bacterial surface sites, La(III) ≈ U(VI) > Pb(II) > Cu(II) >> Na(I). These results illustrate that the influence of Na and other weakly adsorbing metals, which constitute the majority of TDS, is clearly distinguishable from the effect of specifically competitive metals.

*Effects of pH*

The geofluids with higher total REE concentrations (e.g., >100 ppb) are typically acidic (pH <3.5), so a biosorbent that can function at lower pH is advantageous.[24] To test the effect of pH on REE biosorption, we conducted a series of Tb adsorption experiments with the GSL brine adjusted to an initial pH between 2 and 6. Higher pH conditions were not tested due to limited

REE solubility.[7, 14, 25, 50, 51] Tb was added in excess to avoid undersaturation of cell surface binding sites. We observed an increase in Tb extraction efficiency with increasing pH, peaking at ~36.9 ± 10.3% at pH 6, and dropping to ~12.5 ± 1.3% at pH 2 (Figure 4). As in the TDS experiments, the concentrations of major elements (Na, Mg, K, and Ca) in the eluent are generally <2% of those present in the initial GSL brine across the tested pH range (Figure 4). At pH 6, there was a ~20-fold increase in REE purity in the eluent compared to the initial feedstock, which dropped to ~9-fold at pH 2 due to a decrease in Tb adsorption.

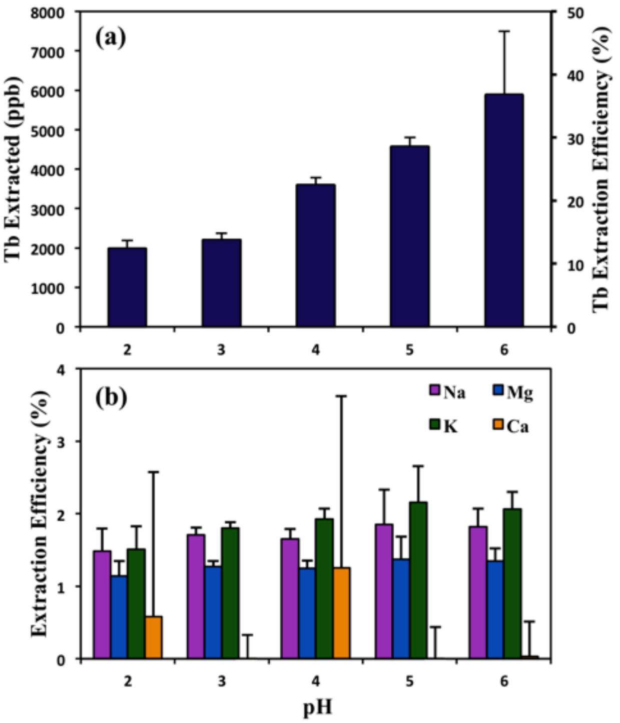

**Figure 4:** (a) REE biosorption performance from the GSL brine at pH 2-6. Initial Tb concentration was fixed at ~16 ppm and cell concentration at ~1.2x$10^9$ cells/ml. Less than 4% Tb extraction was observed for abiotic controls at all tested pH conditions. (b) Extraction efficiency of major metals is <3% and shows no significant change over pH 2-6. The error bars represent the standard deviations of biological triplicates.

Likely factors contributing to suppressed REE adsorption at lower pH include the protonation of cell surface binding sites and an increase in overall cell surface charge. The primary native cell surface functional groups involved in REE adsorption are carboxyl (pKa, 4.3 and 5.5) and phosphoryl (pKa, 2.2 and 6.9).[18-21] At low <4, phosphoryl ligands are expected to exert a dominant control on REE adsorption, and carboxyl ligands play a larger role as pH increases[55] which is reflected in the REE adsorption data in which adsorption decreases with pH, especially below pH 4. Consistent with previous studies,[50-54] we conclude that the optimal REE adsorption by the LBT-displayed strain of *E. coli* occurs at pH 5-6.

*Effects of temperature*

Since geothermal fluids range from ambient temperatures to >300°C, we examined REE extraction efficiency as a function of temperature. A series of adsorption experiments with the synthetic GSL brine were conducted at 24, 40, and 70°C. A high Tb concentration (~48 ppm) was set to exceed the apparent adsorption capacity of the cells at room temperature. Although cells are no longer viable at 70°C, they appear to remain structurally intact as examined via light microscopy (Figure S2). While there was minimal change in Tb adsorption from 24 to 40°C in the high TDS GSL brine, REE adsorption nearly tripled (~2.9-fold) from 40 to 70°C (Figure 5a). Further temperature increase to 100°C did not yield additional improvement in extraction efficiency (Figure S3). The increase in purity improved from ~15-fold at 24°C to ~60-fold at 70°C. Less than 1% of the major elements were recovered at all tested temperatures (Figure 5b). The increase in the extraction efficiency of REEs but not major elements suggests that a biosorption operation at elevated temperatures (e.g., 70°C) can improve REE extraction efficiency without compromising REE purity. We performed a series of experiments and constructed a theoretical model to better understand this intriguing REE biosorption behavior at elevated temperatures.

To determine if the temperature dependence of Tb adsorption was impacted by the high TDS in the GSL brine or was an innate feature of the cell surface, we conducted mono-element biosorption experiments in the low TDS buffer solution (10 mM MES pH 6) at 24, 40, and 70°C. Tb adsorption in MES buffer exhibited an approximately linear increase in extraction efficiency with increasing temperature, with a smaller increase (~1.6-fold) compared to the GSL brine (~2.9-fold) from 24 to 70°C (Figure 5c). Prior studies have similarly revealed that temperature dependence of Mg and Ca adsorption onto mineral surfaces was variably affected by ionic strength.[56, 57] Major element (Mg, K, Ca) adsorption in the buffer solution exhibited no systematic change with temperature (Figure 5c); Na was not tested due to the non-negligible Na present in MES. The increased Tb extraction efficiency and selectivity with increasing temperature is therefore not likely controlled by aqueous speciation in the GSL feedstock, but rather is characteristic of the cell surface.

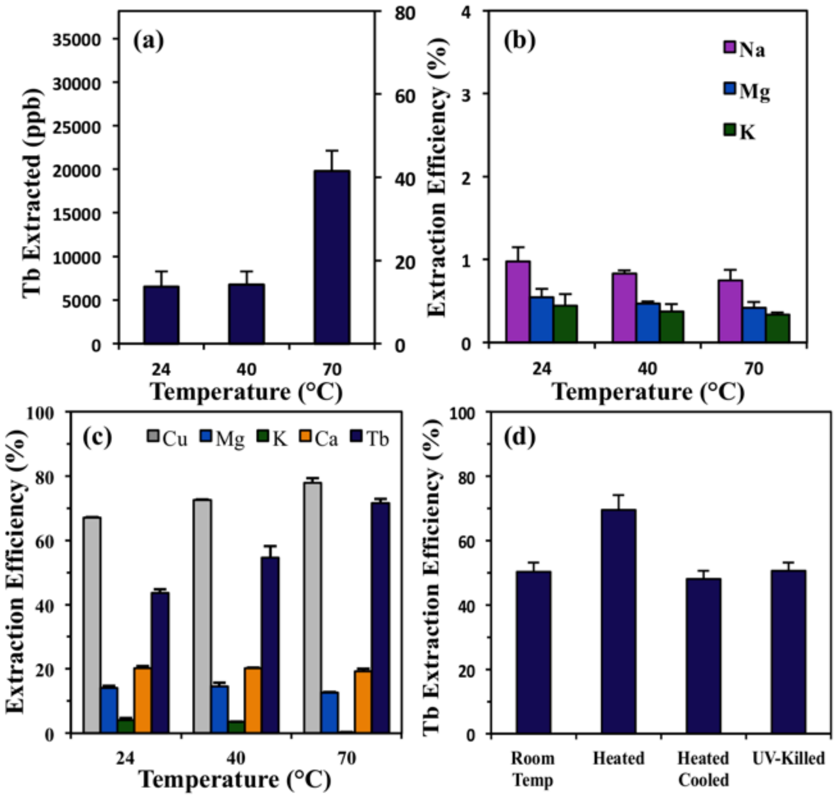

**Figure 5:** (a) REEs extracted (ppb) and extraction efficiency (%) as a function of temperature from 24-70°C. The initial Tb concentration was ~48 ppm and the cell concentration was ~1.2x10$^{9}$ cells/ml. Less than 3% Tb extraction was observed for abiotic controls at all temperatures. (b) Extraction efficiency (%) remains <2% for the major metals at all tested temperatures. (c) Tb, Cu, Mg, K, and Ca extraction efficiencies as a function of temperature from 24-70°C in 10 mM MES pH 6. (d) Comparison of Tb extraction efficiency in buffer solution at room temperature (24°C), heated (70°C), heated to 70°C then cooled to 24°C before Tb exposure, and UV-killed cells at 24°C. The error bars represent the standard deviations of biological triplicates.

To examine whether the temperature dependence of REE adsorption is caused by a temporary, reversible change in adsorption behavior or a permanent change in cell envelope structure, we analyzed the REE extraction efficiency of cells that were heated to 70°C then cooled to 24°C prior to REE exposure. These cells exhibited the same extraction efficiency as unheated cells, indicating that the increased Tb adsorption at elevated temperatures is reversible (Figure 5d). Moreover, UV-killed cells exhibited the same Tb extraction efficiency as live cells, suggesting that cell vitality has no effect on REE adsorption (Figure 5d). A change in adsorption kinetics is also unlikely to explain the temperature dependence since maximum adsorption occurs within 5 min at room temperature (Table S3), and the incubation time of 25 min ensured that equilibrium was reached for all experiments. Together, these observations provide strong evidence that the observed increase in REE extraction efficiency and selectivity with increasing temperature likely results from innate thermodynamic properties of the cell surface functional groups.

### *Thermodynamic analysis of temperature-dependent biosorption*

Changes in temperature have been shown to directly impact the thermodynamics of metal complexation by surface ligands. For example, complexation of many metals by carboxylate complexes on biological surfaces tends to be endothermic, resulting in enhanced metal adsorption at higher temperatures.[58] This behavior has been attributed to a reversible increase in the enthalpy of REE inner sphere complexation with cell surface functional groups.[26-28]

Fein et al. (2001) constructed a linear free energy relationship (LFER) at ambient temperature to relate metal-acetate and metal-*Bacillus subtilis* complexation stability constants, reporting a high 0.97 linear correlation coefficient for numerous metals including neodymium (Nd). The stability of aqueous REE-acetate complexes is known to increase with temperature,[34] but the corresponding REE-bacteria stability constants are unknown at elevated temperatures. We developed a series of temperature-dependent LFERs based on available metal-bacteria stability constants for *Penicillium simplicissimum* biosorption of Zn(II), Cd(II), and Pb(II) at 24, 30, and 40°C. The slopes of these LFERs steepen with increasing temperature, indicating that metal-bacteria stability constants increase more quickly with temperature than the corresponding metal-acetate stability constants (Figure S1).[35] A Van't Hoff plot for aqueous REE-acetate complexation stability constants was constructed using thermodynamic data from Ding and Wood (2002) (Figure 6a).[36] The slope of the Van't Hoff plot gives a positive $\Delta H_{\text{La-Acetate}}$ of 24.8 kJ/mol, indicating an endothermic reaction. Based on the temperature dependence of calculated LFERs, the slope of the REE-bacteria Van't Hoff plot is expected to be steeper (*i.e.,* more negative) than its corresponding REE-acetate plot (Figure 6a), which strongly suggests that REE-bacterial surface complexation reactions are even more endothermic. We conclude that the strong positive temperature dependence of REE biosorption is likely controlled by the increased REE affinity for carboxylate functional groups on the cell surface.

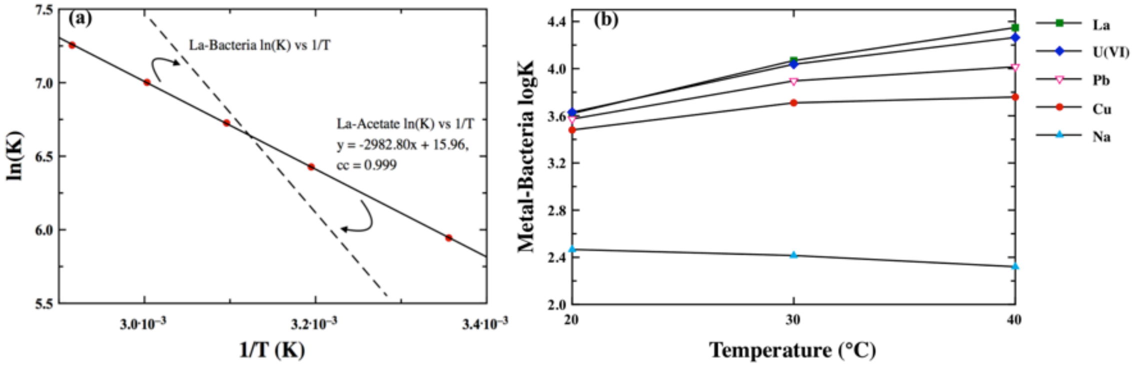

**Figure 6:** (a) Van't Hoff plots of lanthanum-acetate and projected lanthanum-bacteria complexation. The lanthanum-bacteria ln(K) vs 1/T plot is a qualitative dashed line indicating a steeper negative slope than lanthanum-acetate given that the lanthanum-bacteria stability constant is higher than its lanthanum-acetate counterpart at elevated temperatures. (b) Metal-bacteria stability constants (logK) as a function of temperature. Stability constants for La, U(VI), Cu, and Na (closed symbols) were calculated based on a temperature-dependent linear free energy relationship (Figure S1) generated from Zn, Cd, and Pb-acetate[34] and bacteria (open symbol) stability constant data.[35]

The same LFER analysis can be used to evaluate the influence of temperature on bacterial surface selectivity for various metals. At higher temperatures, La-bacteria stability constants increase more dramatically than those of the competitive metals included for comparison (Na, Zn, Cd, Cu, and Pb, Figure 6b). Thus, increasing temperature is expected to cause both increased REE adsorption and increased surface selectivity for the REEs. The apparent increase in surface selectivity for REEs with respect to the competitive metals in the GSL brine can be explained by the proportionally greater increase in REE-surface site affinity compared with non-REEs with increasing temperature, as indicated in Figure 6b. Based on the good agreement between the experimental data and the theoretical thermodynamic behavior, we conclude that the observed increase in Tb adsorption with increasing temperature is likely a thermodynamic effect, although reversible, temperature-mediated changes to the cell surface cannot be conclusively ruled out.

*Implications for REE extraction*

Given its high REE recovery efficiency and selectivity, biosorption with LBT-displayed *E. coli* shows promise for REE recovery from geofluids. In the overall REE recovery process (Figure 7), the first step would be preconditioning the geofluid to optimal conditions for biosorption (e.g., pH 5-6 and 70°C). As a result of the temperature and pH changes, the solubility of some competitive metals, particularly Al and Pb, will be limited. Therefore, the removal of precipitates prior to biosorption may help to eliminate these contaminants. Following preconditioning, selective biosorption will deliver an enriched and purified REE eluent, and the

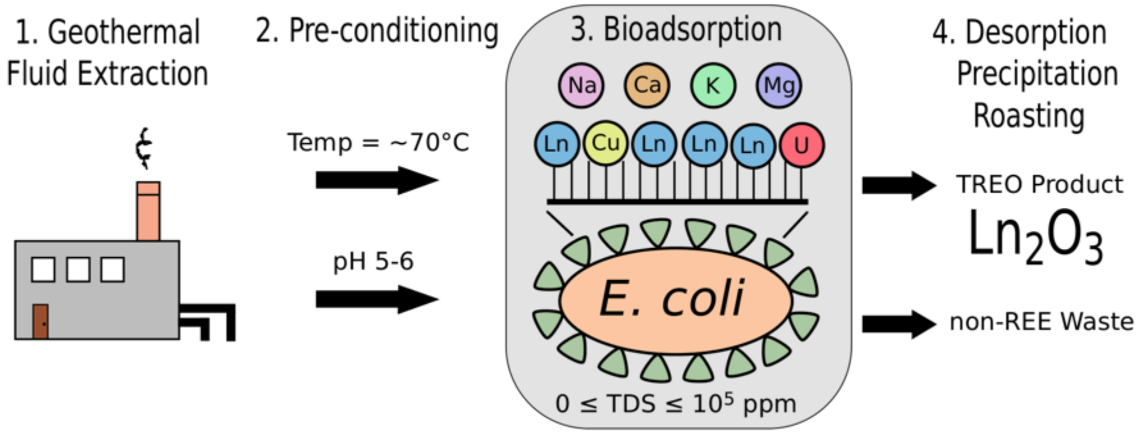

**Figure 7:** Schematic showing a process flow for integrating the LBT-displayed *E. coli* biosorption system for REE extraction from geofluids.

aqueous REEs are then precipitated as REE minerals by adding oxalate or carbonate. Unlike REEs, some metals, such as U and Th, will remain in solution during this precipitation step, improving REE purity.[15, 48] Finally, the REE precipitates are roasted to produce total rare earth oxides. These results demonstrate that biosorption using bioengineered microbes may be an effective platform for extracting REEs from geofluids and other non-traditional feedstocks. Overall, this study contributes to the development of innovative clean mining technologies.

## Acknowledgements

We thank Geoffrey Garrison at AltaRock for providing the Blue Mountain geothermal fluid and Hari Neupane at Idaho National Laboratory for providing the Great Salt Lake brine. This research is supported by the U.S. Department of Energy, Office of Energy Efficiency and Renewable Energy, Geothermal Office. AB acknowledges funding from the Livermore Graduate Scholar Program from Lawrence Livermore National Laboratory. This work was performed under the auspices of the U.S. Department of Energy by Lawrence Livermore National Laboratory under Contract DEAC52-07NA27344 (LLNL-TH-763869).

**Supporting Information.** Tables S1, metal concentration profile of the BMG before and after biosorption; Table S2, metal recovery from the GSL brine at different TDS; Table S3, Tb biosorption kinetics; Figure S1, modeled linear free energy relationship dependence on temperature for metal-cell surface and metal-acetate complexation; Figure S2, Live/Dead staining of heated and cooled cells; Figure S3, temperature dependence of REE recovery up to 100°C.

| Metal | Feedstock Concentration (ppb) | Eluent Concentration (ppb) | Extraction Efficiency (%) |
|---|---|---|---|
| Li | 1733 | 12 | 0.71 |
| Na | 838,392 | 6311 | 0.75 |
| Mg | 1448 | 76 | 5.25 |
| K | 87,874 | bd | 0.00 |
| Ca | 23,251 | bd | 0.00 |
| Mn | 99 | 9 | 8.81 |
| Fe | 737 | 216 | 29.30 |
| As | 20 | bd | 0.00 |
| Rb | 426 | 3 | 0.69 |
| Sr | 1068 | 21 | 1.93 |
| Cs | 155 | bd | 0.00 |
| Ba | 162 | bd | 0.00 |
| W | 31 | bd | 0.00 |
| Tb | 9.40 | 7.16 | 76.21 |

**Table S1:** Metal concentration profile of the initial Blue Mountain geothermal fluid (BMG) prior to biosorption and of the recovered eluent upon desorption with 5 mM citrate. Data below the detection limit are reported as 'bd'. The extraction efficiency is defined as the percent of a given metal recovered by one cycle of biosorption and elution.

| TDS (ppm) | Tb (ppb) | Na* (ppm) | Mg (ppm) |
|---|---|---|---|
| 165,000 | 63.0 ± 3.7 | 341.6 ± 3.2 | 2.2 ± 0.3 |
| 55,100 | 64.9 ± 3.9 | 339.1 ± 2.5 | 1.9 ± 0.2 |
| 16,500 | 66.1 ± 1.6 | 343.4 ± 6.2 | 1.3 ± 0.0 |
| 1,650 | 56.1 ± 6.2 | 343.1 ± 2.3 | 0.8 ± 0.1 |
| 165 | 56.3 ± 7.8 | 358.7 ± 1.2 | 1.6 ± 0.9 |
| 5.4 | 52.0 ± 3.1 | 370.0 ± 9.2 | 0.3 ± 0.1 |

**Table S2:** Tb, Na, and Mg extracted from the GSL solution at different TDS conditions. *Note that the Na concentration of the sodium citrate used for elution is ~369 ppm, so the Na present is not derived from the GSL feedstock but from the citrate desorbent.

| Time (min) | Tb Adsorbed (μM) |
|---|---|
| 5 | 41.36 ± 0.43 |
| 10 | 41.27 ± 0.78 |
| 20 | 42.20 ± 0.39 |
| 40 | 41.72 ± 0.83 |
| 90 | 41.60 ± 0.66 |

**Table S3:** Tb adsorption by the LBT-displayed *E. coli* in MES buffer (pH 6) over time. The initial Tb concentration was ~8 ppm (50 μM) and the cell concentration was ~1.2x$10^9$ cells/ml.

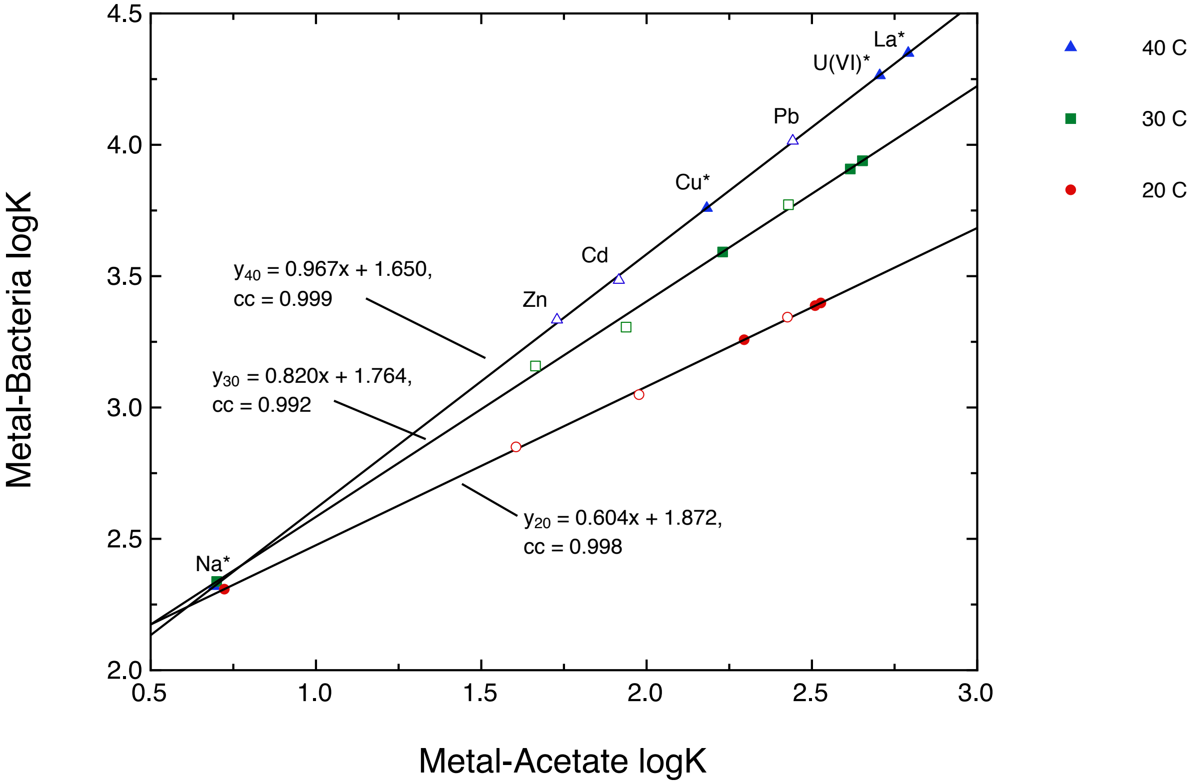

**Figure S1:** Linear free energy relationship dependence on temperature for Zn, Cd, and Pb. *Penicillium simplicissimum* was used to experimentally generate the metal-bacteria logKs for Zn, Cd, and Pb (open symbols).[1] La-acetate,[2] Na-acetate,[3] Cu-acetate,[4] and $UO_2$-acetate[5] stability constants were used in the computed linear free energy equations to obtain fitted La-, Na-, Cu- and U(VI)-bacteria Langmuir affinity logKs (closed symbols, asterisked metal names). Most notably, this figure illustrates that the linear free energy relationships become steeper in slope as temperature increases.

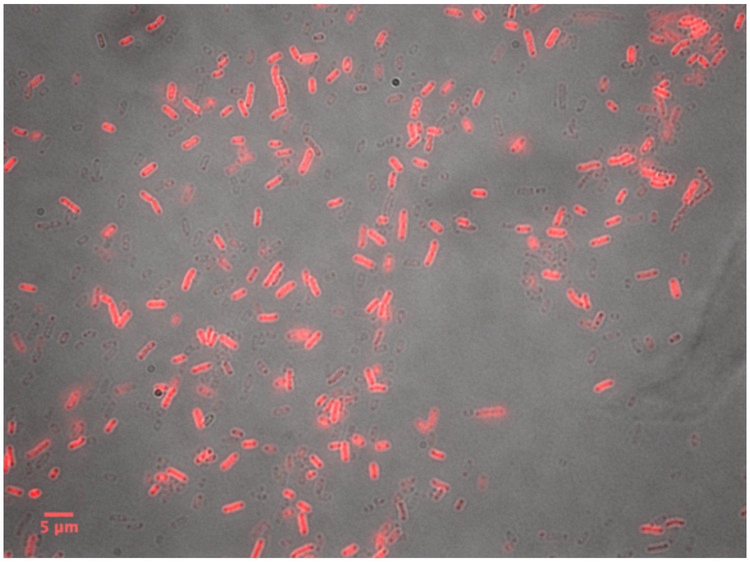

**Figure S2:** Propidium iodide staining of LBT-displayed *E. coli* cells that were heated to 70°C for 30 minutes and cooled back to room temperature before imaging. Composite of phase contrast and fluorescence images (490/635 nm) of dead cells stained with propidium iodide during a bacterial viability test (*Bac*Light$^{TM}$, ThermoFisher).

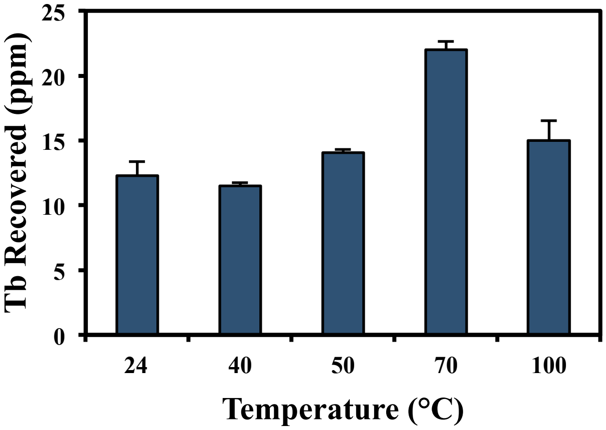

**Figure S3:** Tb recovery from the synthetic GSL brine. Initial Tb concentration was ~48 ppm (300 µM) and cell concentration were maintained at ~$1.2x10^9$ cells/ml. Note that temperatures above 70°C (i.e., 100°C) did not improve recovery efficiency.

## References

1. DOE, Critical Materials Strategy. In 2011.

2. Zhuang, W. Q.; Fitts, J. P.; Ajo-Franklin, C. M.; Maes, S.; Alvarez-Cohen, L.; Hennebel, T., Recovery of critical metals using biometallurgy. *Curr Opin Biotech* **2015,** *33*, 327-335.

3. Hennebel, T.; Boon, N.; Maes, S.; Lenz, M., Biotechnologies for critical raw material recovery from primary and secondary sources: R&D priorities and future perspectives. *New Biotechnol* **2015,** *32*, (1), 121-127.

4. Dodson, J. R.; Parker, H. L.; Garcia, A. M.; Hicken, A.; Asemave, K.; Farmer, T. J.; He, H.; Clark, J. H.; Hunt, A. J., Bio-derived materials as a green route for precious & critical metal recovery and re-use. *Green Chem* **2015,** *17*, (4), 1951-1965.

5. Eggert, R. W., C.; Anderson, C.; Bauer, D.; Fields, F.; Meinert, L.; Taylor, P., Rare Earths: Market disruption, innovation, and global supply chains. *Annu. Rev. Environ. Resour.* **2016,** *41*, 199-222.

6. Jacinto, J.; Henriques, B.; Duarte, A. C.; Vale, C.; Pereira, E., Removal and recovery of Critical Rare Elements from contaminated waters by living Gracilaria gracilis. *J Hazard Mater* **2018,** *344*, 531-538.

7. Kucuker, M. A.; Wieczorek, N.; Kuchta, K.; Copty, N. K., Biosorption of neodymium on Chlorella vulgaris in aqueous solution obtained from hard disk drive magnets. *PLoS One* **2017,** *12*, (4), e0175255.

8. Lo, Y. C.; Cheng, C. L.; Han, Y. L.; Chen, B. Y.; Chang, J. S., Recovery of high-value metals from geothermal sites by biosorption and bioaccumulation. *Bioresource Technol* **2014,** *160*, 182-190.

9. Jiang, M. Y.; Ohnuki, T.; Tanaka, K.; Kozai, N.; Kamiishi, E.; Utsunomiya, S., Post-adsorption process of Yb phosphate nano-particle formation by Saccharomyces cerevisiae. *Geochim Cosmochim Ac* **2012,** *93*, 30-46.

10. Moriwaki, H.; Yamamoto, H., Interactions of microorganisms with rare earth ions and their utilization for separation and environmental technology. *Appl Microbiol Biot* **2013,** *97*, (1), 1-8.

11. Ozaki, T.; Gillow, J. B.; Kimura, T.; Ohnuki, T.; Yoshida, Z.; Francis, A. J., Sorption behavior of europium(III) and curium(III) on the cell surfaces of microorganisms. *Radiochim Acta* **2004,** *92*, (9-11), 741-748.

12. Texier, A. C.; Andres, Y.; Le Cloirec, P., Selective biosorption of lanthanide (La, Eu, Yb) ions by Pseudomonas aeruginosa. *Environ Sci Technol* **1999,** *33*, (3), 489-495.

13. Tsuruta, T., Accumulation of rare earth elements in various microorganisms. *J Rare Earth* **2007,** *25*, (5), 526-532.

14. Park, D. M.; Reed, D. W.; Yung, M. C.; Eslamimanesh, A.; Lencka, M. M.; Anderko, A.; Fujita, Y.; Riman, R. E.; Navrotsky, A.; Jiao, Y. Q., Bioadsorption of Rare Earth Elements through Cell Surface Display of Lanthanide Binding Tags. *Environ Sci Technol* **2016,** *50*, (5), 2735-2742.

15. Nash, K. L.; Jensen, M. P., Analytical-scale separations of the lanthanides: A review of techniques and fundamentals. *Sep Sci Technol* **2001,** *36*, (5-6), 1257-1282.

16. Xie, F.; Zhang, T. A.; Dreisinger, D.; Doyle, F., A critical review on solvent extraction of rare earths from aqueous solutions. *Miner Eng* **2014,** *56*, 10-28.

17. Park, D. M.; Brewer, A.; Reed, D. W.; Lammers, L. N.; Jiao, Y., Recovery of Rare Earth Elements from Low-Grade Feedstock Leachates Using Engineered Bacteria. *Environ Sci Technol* **2017,** *51*, (22), 13471-13480.

18. Ngwenya, B. T.; Magennis, M.; Olive, V.; Mosselmans, J. F.; Ellam, R. M., Discrete site surface complexation constants for lanthanide adsorption to bacteria as determined by experiments and linear free energy relationships. *Environ Sci Technol* **2010,** *44*, (2), 650-6.

19. Martinez, R. E. P., O.; Takahashi, Y., Modeling rare earth element sorption to the Gram positive Bacillus subtilis bacteria surface. *J Colloid Interf Sci* **2014,** *413*, 106-111.

20. Markai, S. A., Y.; Montavon, G.; Grambow, B., Study of the interaction between europium (III) and Bacillus subtilis: fixation sites, biosorption modeling and reversibility. *J Colloid Interf Sci* **2003,** *262*, 351-361.

21. Texier, A. C. A., Y.; Illemassene, M.; Le Cloirec, P., Characterization of lanthanide ions binding sites in the cell wall of Pseudomonas aeruginosa. *Environ Sci Technol* **2000,** *34*, (4), 610-615.

22. Smith, Y. R.; Kumar, P.; McLennan, J. D., On the Extraction of Rare Earth Elements from Geothermal Brines. *Resources-Basel* **2017,** *6*, (3).

23. Jin, H. Y.; Park, D. M.; Gupta, M.; Brewer, A. W.; Ho, L.; Singer, S. L.; Bourcier, W. L.; Woods, S.; Reed, D. W.; Lammers, L. N.; Sutherland, J. W.; Jiao, Y. Q., Techno-economic Assessment for Integrating Biosorption into Rare Earth Recovery Process. *Acs Sustain Chem Eng* **2017,** *5*, (11), 10148-10155.

24. Wood, S. A., Behavior of rare earth elements in geothermal systems: A new exploration/exploitation tool? In DOE, Ed. Geothermal Reservoir Technology Research: 2001.

25. Bonificio, W. D.; Clarke, D. R., Rare-Earth Separation Using Bacteria. *Environ Sci Tech Let* **2016,** *3*, (4), 180-184.

26. Takahashi, Y.; Chatellier, X.; Hattori, K. H.; Kato, K.; Fortin, D., Adsorption of rare earth elements onto bacterial cell walls and its implication for REE sorption onto natural microbial mats. *Chem Geol* **2005,** *219*, (1-4), 53-67.

27. Smith, Y. R.; Bhattacharyya, D.; Willhard, T.; Misra, M., Adsorption of aqueous rare earth elements using carbon black derived from recycled tires. *Chem Eng J* **2016,** *296*, 102-111.

28. Xu, S. X.; Wang, Z. W.; Gao, Y. Q.; Zhang, S. M.; Wu, K., Adsorption of Rare Earths(III) Using an Efficient Sodium Alginate Hydrogel Cross-Linked with Poly-gamma-Glutamate. *Plos One* **2015,** *10*, (5).

29. Wood, S. A., Rare earth element systematics of acidic geothermal waters from the Taupo Volcanic Zone, New Zealand. *J Geochem Explor* **2006,** *89*, (1-3), 424-427.

30. Muravyov, M. I.; Bulaev, A. G.; Melamud, V. S.; Kondrat'eva, T. F., [Leaching of Rare Earth Elements from Coal Ashes Using Acidophilic Chemolithotrophic Microbial Communities]. *Mikrobiologiia* **2015,** *84*, (2), 216-24.

31. Martin, L. J.; Hahnke, M. J.; Nitz, M.; Wohnert, J.; Silvaggi, N. R.; Allen, K. N.; Schwalbe, H.; Imperiali, B., Double-lanthanide-binding tags: Design, photophysical properties, and NMR applications. *J Am Chem Soc* **2007,** *129*, (22), 7106-7113.

32. Wei, W.; Liu, X. Z.; Sun, P. Q.; Wang, X.; Zhu, H.; Hong, M.; Mao, Z. W.; Zhao, J., Simple Whole-Cell Biodetection and Bioremediation of Heavy Metals Based on an Engineered Lead-Specific Operon. *Environ Sci Technol* **2014,** *48*, (6), 3363-3371.

33. Fein, J. B.; Martin, A. M.; Wightman, P. G., Metal adsorption onto bacterial surfaces: Development of a predictive approach. *Geochim Cosmochim Ac* **2001,** *65*, (23), 4267-4273.

34. Shock, E. L. K., C. M., Metal-organic complexes in geochemical processes: Calculation of standard partial molal thermodynamic properties of aqueous acetate complexes at high pressures and temepratures. *Geochim Cosmochim Ac* **1993,** *57*, 4899-4922.

35. Fan, T.; Liu, Y.; Feng, B.; Zeng, G.; Yang, C.; Zhou, M.; Zhou, H.; Tan, Z.; Wang, X., Biosorption of cadmium(II), zinc(II) and lead(II) by Penicillium simplicissimum: Isotherms, kinetics and thermodynamics. *J Hazard Mater* **2008,** *160*, (2-3), 655-61.

36. Ding, R. W., S. A., The aqueous geochemistry of the rare earth elements and yttrium. Part X. Potentiometric determination of stability constants of acetate complexes of La3+, Nd3+, Gd3+, and Yb3+ at 25-70°C and 1 bar. In *Water-rock interactions, ore deposits, and environmental geochemistry: A tribute to David A. Crerar*, R. Hellmann, S. A. W., Ed. The Geochemical Society: 2002; pp 209-227.

37. Fournier, P.; Oelkers, E. H.; Gout, R.; Pokrovski, G., Experimental determination of aqueous sodium-acetate dissociation constants at temperatures from 20 to 240 degrees C. *Chem Geol* **1998,** *151*, (1-4), 69-84.

38. Jiang, J. R., L.; Di Bernardo, P.; Zanonato, P. L.; Bismondo, A., Complexation of uranium(VI) with acetate at variable temperatures. *Journal of the Chemical Society, Dalton Transactions* **2002**, (8), 1832-1838.

39. Ngwenya, B. T.; Mosselmans, J. F. W.; Magennis, M.; Atkinson, K. D.; Tourney, J.; Olive, V.; Ellam, R. M., Macroscopic and spectroscopic analysis of lanthanide adsorption to bacterial cells. *Geochim Cosmochim Ac* **2009,** *73*, (11), 3134-3147.

40. Tang, J. W.; Johannesson, K. H., Rare earth elements adsorption onto Carrizo sand: Influence of strong solution complexation. *Chem Geol* **2010,** *279*, (3-4), 120-133.

41. Munemoto, T.; Ohmori, K.; Iwatsuki, T., Rare earth elements (REE) in deep groundwater from granite and fracture-filling calcite in the Tono area, central Japan: Prediction of REE fractionation in paleo- to present-day groundwater. *Chem Geol* **2015,** *417*, 58-67.

42. Small, T. D.; Warren, L. A.; Ferris, F. G., Influence of ionic strength on strontium sorption to bacteria, Fe(III) oxide, and composite bacteria-Fe(III) oxide surfaces. *Appl Geochem* **2001,** *16*, (7-8), 939-946.

43. Borrok, D. M.; Fein, J. B., The impact of ionic strength on the adsorption of protons, Pb, Cd, and Sr onto the surfaces of Gram negative bacteria: testing non-electro static, diffuse, and triple-layer models. *J Colloid Interf Sci* **2005,** *286*, (1), 110-126.

44. Daughney, C. J.; Fein, J. B., The effect of ionic strength on the adsorption of H+, Cd2+, Pb2+, and Cu2+ by Bacillus subtilis and Bacillus licheniformis: A surface complexation model. *J Colloid Interf Sci* **1998,** *198*, (1), 53-77.

45. Elsalamouny, A. R.; Desouky, O. A.; Mohamed, S. A.; Galhoum, A. A.; Guibal, E., Uranium and neodymium biosorption using novel chelating polysaccharide. *Int J Biol Macromol* **2017,** *104*, (Pt A), 963-968.

46. Poetsch, M.; Lippold, H., Effects of ionic strength and fulvic acid on adsorption of Tb(III) and Eu(III) onto clay. *J Contam Hydrol* **2016,** *192*, 146-151.

47. Dolatyari, L. Y., M. R.; Rostamnia, S., Adsorption characteristics of Eu(III) and Th(IV) ions onto modified mesoporous silica SBA-15 materials. *Journal of the Taiwan Institute of Chemical Engineers* **2016,** *60*, 174-184.

48. Zhu, Z. P., Y.; Cheng, C. Y., Separation of uranium and thorium from rare earths for rare earth production - A review. *Miner Eng* **2015,** *77*, 185-196.

49. Mashkovtsev, M. B., M.; Smyshlyaev, D.; Pajarre, R.; Kangas, P.; Rychkov, V.; Koukkari, P., Pilot-scale recovery of rare earths and scandium from phosphogypsum and uranium leachates. *E3S Web of Conferences* **2016,** *8*, (01026).

50. Hosomomi, Y.; Wakabayashi, R.; Kubota, F.; Kamiya, N.; Goto, M., Diglycolic amic acid-modified E. coli as a biosorbent for the recovery of rare earth elements. *Biochem Eng J* **2016,** *113*, 102-106.

51. Vijayaraghavan, K.; Sathishkumar, M.; Balasubramanian, R., Interaction of rare earth elements with a brown marine alga in multi-component solutions. *Desalination* **2011,** *265*, (1-3), 54-59.

52. Mosbah, R.; Sahmoune, M. N., Biosorption of heavy metals by Streptomyces species - an overview. *Cent Eur J Chem* **2013,** *11*, (9), 1412-1422.

53. Pacheco, P. H.; Gil, R. A.; Cerutti, S. E.; Smichowski, P.; Martinez, L. D., Biosorption: A new rise for elemental solid phase extraction methods. *Talanta* **2011,** *85*, (5), 2290-2300.

54. Xu, S. X.; Zhang, S. M.; Chen, K.; Han, J. F.; Liu, H. S.; Wu, K., Biosorption of La3+ and Ce3+ by Agrobacterium sp HN1. *J Rare Earth* **2011,** *29*, (3), 265-270.

55. Takahashi, Y. Y., M.; Yamamoto, Y.; Tanaka, K., EXAFS study on the cause of enrichment of heavy REEs on bacterial surfaces. *Geochim Cosmochim Ac* **2010,** *74*, 5443-5462.

56. Ridley, M. K. M., M. L.; Wesolowski, D. J.; Palmer, D. A., Calcium adsorption at the rutile-water interface: A potentiometric study in NaCl media to 250C. *Geochim Cosmochim Ac* **1999,** *63*, 3087-3096.

57. Katz, L. E.; Criscenti, L. J.; Chen, C. C.; Larentzos, J. P.; Liljestrand, H. M., Temperature effects on alkaline earth metal ions adsorption on gibbsite: approaches from macroscopic sorption experiments and molecular dynamics simulations. *J Colloid Interface Sci* **2013,** *399*, 68-76.

58. Sag, Y. K., T., Determination of the biosorption heats of heavy metal ions on *Zoogloea ramigera* and *Rhizopus arrhizus*. *Biochem Eng J* **2000,** *6*, 145-151.

59. Shakeri, A.; Ghoreyshinia, S.; Mehrabi, B.; Delavari, M., Rare earth elements geochemistry in springs from Taftan geothermal area SE Iran. *J Volcanol Geoth Res* **2015,** *304*, 49-61.

60. Sanada, T.; Takamatsu, N.; Yoshiike, Y., Geochemical interpretation of long-term variations in rare earth element concentrations in acidic hot spring waters from the Tamagawa geothermal area, Japan. *Geothermics* **2006,** *35*, (2), 141-155.

61. Zhang, Y. T., H.; Zhang, W.; Wei, H.; Dong, T., Geochemical constraint on origin and evolution of solutes in geothermal springs in western Yunnan, China. *Chemie der Erde* **2016,** *76*, 63-75.

62. Michard, A., Rare earth element systematics in hydrothermal fluids. *Geochim Cosmochim Ac* **1989,** *53*, 745-750.

# CHAPTER 6: Selective recovery of rare earth elements from non-traditional feedstocks using bacteria immobilized in polymer microparticles

This chapter is in preparation for publication as:

*Brewer, A.B., Park, D.M., Ye, C.W., Wang, S., Li, Y., Reed, D., Lammers, L.N., Jiao, Y. (2018) Selective recovery of rare earth elements from non-traditional feedstocks using bacteria immobilized in polymer microparticles. ACS Applied Materials & Interfaces.*

## Abstract

Rare earth elements (REEs) are considered critical materials based on their importance to the modern economy and their potential supply vulnerability. This supply vulnerability motivates the development of new techniques to enable cost-effective REE recovery from non-traditional feedstocks. We have previously engineered *E. coli* to express lanthanide binding tags (LBTs) on the cell surface for selective recovery of REEs from feedstocks such as geothermal fluids. However, free-floating cells are generally not suitable for industrial-scale extraction operations, in part because they can limit fluid transport in continuous flow systems. Here we immobilize the engineered cells by encapsulating them in polyethylene glycol diacrylate (PEGDA) microparticles for use in fixed-bed columns for REE recovery and purification. We demonstrate that optimal REE recovery (~2.6 mg Nd/g dry sorbent) in these columns occurs at a flow rate of ≤1 ml/min with an influent pH of 6. The estimated maximum influent REE concentration is ~21 mM, so the microparticles are capable of extracting REEs from most non-traditional feedstocks when applied in a column system. The microparticles are reusable over >9 adsorption/desorption cycles, with minimal loss in REE recovery performance. Furthermore, the microparticles exhibit a strong preference for heavy REEs, particularly Eu, Sm, Yb, and Lu, compared to the light

REEs, which may permit the separation of individual REEs with an appropriate method design. The results of this study represent a major step towards transitioning engineered microbes from promising REE adsorbents to a practical, industrial scale REE extraction technology.

## Introduction

Rare earth elements (REEs) are critical components of many green energy technologies, such as wind turbines, and consumer products, including mobile phones, laptops, and appliances.[1] However, greater than >85% of the global REE supply is obtained from China, leaving the global market vulnerable to supply restrictions.[2] Given the lack of economically exploitable REE ore deposits in many locations, various abundant, non-traditional REE resources (e.g., geothermal fluids,[3] coal byproducts,[4, 5] and electronic wastes[6]) are currently being explored as potential REE feedstocks. The adverse chemical characteristics of many of these feedstocks relative to high-grade ores, including high concentrations of non-REE metals and low REE contents, present a significant challenge for industrial-scale exploitation using traditional extraction technologies. The development of new REE extraction methodologies that can effectively exploit these non-traditional feedstocks is thus important for diversifying the REE supply chain and reducing dependency on foreign imports.

Adsorption-based solid-phase extraction systems offer promise for extracting REEs from low-grade feedstocks. Many adsorbents have been tested,[7] including bioengineered microbes,[8-10] organic wastes such as seafood[11] and vegetable byproducts,[12] various hydrogels,[13] zero-valent iron particles,[14] and mineral powders.[15] Each of these materials has advantages and disadvantages for REE extraction. For example, organic wastes are inexpensive, abundant, and non-hazardous; however, they may not have the high selectivity for REEs that an engineered hydrogel will exhibit.[7] Zero-valent iron particles on the other hand, are highly adsorbent but degrade at some environmentally-relevant conditions.[14] An ideal adsorbent would exhibit both a high capacity and a high selectivity for REEs and be inexpensive, readily available, mechanically and chemically stable, and environmentally friendly.

Biosorption offers a sustainable method for REE extraction and purification that is well suited for non-traditional REE feedstocks. Native microbial surfaces typically have a high binding affinity for REEs compared to most non-REE metals, enabling REEs to be selectively concentrated on the cell surface relative to the aqueous phase.[16-19] Microbes are relatively inexpensive to produce in large quantities, exhibit fast adsorption and desorption kinetics, and can be reused over multiple REE recovery cycles.[8, 20-24] Furthermore, unlike solvent extraction, which is the current industrial standard for REE separation, biosorption processes would not contribute to the production of hazardous chemical wastes.[25, 26] Recent work from our group and others has revealed the potential utility of genetic engineering to enhance the already high REE binding capacity and selectivity of native microbial surfaces. Genetic alteration of teichoic acids, a major cell wall component of *Bacillus subtilis*,[27] and heterologous expression and display of lanthanide binding peptides on the surface of *Caulobacter crescentus*[8] and *E. coli*[9] has enhanced microbial REE adsorption capacity and selectivity. Although the adsorptive characteristics of these microbes are appropriate for selective REE extraction, there are several drawbacks to their use in industrial-scale applications in their native form, including a tendency to obstruct fluid flow, relatively low cell stability, and the risk of cells escaping into the feedstock.[28]

Immobilizing the cells, often by imbedding them in a permeable matrix such as a polymer, circumvents these issues, limiting obstruction to flow, stabilizing the cells, and preventing their release into the fluid phase. The ideal carrier material would be biocompatible, highly permeable, and mechanically and chemically stable. To date, several natural and synthetic polymers including polyacrylamide,[29] silica,[30] polyvinyl alcohol,[31] and more commonly alginate,[31-34] have been used to immobilize cells for metal adsorption applications in matrix-type capsules, or microparticles. With cells uniformly distributed throughout the material, these microparticles exhibit both the advantageous chemical characteristics of the biological material and the advantageous physical characteristics of the polymer. Polyethylene glycol diacrylate (PEGDA) is an attractive polymer matrix for cell immobilization as it is highly customizable, capable of being modified to display a range of physical and chemical characteristics, and is non-adsorptive, unlike other common polymers such as alginate and silica gel.[35-38] For biomining purposes, where the purity of the adsorbed metals is of paramount importance, it is crucial to minimize any non-specific adsorption by the carrier material. Finally, adsorbed REEs must be recovered through targeted desorption with an eluent such as citrate or EDTA. These eluents would degrade some polymer materials, such as alginate, which is ionically crosslinked with divalent metals, but PEGDA remains stable even after long exposure to these chemicals. With these considerations in mind, we have synthesized PEGDA microparticles impregnated with a high concentration of LBT-displayed *E. coli* cells to create an adaptable adsorbent suited for selective REE recovery in a continuous flow column.

## Methods

### *Bacterial strains and growth conditions*

The *E. coli* strain with an *lpp-ompA-dLBT* expression plasmid was grown in LB media containing 50 μg/ml ampicillin. Induction of LBT expression occurred at mid-exponential phase using 0.002% arabinose for 3 hr at 30°C. Park et al. (2016) and (2017) include a complete description of plasmid construction and LBT expression.[8, 9] Cells were harvested, washed once in 0.9% NaCl, and normalized by $OD_{600}$ in preparation for microparticle synthesis.

*Microparticle synthesis*

Three components are required for microparticle synthesis 1) polymer precursor: 1% (g/g) TPO-L photoiniator (2,4,6-Trimethylbenzoylphenyl phosphinic acid ethyl ester; Rahn AG) and 99% polyethylene glycol diacrylate (Mn 575; Sigma Aldrich); 2) cell suspension: ~$1x10^{11}$ cells/ml ($OD_{600}$ ~40) LBT-displayed *E. coli* in 10 mM MES pH 6; and 3) oil phase: 1% (g/g) Triton X-100 surfactant (Sigma Aldrich) and 99% 10cSt PDMS oil (polydimethylsiloxane; Clearco Products). 10 mM MES pH 6 was used as the cell suspension solution for all microparticle production batches except for one large batch, used to pack a 315 ml column, for which 0.9% NaCl was used. The polymer precursor and cell suspension were first mixed at a 1:3 ratio (25% PEGDA by volume) to produce the final aqueous phase. The oil phase and aqueous phases were then mixed to a ratio of ~7:1 (vol/vol) in 40 ml silanized borosilicate vials. The vials were vigorously shaken for ~15 s by hand to produce an emulsion and were immediately exposed to UV (4 $W/cm^2$ at 365 nm) for 120 s to polymerize the droplets comprised of PEGDA and LBT-displayed cells. The PDMS oil was removed from the polymerized microparticles by vacuum filtration through a 20 μm nylon mesh filter. The microparticles were rinsed ~10 times in 0.9% NaCl solution to remove any residual oil before being stored in 10 mM PIPES buffer pH 7 (or 0.9% NaCl for the 315 ml column batch) at ~4°C until use.

*Batch sorption experiments*

Microparticles were collected on a 20 μm nylon mesh filter and any residual liquid was removed. The microparticles were then distributed into 5 ml Eppendorf tubes at a controlled wetweight. To determine the dry weight, the particles were dried for >72 hours at ~65°C and re-weighed. For the batch adsorption capacity experiment, 4.5 ml of feedstock with varying Nd concentrations in 10 mM MES buffer pH 6 was added to 0.2 g (wet weight) of the microparticles. For the batch adsorption kinetics experiment, 5 ml of 500 μM Nd in 10 mM MES buffer pH 6 was added to 0.2 g (wet weight) of microparticles. The tubes were mixed in a rotator for the duration of the experiments (30 min for the adsorption capacity tests and 1-120 min for the adsorption kinetics tests). The Nd concentrations remaining in the solutions were tested colorimetrically with Arsenazo, and the amount of Nd adsorbed was calculated based on mass balance.

*Breakthrough columns*

Empty glass columns (Biorad) were packed with the cell/PEGDA microparticles. Column dimensions used were 15 x 0.5 cm, 20 x 0.5 cm, and 100 x 1 cm. The microparticle suspension was initially added gravimetrically, then packed down by adding slight pressure to the top of the column. Under pressure, the sorbent bed compressed and more microparticles were added. This procedure was repeated until the entire column volume was filled. The microparticle sorbent was conditioned with 10 mM MES buffer pH 6 at >5x the bed volume prior to REE adsorption. The REE feedstock was then pumped through the column at a measured rate of 1 ml/min unless otherwise specified. For most tests, the feedstock concentration was kept at 500 μM Nd in 10 mM MES buffer pH 6, though exceptions are described and discussed below. The effluent was collected in 1 ml aliquots during the adsorption step. Following adsorption, columns were desorbed with >1.5x fixed bed volume of 10 mM citrate, and again conditioned with 10 mM MES buffer pH 6 prior to reuse. The microparticles were removed from the columns that would no longer be used and dried down to assess dry adsorbent weight. REE concentrations of the samples were assessed by ICP-MS and/or colorimetrically with Arsenazo. Non-REE concentrations were measured by ICP-MS.

### *ICP-MS analysis*

Nd breakthrough column sample analyses were performed using a Thermo XSeriesII ICP-MS run in standard mode at UC Santa Cruz. The sample introduction system was an ESI PFA-ST nebulizer pumped at 120 μl/min. Selectivity column sample analyses were conducted at Idaho National Laboratory on an Agilent 7900 ICP-MS run in either hydrogen or helium gas modes.

## Results and Discussion

### *Microparticle synthesis and characterization*

To encapsulate a high density of LBT-displayed *E. coli* in PEGDA microparticles, we employed a bulk emulsion and polymerization technique. Microparticles were produced and tested over a range of cell densities and PEGDA concentrations in order to determine the optimal microparticle formulation. As expected, REE adsorption scaled in proportion to cell density between ~1.5x$10^{10}$ and ~9.6x$10^{10}$ cells/ml (Supplementary Figure 1a), suggesting that cell surface availability was not limited by increased cell density within the tested range. With a cell density above ~4.3x$10^{10}$ cells/ml, a higher PEGDA content (≥15 vol%) was required to maintain the physical integrity of the produced microparticles (data not shown). This increase in PEGDA content had a minimal negative effect on REE sorption (per unit wet weight) between 10 and 25 vol% (Supplementary Figure 1b). As such, all cell/PEGDA microparticles described in this work were formulated with ~10x$10^{10}$ cells/ml in 25 vol% PEGDA.

The microparticles were assessed in batch to determine their baseline REE adsorption behavior. Nd was used for these experiments given its abundance in many REE feedstocks and its high criticality. The calculated adsorption capacity was ~2.9 mg Nd/g dry particles. This capacity represents a significant decrease (~88.7%) from the LBT-displayed cells alone, which have an adsorption capacity of ~25.7 mg Nd/g dry cells.[9] This decrease is expected given that PEGDA, which is not adsorptive, contributes ~86.6% of the total dry weight of the microparticles as discussed above. The observed REE adsorption capacity is comparable to published values for some other adsorbents, which range from <1 to hundreds of mg/g.[7] The adsorption and desorption kinetics for free LBT-displayed cells were rapid, with equilibrium attained within 1 min (Figure 1); however, cell immobilization appears to slow the kinetics, with equilibrium attained at ~10 and ~5 min for adsorption and desorption, respectively (Figure 1). The slower sorption kinetics are unsurprising given that the feedstock must diffuse through the entire volume of the microparticles to reach all of the accessible cell surface functional groups. Although encapsulation does have a negative effect on adsorption capacity and kinetics compared to free-floating cells, the microparticles are a practical and scalable adsorbent while the cells alone are not.

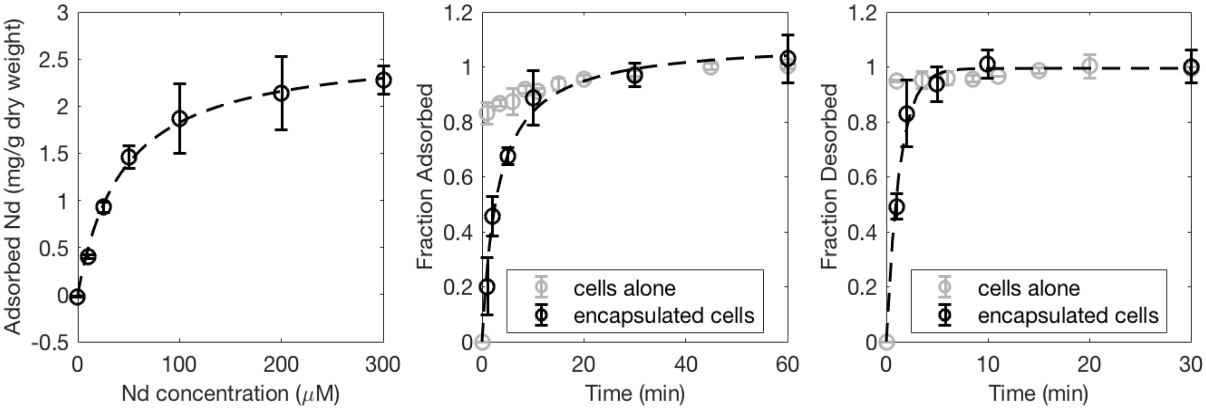

**Figure 1:** (a) Nd adsorption capacity, (b) Nd adsorption kinetics, and (c) Nd desorption kinetics of the microparticles (black symbols) and free-floating cells (grey symbols) in batch. The dotted line in the first plot is adsorption capacity fit with a Langmuir isotherm. The dotted lines in the second and third panels represent the fitted curves for second order adsorption and first order desorption behavior. The influent solution for adsorption was Nd in 10 mM MES buffer pH 6. 10 mM citrate was added for desorption.

*REE adsorption in a fixed-bed column*

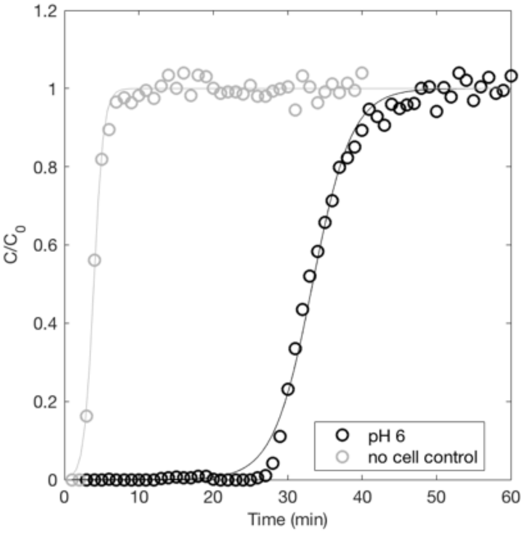

**Figure 2:** (a) Nd breakthough behavior from a 20 cm x 0.5 cm column packed with microparticles with or without the LBT-displayed cells at a flow rate of 1 ml/min. Influent composition was 500 µM Nd in 10 mM MES pH 6.

Breakthrough curves for fixed-bed columns packed with microparticles with or without cells were analyzed to assess any contribution of the PEGDA to REE recovery. In the column without cells, Nd breakthrough occurred almost immediately (after ~2 ml), and the delay is attributable to the passage of void volume rather than sorption (Figure 2). In the column with cells, on the other hand, Nd breakthrough occurred after ~28 ml, demonstrating a baseline Nd capacity of ~2.56 mg Nd/g dry sorbent (Figure 2). Breakthrough data were approximated with a Bohart-Adams model for visualization purposes. To establish the potential of these microparticles in a fixed bed REE extraction column, we conducted a series of column recovery experiments designed to assess the effects of influent flow rate, concentration, and pH.

REE extraction rates within a continuous flow column are determined by a combination of adsorption rate, diffusion rate within the particles, and influent flow rate. The ideal flow rate would enable rapid feedstock throughput without compromising extraction efficiency. Increasing flow rate above 1 ml/min caused increasingly early Nd breakthrough from the column (Figure 3a), likely due to Nd transport limitations within the microparticles. There was a small change observed in the calculated total adsorption capacity as flow rate increased from 0.5 to 1 ml/min, going from ~2.59 and ~2.50 mg Nd/g dry sorbent. As flow rate increased to 2 and then 5 ml/min,

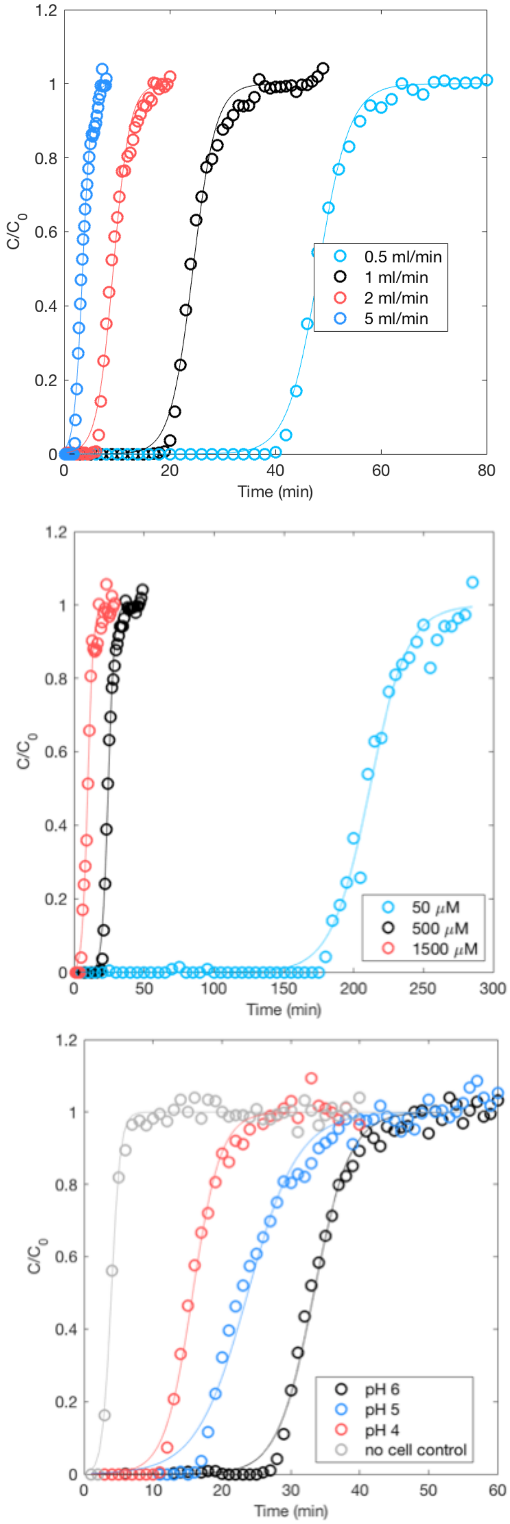

**Figure 3:** Breakthrough curves showing the effect of (a) flow rate, (b) initial influent concentration, and (c) influent pH on REE extraction. The column dimensions were 15 cm x 0.5 cm.

column capacity continued to decrease, to ~1.94 and ~1.83 mg Nd/g dry sorbent, respectively. Previous fixed-bed column studies have also observed a decrease in column adsorption capacity with increased flow rate.[29, 39] The equilibrium adsorption capacity of the sorbent should not change unless a physical or chemical process is affecting the available binding sites. In the case of flow rate, the most likely explanation is that increasing flow rates physically isolates a fraction of the binding sites from the feedstock, perhaps by causing bead deformation due to increased pressure in the column. In situations for which a high flow rate is required, the sorbent mass could be increased to account for the loss in adsorption capacity. These tested flow rates are rapid compared to other fixed-bed column studies for REE extraction,[29, 39] demonstrating that this system could more quickly process the desired feedstock volume, which is a significant advantage at an industrial scale. Based on these results, the remainder of the column experiments were conducted at a flow rate of 1 ml/min.

An ideal metal adsorption system would be capable of functioning across a wide range of influent concentrations to permit recovery from various feedstocks. We tested the effect of feedstock REE concentration on cell/PEGDA microparticle column performance at pH 6 and a flow rate of 1 ml/min. Observed REE adsorption capacity exhibited a small increase with increasing influent concentration, from ~2.29 to ~2.80 mg Nd/g dry sorbent at 50 and 1500 μM Nd in the influent. The breakthrough points were roughly proportional to feedstock concentration, occurring at ~5 ml, ~19 ml, and ~185 ml for the influents with 1500 μM, 500 μM, and 50 μM Nd, respectively (Figure 3b). Based on this data, the scalability of this column system in terms of influent concentration can be assessed. The maximum practical REE concentration can be estimated by calculating the total molar adsorption capacity, at the given column conditions, and dividing that capacity by the minimum volume that could be passed through the column, which is approximately the column pore volume (~76% of total column volume). Other variables, such as pH, must be accounted for when designing a system for a specific influent; however, at this influent composition, the maximum concentration is estimated to be ~21 mM Nd. Once the concentration goes above that threshold, there will be insufficient fluid volume to distribute the REEs across all of the available cell surface sites, and the extraction process would require further steps. In cases where waste volume is not a limiting factor, the influent may be diluted to a usable concentration. Because the LBT-displayed cells have a high selectivity for REEs compared to most non-REE metals, these microparticles in a continuous flow column system are particularly well suited to low-grade REE feedstocks such as geothermal fluids. Large volumes of these feedstocks could be passed through relatively low volume fixed bed columns to purify and dramatically concentrate the REEs.

Many aqueous REE feedstocks, from the leachates of solid materials like E-waste and coal byproducts to REE-bearing geothermal fluids, have a low pH. It is therefore crucial that a

REE adsorbent be able to function at low pH conditions. REE extraction by cell/PEGDA microparticles packed in 20 cm x 0.5 cm continuous flow columns was tested at an influent pH of 4, 5, and 6 (Figure 3c). Influent composition was 500 uM Nd in 10 mM HomoPIPES (pH 4 or 5) or MES buffer (pH 6). Optimal recovery performance was observed at pH 6, and the breakthrough point came progressively earlier with decreasing pH, from ~28 ml at pH 6 to ~17 ml at pH 5 and ~12 ml at pH 4 (Figure 3c). The total adsorption capacity was also strongly correlated with pH, decreasing from ~2.56 to ~1.79 to ~1.13 mg Nd/g dry sorbent, for pH 6, 5, and 4, respectively. This decrease in recovery from pH 6 to 4 represents an ~56% loss in column capacity, comparable to the observed decrease in REE adsorption with free-floating LBT-displayed cells (~57%).[8] The microparticle columns do remain functional REE adsorbents down to pH 4, albeit with significant loss in performance. This loss may, however, be accounted for by increasing the column size for low pH influents, permitting this recovery technique to be used with a variety of feedstocks without the need for pH adjustment.

### *Column Reusability*

A green mining adsorption system becomes increasingly practical and economically feasible if it is capable of being reused multiple times without a major loss in performance. To assess cell/PEGDA microparticle reusability, a single column was tested over 9 adsorption/desorption cycles. Each cycle, adsorption from an influent with 500 μM Nd in 10 mM MES buffer pH 6 was measured. Desorption was achieved by passing 10 mM citrate (pH ~6) through the column after adsorption (Figure 4a). 10 mM MES buffer pH 6 was passed through the column following desorption to remove any residual citrate in preparation for the next adsorption phase. A small, gradual decrease in adsorption capacity (totaling ~18%) was observed over the course of the nine cycles (Figure 4a), corresponding with progressively earlier Nd breakthrough (Figure 4b). We attribute this performance loss to the citrate desorption process, likely due to minor, gradual degradation of the cell surfaces over prolonged exposure periods. These data show that the cell/PEGDA adsorbent columns exhibit excellent reusability over >9 adsorption/desorption cycles.

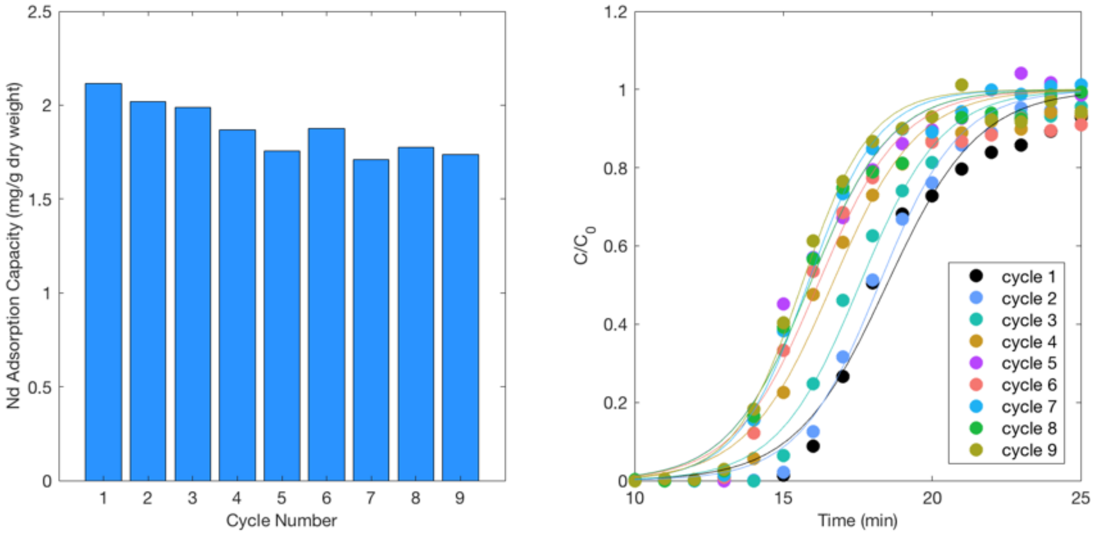

**Figure 4:** (a) Nd adsorption capacity and (b) Nd breakthrough behavior of the microparticles in a fixed-bed column after 1 to 9 adsorption/desorption cycles. The feedstock solution was 500 µM Nd in 10 mM MES buffer pH 6 for each test. ~35 ml 10 mM citrate was used for desorption, and then the column was washed with >100 ml 10 mM MES buffer pH 6 prior to the next adsorption cycle. The column dimensions were 15 cm x 0.5 cm and flow rate was 1 ml/min.

### *Selective REE Recovery*

A continuous flow column that is capable of achieving a degree of separation between the individual REEs would be advantageous because it would allow the user to have some control over the final product composition, rather than just generating a total REE mixture. The LBT-displayed *E. coli* cells have previously been shown to exhibit some selectivity between different REEs,[9] and a sufficiently large column may be able to exploit this selectivity for REE separation. A 100 x 1 cm column was packed with the microparticles to test REE selectivity with a synthetic multi-REE influent. The feedstock contained equal concentrations (500 µM) of Y and all of the lanthanides except Pm in 10 mM MES buffer pH 6. The sorbent generally exhibited a preference for the heavy REEs over the light REEs, with a particular affinity for Sm, Eu, Yb, and Lu (Figure 5). Light REEs that were initially adsorbed onto the column prior to reaching adsorption capacity were ultimately desorbed and replaced by the heavy REEs as evidenced by the spike in La and Ce concentration in the effluent, reaching concentrations above that of the initial feedstock, as heavy REE adsorption increased (Figure 5a). This observed selectivity for heavy REEs would permit us to achieve a degree of the separation between the REEs in a breakthrough column and may be further exploited with a chromatography column system design to separate individual REEs or REE pairs.

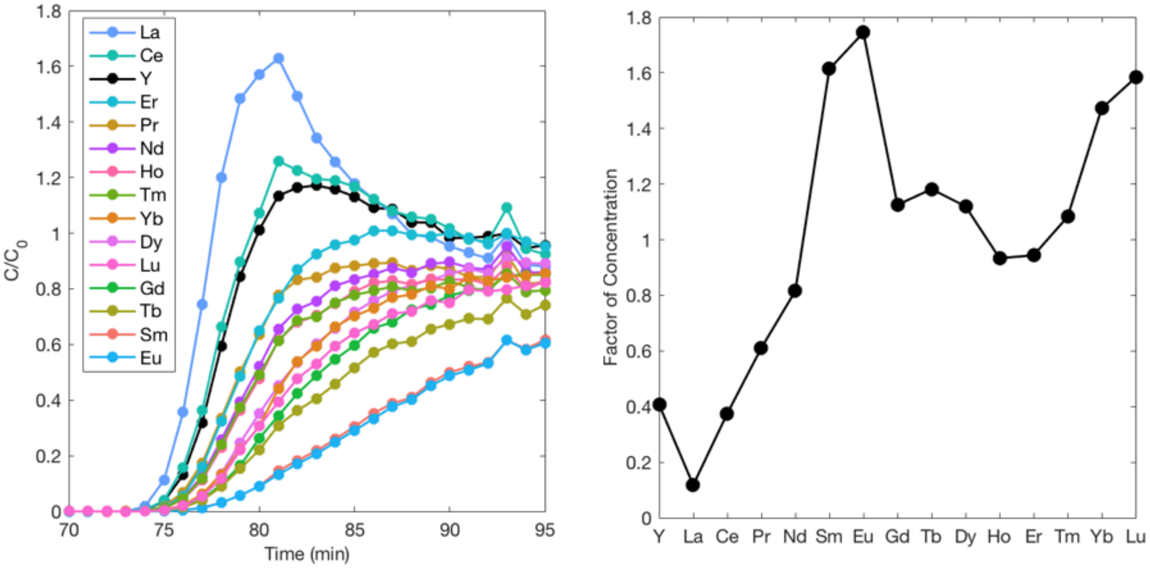

**Figure 5:** (a) Breakthrough curves for all REEs (except Pm and Sc) from a 100 cm x 1 cm fixed bed column. (b) Factor of concentration for each REE. The initial feedstock had approx. equal concentrations of all REEs in a 10 mM MES buffer pH 6 solution matrix. The flow rate through the column was 1 ml/min.

### *Implications for REE extraction*

The LBT-displayed cells, and a number of other REE adsorbents, have shown great promise in terms of their REE adsorption capacity and selectivity; however, many of these adsorbents have not yet been incorporated into a practical, industrial-scale REE recovery technology. The requirements for an industrial-scale REE adsorbent go beyond simply its adsorptive characteristics. In addition to having adequate REE adsorption capacity and kinetics, the sorbent must be reusable, stable in the presence of harsh REE feedstocks and eluents, capable of being applied in continuous flow systems, and easily and sustainably produced. Based on these criteria, the cell/PEGDA microparticles are suited for REE extraction processes beyond the bench scale, unlike many REE sorbents, including LBT-displayed cells alone.

Immobilizing LBT-displayed cells in PEGDA microparticles creates a REE adsorbent that has the advantageous adsorptive characteristics of the cell surfaces and the advantageous physical characteristics of the polymer. While the microparticles do have a lower adsorption capacity than the cells, immobilization has successfully enabled the cells to be used in continuous flow column extraction systems. The microparticles are also highly stable, capable of being recycled and reused through many adsorption/desorption cycles. Furthermore, the microparticles are relatively simple to synthesize in large quantities, allowing the technology to be scaled to the requirements of the specific application. This microparticle synthesis method could be easily scaled to rapidly produce large volumes of sorbent for industrial-scale REE recovery operations, for example, by incorporating an in-line emulsifier and UV source to continuously mix and polymerize the microparticles. The microparticles are an effective, green REE adsorbent that is readily scalable, broadly reusable, and can be applied in continuous flow systems.

## Acknowledgements

We would like to thank Kevin Paulsen for his assistance silanizing the borosilicate vials. AB acknowledges funding from the Livermore Graduate Scholar Program from Lawrence Livermore National Laboratory. This work was performed under the auspices of the U.S. Department of Energy by Lawrence Livermore National Laboratory under Contract DEAC52-07NA27344 (LLNL-TH-763869).

**Supporting Information.** Figure S1, Tb adsorption capacity as a function of cell density and PEGDA content for the cell/PEGDA microparticles; Figure S2, Comparison of Nd breakthrough data for a single column based on colorimetric assays (Arsenazo) and ICP-MS analyses**.**

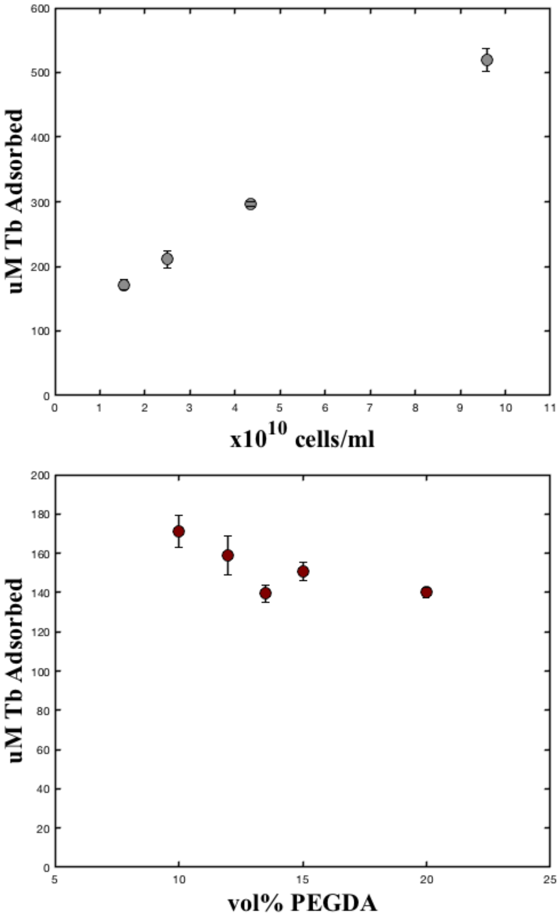

**Figure S1:** (a) µM Tb adsorbed as a function of cell density in the cell/PEGDA microparticles. PEGDA was set at 10 vol% for all microparticles, except for the highest tested point (~10x10$^{10}$ cells/ml) for which 15 vol% PEGDA was required to maintain particle integrity. (b) µM Tb adsorbed as a function of PEGDA fraction (vol%) in the cell/PEGDA microparticles. Cell density was set at ~1.5x10$^{10}$ cells/ml. In all sorption assays, 0.5 g of microparticles was exposed to 4 ml of 300 µM Tb in 10 mM MES buffer pH 6 in a 5 ml Eppendorf tube for ~30 minutes, except for the highest cell density (~10x10$^{10}$ cells/ml), which required 600 µM Tb due to its high adsorption capacity. Error bars represent the SD of the assays in triplicate.

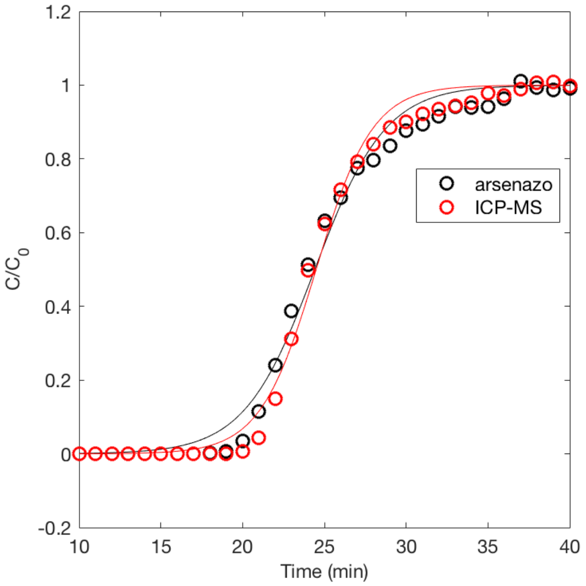

**Figure S2:** Comparison of a breakthrough curve with Nd concentrations measured colorimetrically with Arsenazo (black line and symbols) and with an ICP-MS (red line and symbols).

## References

1. DOE, Critical Materials Strategy. In 2011.

2. Zhou, B. Li, Z.;Chen, C., Global potential of rare earth resources and rare earth demand from clean technologies. *Minerals* **2017,** *7*, 1-14.

3. Wood, S. A., Behavior of rare earth elements in geothermal systems: A new exploration/exploitation tool? In DOE, Ed. Geothermal Reservoir Technology Research: 2001.

4. Taggart, R. K.; Hower, J. C.; Dwyer, G. S.; Hsu-Kim, H., Trends in the Rare Earth Element Content of U.S.-Based Coal Combustion Fly Ashes. *Environ Sci Technol* **2016,** *50*, (11), 5919-5926.

5. Qi, H.; Hu, R.; Zhang, Q., REE Geochemistry of the Cretaceous lignite from Wulantuga Germanium Deposit, Inner Mongolia, Northeastern China. *International Journal of Coal Geology* **2007,** *71*, (2), 329-344.

6. Lixandru, A.; Venkatesan, P.; Jönsson, C.; Poenaru, I.; Hall, B.; Yang, Y.; Walton, A.; Güth, K.; Gauß, R.; Gutfleisch, O., Identification and recovery of rare-earth permanent magnets from waste electrical and electronic equipment. *Waste Management* **2017,** *68*, 482-489.

7. Anastopoulos, I.; Bhatnagar, A.; Lima, E. C., Adsorption of rare earth metals: A review of recent literature. *Journal of Molecular Liquids* **2016,** *221*, 954-962.

8. Park, D. M.; Reed, D. W.; Yung, M. C.; Eslamimanesh, A.; Lencka, M. M.; Anderko, A.; Fujita, Y.; Riman, R. E.; Navrotsky, A.; Jiao, Y. Q., Bioadsorption of Rare Earth Elements through Cell Surface Display of Lanthanide Binding Tags. *Environ Sci Technol* **2016,** *50*, (5), 2735-2742.

9. Park, D. M.; Brewer, A.; Reed, D. W.; Lammers, L. N.; Jiao, Y., Recovery of Rare Earth Elements from Low-Grade Feedstock Leachates Using Engineered Bacteria. *Environ Sci Technol* **2017,** *51*, (22), 13471-13480.

10. Jin, H. Y.; Park, D. M.; Gupta, M.; Brewer, A. W.; Ho, L.; Singer, S. L.; Bourcier, W. L.; Woods, S.; Reed, D. W.; Lammers, L. N.; Sutherland, J. W.; Jiao, Y. Q., Techno-economic Assessment for Integrating Biosorption into Rare Earth Recovery Process. *Acs Sustain Chem Eng* **2017,** *5*, (11), 10148-10155.

11. Takahashi, Y.; Kondo, K.; Miyaji, A.; Watanabe, Y.; Fan, Q.; Honma, T.; Tanaka, K., Recovery and Separation of Rare Earth Elements Using Salmon Milt. *PLOS ONE* **2014,** *9*, (12), e114858.

12. Varshini, J. S. C., Nilanjana, D., Screening of biowaste materials for the sorption of cerium (III) from aqueous environment. *Research Journal of Pharmaceutical, Biological and Chemical Sciences* **2014,** *5*, 402-408.

13. Bertagnolli, C.; Grishin, A.; Vincent, T.; Guibal, E., Recovering Heavy Metal Ions from Complex Solutions Using Polyethylenimine Derivatives Encapsulated in Alginate Matrix. *Industrial & Engineering Chemistry Research* **2016,** *55*, (8), 2461-2470.

14. Crane, R. A.; Sapsford, D. J., Sorption and fractionation of rare earth element ions onto nanoscale zerovalent iron particles. *Chem Eng J* **2018,** *345*, 126-137.

15. Gok, C., Neodymium and samarium recovery by magnetic nano-hydroxyapatite. *Journal of Radioanalytical and Nuclear Chemistry* **2014,** *301*, (3), 641-651.

16. Dodson, J. R.; Parker, H. L.; Garcia, A. M.; Hicken, A.; Asemave, K.; Farmer, T. J.; He, H.; Clark, J. H.; Hunt, A. J., Bio-derived materials as a green route for precious & critical metal recovery and re-use. *Green Chem* **2015,** *17*, (4), 1951-1965.

17. Jacinto, J.; Henriques, B.; Duarte, A. C.; Vale, C.; Pereira, E., Removal and recovery of Critical Rare Elements from contaminated waters by living Gracilaria gracilis. *J Hazard Mater* **2018,** *344*, 531-538.

18. Lo, Y. C.; Cheng, C. L.; Han, Y. L.; Chen, B. Y.; Chang, J. S., Recovery of high-value metals from geothermal sites by biosorption and bioaccumulation. *Bioresource Technol* **2014,** *160*, 182-190.

19. Kucuker, M. A.; Wieczorek, N.; Kuchta, K.; Copty, N. K., Biosorption of neodymium on Chlorella vulgaris in aqueous solution obtained from hard disk drive magnets. *PLoS One* **2017,** *12*, (4), e0175255.

20. Jiang, M. Y.; Ohnuki, T.; Tanaka, K.; Kozai, N.; Kamiishi, E.; Utsunomiya, S., Post-adsorption process of Yb phosphate nano-particle formation by Saccharomyces cerevisiae. *Geochim Cosmochim Ac* **2012,** *93*, 30-46.

21. Moriwaki, H.; Yamamoto, H., Interactions of microorganisms with rare earth ions and their utilization for separation and environmental technology. *Appl Microbiol Biot* **2013,** *97*, (1), 1-8.

22. Ozaki, T.; Gillow, J. B.; Kimura, T.; Ohnuki, T.; Yoshida, Z.; Francis, A. J., Sorption behavior of europium(III) and curium(III) on the cell surfaces of microorganisms. *Radiochim Acta* **2004,** *92*, (9-11), 741-748.

23. Texier, A. C.; Andres, Y.; Le Cloirec, P., Selective biosorption of lanthanide (La, Eu, Yb) ions by Pseudomonas aeruginosa. *Environ Sci Technol* **1999,** *33*, (3), 489-495.

24. Tsuruta, T., Accumulation of rare earth elements in various microorganisms. *J Rare Earth* **2007,** *25*, (5), 526-532.

25. Nash, K. L.; Jensen, M. P., Analytical-scale separations of the lanthanides: A review of techniques and fundamentals. *Sep Sci Technol* **2001,** *36*, (5-6), 1257-1282.

26. Xie, F.; Zhang, T. A.; Dreisinger, D.; Doyle, F., A critical review on solvent extraction of rare earths from aqueous solutions. *Miner Eng* **2014,** *56*, 10-28.

27. Moriwaki, H.; Koide, R.; Yoshikawa, R.; Warabino, Y.; Yamamoto, H., Adsorption of rare earth ions onto the cell walls of wild-type and lipoteichoic acid-defective strains of Bacillus subtilis. *Appl Microbiol Biot* **2013,** *97*, (8), 3721-3728.

28. Zhu, Y., Chapter 14 - Immobilized Cell Fermentation for Production of Chemicals and Fuels. In *Bioprocessing for Value-Added Products from Renewable Resources*, Yang, S.-T., Ed. Elsevier: Amsterdam, 2007; pp 373-396.

29. Texier, A. C.; Andres, Y.; Faur-Brasquet, C.; Le Cloirec, P., Fixed-bed study for lanthanide (La, Eu, Yb) ions removal from aqueous solutions by immobilized Pseudomonas aeruginosa: experimental data and modelization. *Chemosphere* **2002,** *47*, (3), 333-42.

30. Cabuk, A.; Akar, T.; Tunali, S.; Tabak, O., Biosorption characteristics of Bacillus sp. ATS-2 immobilized in silica gel for removal of Pb(II). *J Hazard Mater* **2006,** *136*, (2), 317-23.

31. Tsekova, K. T., D.; Ganeva, S., Removal of heavy metals from industrial wastewater by free and immobilized cells of Aspergillus niger. *International Biodeterioration & Biodegradation* **2010,** *64*, 447-451.

32. Xu, J.; Song, X. C.; Zhang, Q.; Pan, H.; Liang, Y.; Fan, X. W.; Li, Y. Z., Characterization of metal removal of immobilized Bacillus strain CR-7 biomass from aqueous solutions. *J Hazard Mater* **2011,** *187*, (1-3), 450-8.

33. Preetha, B. V., T., Batch and continuous biosorption of chromium(VI) by Rhizopus arrhizus. *Separation and Purification Technology* **2007,** *57*, 126-133.

34. Kuhn, S. P. P., R.M., Adsorption of mixed metals and cadmium by calcium-alginate immobilized Zoogloea ramigera. *Appl Microbiol Biot* **1989,** *31*, (5-6), 613-618.

35. Michelini, E.; Roda, A., Staying alive: new perspectives on cell immobilization for biosensing purposes. *Analytical and Bioanalytical Chemistry* **2012,** *402*, (5), 1785-1797.

36. Lee, K. G.; Park, T. J.; Soo, S. Y.; Wang, K. W.; Kim, B. I. I.; Park, J. H.; Lee, C.-S.; Kim, D. H.; Lee, S. J., Synthesis and utilization of E. coli-encapsulated PEG-based

microdroplet using a microfluidic chip for biological application. *Biotechnology and Bioengineering* **2010,** *107*, (4), 747-751.

37. Son, H. A.; Choi, S. K.; Jeong, E. S.; Kim, B.; Kim, H. T.; Sung, W. M.; Kim, J. W., Microbial Activation of Bacillus subtilis-Immobilized Microgel Particles for Enhanced Oil Recovery. *Langmuir* **2016,** *32*, (35), 8909-8915.

38. Akselrod, G. M.; Timp, W.; Mirsaidov, U.; Zhao, Q.; Li, C.; Timp, R.; Timp, K.; Matsudaira, P.; Timp, G., Laser-Guided Assembly of Heterotypic Three-Dimensional Living Cell Microarrays. *Biophysical Journal* **2006,** *91*, (9), 3465-3473.

39. Chu, K. H.; Hashim, M. A., Copper biosorption on immobilized seaweed biomass: Column breakthrough characteristics. *Journal of Environmental Sciences* **2007,** *19*, (8), 928-932.

# CHAPTER 7: Summary and Future Work

The first portion of this dissertation investigates Mg isotope fractionation associated with biological and chemical weathering and weathered materials. I first discuss a laboratory study of the effects of cell surface reactivity on Mg isotopes in a forsterite weathering system. Next, I characterize the Mg isotope fractionation associated granite and granodiorite weathering in natural environments. Finally, I conclude with the use of Mg isotopes to trace the fate of upper crustal materials in volcanic arc magmas. The described results further our understanding of Mg isotope behavior during biological and chemical weathering and the effects of upper crustal material on the Mg isotope composition of volcanic arc rocks. The main conclusions from these chapters are discussed below:

1. Chapter 2 discusses Mg isotope fractionation during forsterite dissolution in the presence of *Bacillus subtilis* endospores. Because the endospores do not have an active metabolism or release significant organic acids, their surface reactivity is the only way that they affect the weathering system. The endospores therefore are ideal for demonstrating the isolated effects of cell surface reactivity on Mg isotopes during weathering. As the forsterite dissolves, $^{24}$Mg is preferentially leached from the mineral into the aqueous phase, and the presence of endospores has little impact on this process despite increasing initial dissolution rate. However, the endospore surfaces preferentially adsorb $^{24}$Mg from the aqueous phase, causing the Mg isotope composition of the liquid phase to increase in proportion to the fraction of aqueous Mg adsorbed. With further study of the other ways in which microbes can fractionate Mg isotopes, this geochemical tracer may function as a biosignature in weathered rock.

2. Chapter 3 describes the Mg isotope composition of four granite and granodiorite weathering profiles from Boulder Creek, Colorado, USA. As weathering progresses, the primary biotite is lost, but most Mg is retained in the solid phase as secondary illite. A small increase in Mg isotope composition is observed at >2 m depth during this process as some $^{24}$Mg is preferentially lost to the hydrosphere. However, as weathering continues, the secondary illite is lost, with Mg retained in the profile adsorbed onto other clay minerals like kaolinite. Exchangeable Mg is typically isotopically light, which is reflected in a decrease in Mg isotope composition in this upper portion of the weathering profiles. These results demonstrate the effects of chemical weathering on the Mg isotope composition of felsic lithologies, which informs Mg cycling in many continental surface environments.
3. Chapter 4 presents Mg isotope data for a suite of well-characterized samples from the North Cascade Volcanic Arc that are known to exhibit variable input from upper crustal materials (Mullen and Weis, 2013, 2015; Mullen and McCallum, 2014; Mullen et al., 2017). The Mg isotope results, in conjunction with trace element data, demonstrate that the addition of isotopically heavy upper crustal material to upwelling magmas during assimilation and fractional crystallization caused a small, but measurable, increase in Mg isotope composition in some locations. A small contribution to Mg isotope composition due to bulk mixing of subducted materials cannot be ruled out. With further study, Mg isotope systematics may supplement traditional geochemical tracers to monitor the addition of crustal materials to primitive magmas in a variety of geological settings.

Magnesium isotope behavior has become increasingly well characterized for a wide range of geological processes, but many avenues remain for further investigation. In the context of weathering specifically, I believe that important advances could be made in our mechanistic understanding of specific weathering processes. Natural weathering systems are typically the result of a combination of several distinct processes that can be difficult to differentiate or quantify. Primary mineral dissolution, secondary mineral formation, surface adsorption, and uptake into plants, for example, could all play a role in determining the ultimate composition of a weathered rock. Laboratory studies at controlled conditions can isolate the Mg isotope fractionation associated with a single process in isolation. Armed with the results of a more comprehensive series of these laboratory studies, a researcher could interpret Mg isotope data from natural weathering environments much more rigorously than is currently possible.

*Part 2*

The second portion of this dissertation describes the application of engineered *E. coli* for the selective extraction of rare earth elements (REEs) from non-traditional feedstocks. First, I investigate the possibility of using these microbes to recover REEs specifically from natural geofluids. The work assesses the chemical characteristics of these feedstocks, such as pH and temperature, in terms of their effect on REE biosorption. Next, I encapsulate the engineered microbes in polymer microcapsules to create a scalable hybrid adsorbent that may be practical and economically-feasible for industrial REE extraction and purification operations.

1. Natural geofluids have several characteristics that present obstacles for REE extraction, including low REE contents, high total dissolved solids (TDS), high concentrations of competitive metals, low pH, and high temperatures. Chapter 5 discusses the effects of these variables on REE adsorption by engineered *E. coli*. The beneficial adsorptive characteristics of the cells (high capacity and high selectivity) are retained at a wide range of chemical conditions relevant to geofluids. The results obtained during this study will inform the use of biosorption for practical REE recovery from geothermal fluids.

2. Chapter 6 discusses the encapsulation of engineered *E. coli* in polyethylene glycol diacrylate (PEGDA) microparticles for use in continuous flow REE extraction systems. The synthesis procedure is described along with the fundamental physical and chemical characteristics of the microparticles. When packed in a fixed bed column, the hybrid adsorbent is an effective REE extractant at a variety of feedstock concentrations and pH conditions and with several influent flow rates. The optimal conditions for REE recovery are assessed, as is the possibility of the separation of individual REEs in a column extraction system using this adsorbent. The work described in this chapter represents a significant step towards industrial scale application of biosorption for REE extraction and purification.

The importance of REEs to the modern economy, in combination with their potential supply vulnerability, makes the design of novel REE extraction technologies from novel feedstocks a matter of immediate practical concern. Ample progress has been made in the initial development and characterization of many promising REE-specific adsorbents for solid phase extraction systems. However, these materials have generally not progressed to a technology readiness level that approaches industrial scale application. I believe that advancements in polymer encapsulation, particularly in the area of microfluidics, may permit a variety of adsorbents to make the jump from proof of concept to actual application. Once these technologies have been adequately developed, a wide range of applications become possible, from remediation to green mining to analytical chromatography, just to name a few.

## References

Mullen EK, McCallum IS (2014). Origin of Basalts in a Hot Subduction Setting: Petrological and Geochemical Insights from Mt. Baker, Northern Cascade Arc. J Petrol 55(2):241-281.

Mullen EK, Weis D (2013). Sr-Nd-Nf-Pb isotope and trace element evidence for the origin of alkali basalts in the Garabaldi Belt, northern Cascade arc. Geochem Geophy Geosy 14:3126-3155.

Mullen EK, Weis D (2015). Evidence for trench-parallel mantle flow in the northern Cascade Arc from basalt geochemistry. Earth Planet Sc Lett 414:100-107.

Mullen EK, Weis D, Marsh NB, Martindale M (2017). Primitive arc magma diversity: New geochemical insights in the Cascade Arc. Chem Geol 448:43-70.